Grid-Based Split Operator-Quantum Fourier Transform Algorithms for Time-Dependent Quantum Simulation

Xiaoning Feng

Brasenose College

University of Oxford

A thesis submitted for the degree of

Doctor of Philosophy

October 2025

Acknowledgements

I would first like to express my sincere gratitude to my supervisor, Professor David Tew, for welcoming me into his research group and for the unwavering support he has provided throughout my doctoral studies. His expertise, patience, and insightful guidance have shaped the way I think about science, and I have always appreciated the trust he placed in my abilities and the encouragement he gave me to explore ideas freely.

I am also grateful to Hans Hon Sang Chan, who has been both a colleague and a friend throughout these years. I have greatly benefited from our stimulating discussions, and his thoughtful advice has supported me through many challenges. In addition, I would like to thank Arman Nejad for providing helpful suggestions and time-independent reference data on water's fundamental bands. I am also thankful to all members of the Tew Group for creating such a friendly and collaborative research environment.

My deepest and most heartfelt gratitude goes to my mom, Fengren Ma, and my dad, Yabin Feng. Their unconditional love and constant encouragement have carried me further than I ever imagined possible. I am the person I am today because of their endless support, and every success I have had belongs as much to them as it does to me.

Before I realised how far I had come, my little boat had already sailed beyond a thousand mountains. To all who made this journey possible: thank you, from the bottom of my heart.

Abstract

This thesis investigates the grid-based Split Operator–Quantum Fourier Transform (SO-QFT) scheme as a general-purpose backbone for time-dependent quantum simulation. We develop an end-to-end algorithmic framework that unifies state preparation on discretised grids, SO-QFT time propagation, and the extraction of observables via autocorrelation functions, with a focus on efficient quantum circuit construction. Classical emulation is used to evaluate the performance and resource demands of this framework across diverse chemical contexts. For vibronic dynamics arising from conical intersections, we assemble a complete workflow that reproduces absorption spectra and population transfer for a well-characterised prototypical polyatomic system. On this basis, we estimate the required quantum resources by mapping grid size, time resolution and spectral precision to qubit budgets, circuit depths and measurement counts. The framework is further tailored to infrared spectroscopy through probabilistic encoding of non-unitary dipole operators and explicit treatment of higher-order Hamiltonian terms via multi-controlled operations. To minimise gate depth, we optimise time discretisation and employ approximation strategies for initial states and dipole truncations, while preserving the fidelity of computed spectra. Importantly, the resource scaling relations derived from the vibronic and infrared simulations generalise to comparable molecular systems, providing a transferable template for predicting resource estimates beyond the specific benchmark studied. Finally, the methodology is extended to Coulombic systems, whose singular potentials challenge grid-based representations. We improve the simulation fidelity by proposing two correction schemes: a Hamiltonian correction that accounts for grid-basis structure, and a modification of the initial wavefunction to better match the discretised Hamiltonian. Both corrections are compatible with compact quantum encodings, and their representation in truncated Fourier or Walsh series offers an additional reduction in circuit depth. Collectively, these studies advance the grid-based SO-QFT scheme from a promising construct to a systematically assessed framework, establishing methodological guidance, algorithmic variants and quantitative resource benchmarks for future fault-tolerant quantum applications.

Contents

List of Figures

List of Tables

List of Abbreviations

CI . . . . . Confidence Interval

DM . . . . . Dipole Moment

DMS . . . . . Dipole Moment Surface

FFT . . . . . Fast Fourier Transform

IR . . . . . Infrared

ITE . . . . . Imaginary Time Evolution

PES . . . . . Potential Energy Surface

QFT . . . . . Quantum Fourier Transform

QPE . . . . . Quantum Phase Estimation

SO-FT . . . . . Split Operator-Fourier Transform

SO-QFT . . . Split Operator-Quantum Fourier Transform

TVD . . . . . Total Variation Distance

ZPE . . . . . Zero Point Energy

1 Introduction

Contents

1.1 Background

1.1.1 Foundations of Time-Dependent Quantum Simulation

Understanding real-time evolution of quantum systems remains one of the central challenges in theoretical chemistry and chemical physics. Theoretical studies aim to capture such quantum dynamics with high fidelity, which requires faithfully solving the time-dependent Schrödinger equation. Given an initial state of a chemical system, one can compute and reveal dynamical properties of interest by propagating the system with the corresponding Hamiltonian. Various numerical schemes have been developed to achieve this time evolution. These include direct numerical integrators [1], finite-difference integrators [2–5], Chebyshev and Lanczos polynomial expansions [6, 7], and matrix diagonalization approaches [8–10]. While each of these

approaches has its advantages, they often involve either heavy linear-algebra routines, limited scalability, or difficulties in preserving unitarity over long propagation times.

Among various numerical methods, the Split Operator-Fourier Transform (SO-FT) method [11–14], originated from Trotter-Suzuki decomposition [15–17], stands out by combining exact unitarity with remarkable computational efficiency and simplicity of implementation. It exploits the fact that the kinetic and potential operators are diagonal in the momentum and real space representations, respectively, thereby avoiding the numerical difficulties associated with the non-local kinetic operator in real space. Conversions between complementary spaces are performed using Fourier Transform. By decomposing the time evolution into alternating kinetic and potential updates, SO-FT achieves impressive performance across many scenarios [18–22].

However, these existing classical algorithms, although powerful, inevitably encounter exponential growth of Hilbert space with system size. This poses an expensive demand for computational resources, restricting their practical use to systems of modest dimensionality. Despite that ingenious approximations have been developed, from multi-configurational wavefunction methods [23–26] to tensor network approaches [27–31], the exponential scaling barrier persists, rendering many realistic systems beyond reach.

Quantum computing provides a fundamentally different paradigm for simulating large and complex chemical systems. While simulations on classical hardware can rapidly exceeds the tractable limits of classical computation as the number of vibrational or electronic degrees of freedom increases, quantum computing algorithms promise significant resource advantage and runtime reduction over their classical counterparts [32–35]. The unique properties of qubits, such as superposition, entanglement, and interference, offer the potential to overcome inherent limitations of classical techniques [36–39], especially the prohibitive scaling of required computational resources in many-body quantum simulations. Researchers seek greater clarity on exactly which practical algorithms can be ported to quantum computers to deliver a compelling advantage, and hence substantial progress has

been made in the design of quantum algorithms that simulates interacting particles at the quantum gate or circuit level [40–51].

Against this backdrop, the trotterized SO-QFT method represents a natural evolution of SO-FT towards quantum platforms, by replacing the classical Fourier transform component by the transformative Quantum Fourier Transform (QFT) [52–54]. QFT was first implemented in Shor's Algorithm [55], and nowadays forms the basis of many quantum simulation algorithms due to its exponential speed-up over the discrete Fourier Transform [56–60]. At its core, the SO-QFT technique retains the operator splitting procedure to separately treat kinetic and potential contributions, allowing for sequential unitary application in their respective spaces.

Competing alternatives such as linear combination of unitaries (LCU) techniques [61–64] and qubitization [65–68], achieve theoretically optimal error scaling, but are often associated with non-trivial block encodings and quantum signal processing sequences. These translate into intricate circuit constructions with substantial ancilla overhead. In this regard, SO-QFT offers a more straightforward framework for practical contexts where intuitive and accessible circuit design and moderate resource demands are of primary importance: its circuit depth is typically shallower with minimal overhead, its reliance on QFT ensures efficient basis changes, and its structure preserves a direct connection to well-established classical SO-FT algorithms.

On the other hand, the grid-based representation becomes particularly appealing within the quantum computing field, as the discretisation of continuous coordinates maps naturally onto qubit states. Several recent studies have demonstrated the synergies of integrating grid-based representations with quantum computing [69–71]. In stark contrast to the exponential growth in complexity exhibited from classical computers, quantum computer's ability to scale the qubit count polynomially with system size [72] positions the grid-based representation as a very compatible choice in the quantum domain.

While propagation via SO-QFT leverages primitives readily implemented on quantum hardware, e.g., timestep-wise unitary operations and the use of QFT,

its combination with grid-based representation opens new possibility for tracking classically inaccessible problems. This approach has been investigated in many previous works [69, 70, 73–76]. With its favourable scaling with respect to quantum resources, the grid-based SO-QFT method has been regarded as a potential avenue for exploring quantum advantage in chemically relevant simulations. Establishing scalable frameworks, resource estimates, and accuracy benchmarks in this setting is therefore not only of methodological interest but also of strategic importance for the broader field of quantum simulation.

1.1.2 Physical Context of the Target Problems

The molecular phenomena addressed in Chapters 3 and 4 are initiated by light absorption and characterised by the subsequent redistribution of energy between electronic and nuclear motion. Within the Born–Oppenheimer approximation, photoexcitation is described as a vertical transition between electronic states at fixed nuclear geometry, typically occurring on a femtosecond timescale [77, 78]. The nuclear wavefunction, initially prepared in the vibrational ground state of the electronic ground surface, is thereby projected onto an excited-state surface and evolves under coupled electronic–nuclear dynamics [79, 80].

A key feature of excited-state dynamics is the presence of nonradiative decay pathways. In particular, relaxation can proceed through conical intersections, where two adiabatic potential energy surfaces become degenerate [81, 82]. Faithful descriptions of such processes require representations capable of capturing coherent wavepacket motion across multiple coupled surfaces. Adiabatic representations diagonalize the electronic Hamiltonian at each nuclear geometry, giving rise to derivative couplings that can become large and formally divergent near conical intersections, whereas diabatic representations minimise derivative couplings and instead introduce explicit off-diagonal potential couplings [83–85]. For grid-based time-dependent simulations, diabatic pictures are often advantageous, as electronic couplings remain local in coordinate space and avoid singular derivative terms [86]. The vibronic model of pyrazine, studied in Chapter 3, exemplifies this regime.

Infrared (IR) spectroscopy examined in Chapter 4 probes vibrational transitions within a single electronic surface. The absorption of IR radiation induces transitions between vibrational levels through the dipole operator. Although conceptually simpler than nonadiabatic photoexcitation, accurate IR simulations still remain computationally demanding for polyatomic systems due to the exponential growth of the vibrational configuration space [87].

1.1.3 Quantum Computing for Chemical Simulation

The principal distinction between classical and quantum computation lies in how quantum states are encoded and manipulated. A classical description of a general many-body quantum state requires the storage and processing of an exponentially large set of amplitudes, rendering exact simulation intractable beyond modest system sizes. By contrast, a quantum computer encodes these amplitudes directly within the state of a qubit register whose Hilbert space dimension grows exponentially with qubit number. Through coherent unitary operations and quantum interference, such devices evolve the full state vector without explicitly representing it in classical memory. This structural difference underpins the long-standing expectation that quantum computers may offer substantial advantages for chemical simulation [88, 89].

At present, quantum hardware remains in the noisy intermediate-scale quantum (NISQ) era [90], characterised by devices comprising tens to several hundreds of qubits with limited coherence times and non-negligible gate errors. Within this setting, variational hybrid algorithms [91–94] that combine parametrised quantum circuits with classical optimisation have been widely explored for ground-state electronic structure calculations. These approaches are typically formulated in second quantization, where Hamiltonians are expressed in terms of fermionic creation and annihilation operators defined over a finite orbital basis and mapped to Pauli operators via fermion-to-qubit transformations [95–98]. First-quantized approaches [76, 99–101] instead encode particle coordinates explicitly, for example through discretised real-space grids or plane-wave bases. While orbital-based methods are commonly applied to stationary eigenstate problems, grid-based

encodings are naturally suited to wavepacket propagation. The grid-based approach developed in this thesis belongs to this latter category and is specifically oriented toward real-time dynamics.

Looking beyond NISQ, scalable quantum advantage is expected to rely on fault-tolerant architectures supporting deep circuits and error-corrected logical qubits [102–105]. In this regime, algorithms based on phase estimation, qubitization, and LCU techniques have been extensively analysed [106–109], providing controllable error bounds and well-defined asymptotic resource scaling. Rigorous resource estimation under fault-tolerant assumptions has become a central task in assessing the long-term feasibility of quantum algorithms [110, 111]. Accordingly, our SO–QFT framework is designed to remain compatible with fault-tolerant circuit constructions while enabling systematic evaluation of resource scalability.

1.2 Motivation

Quantum simulation is often hailed as a transformative opportunity for chemistry, yet the route from promise to practice depends critically on the availability of well-structured algorithms. Particularly, quantum algorithms for performing time-dependent tasks have attracted considerable interest [76, 112–115], with the grid-based SO-QFT method representing one of the most compelling approaches suitable for future applications on fault-tolerant quantum devices. Despite its significant potential, a systematic assessment, spanning grid-based state preparation, SO-QFT time propagation, and measurement of time-dependent properties, remains incomplete across diverse categories of chemical problems.

The first motivation of my research is therefore to develop an end-to-end quantum algorithm centred on the grid-based SO-QFT backbone, and test its algorithmic variants in a range of contexts. Representative domains examined in this thesis engages with the framework in different ways, covering topics from vibronic and pure vibrational dynamics to Coulombic dynamics, and together they reveal our algorithm's scope of applicability and clarify its scalability.

Apart from the algorithmic completeness, the emphasis should also be placed on resource predictability. For chemists and hardware developers alike, the critical question is not merely whether a quantum algorithm works, but whether its cost can be predicted, justified, and aligned with physical accuracy demands. A further motivation then lies in the need for cost evaluations. For grid-based SO-QFT to be more than a conceptual construct, it must be accompanied by quantitative resource analyses that translate simulation requirements into qubit counts, circuit depths, and measurement overheads.

In summary, by exploring the versatility in multiple problem classes, by validating algorithmic variants appropriate to each through classical emulation, and by charting credible resource benchmarks, this work aims to establish the grid-based SO-QFT algorithm as a broadly applicable, resource-transparent framework for time-dependent simulations, and build the foundations for the next phase: its eventual deployment on quantum computers for problems beyond classical reach.

1.3 Research Overview

In this thesis, we build three study lines that keep the backbone fixed and vary the research areas to probe different operators, Hamiltonian structures, and observable requirements. All studies share the same three-stage architecture: compact initial state preparation within grid-based spaces; efficient time evolution via trotterized SO-QFT method; and extraction of observable quantities from autocorrelation functions. Throughout, we employ classical emulation to calibrate accuracy–cost trade-offs and to report quantum resource profiles that can inform hardware roadmaps.

The first study demonstrates the end-to-end feasibility of our algorithm in simulating vibronic dynamics and derives generalised scaling formulae for qubit budget and gate depth calculations. The second study adapts the workflow to infrared spectra by embedding non-unitary dipoles and incorporating higher-order polynomial terms in the potential. The third study extends the grid-based SO-QFT framework to Coulombic systems where singularities dominate, with long-time stability and high fidelity guaranteed by our tailored corrections on the Hamiltonian

and the wavefunction. After the Introduction and a dedicated Basic Simulation Framework chapter, the thesis proceeds along these three lines in separate chapters, and concludes with comprehensive insights and future outlook.

2
Basic Simulation Framework

Contents

This chapter outlines the algorithmic framework underlying all subsequent research in this thesis, in order to provide a unified account of the foundational principles recurring throughout. The framework combines three essential components: quantum state encoding in a grid basis, Hamiltonian propagation via the SO-QFT scheme, and measurement of time-dependent autocorrelation functions as the central class of observables. Collectively, these elements constitute an end-to-end workflow for later use in Chapters 3-5.

2.1 Grid-Based Representation of Quantum States

In both classical and quantum computational frameworks, grid-based representations frequently utilise plane wave basis functions due to their completeness, orthogonality, and compatibility with periodic boundary conditions. Specifically, we consider a truncated momentum basis of finite 2ρ states, $|j\rangle$, each corresponding to a plane wave function:

$$\phi_j(x) = L^{-\frac{1}{2}} e^{i\frac{2\pi x}{L}j}, \tag{2.1}$$

where $j \in \{-\rho, \ldots, \rho - 1\}$ and $i = \sqrt{-1}$ denotes the imaginary unit. Here L represents the length of the position space, which is chosen to ensure negligible boundary amplitude during the time evolution. Upon application of the inverse Fourier transform, these momentum-space basis states are mapped to a set of dual states $|k\rangle$:

$$\phi_k(x) = \frac{1}{\sqrt{2\rho}} \sum_{j=-\rho}^{\rho-1} e^{-i\frac{2\pi j}{L}x_k} \phi_j(x), \tag{2.2}$$

where each 'pixel function' $\phi_k(x)$ in the position space is sharply peaked at the grid position $x_k = \frac{kL}{2\rho}$. As $2\rho \to \infty$, these pixel functions converge to exact Dirac delta functions: $\phi_k(x) \to \delta(x - x_k)$. In practical use, each position grid point is associated with a single amplitude of the wavefunction, assuming that the pixel function is negligible away from its central peak (i.e., $\phi_k(x) = 0$ at all $x_{m\neq k}$ points and only peaked at x_k) [69].

Unlike classical bits, which take values of 0 or 1 exclusively, each qubit on quantum hardware can exist in a superposition of two states, thereby enabling simultaneous representation of both $|0\rangle$ and $|1\rangle$. This property implies that the 2ρ grid points can be encoded using only $\log_2(2\rho)$ qubits, whereas classical storage requires exactly 2ρ bits. More generally, if we define a register as a collection of qubits encoding a given degree of freedom, then an n-qubit register builds a Hilbert space of 2^n grid points. These discretised coordinates $\{x_k\}$ are mapped to computational basis states

$$|k\rangle = |k_{n-1}k_{n-2}\cdots k_1 k_0\rangle\,, \tag{2.3}$$

where each $|k_j\rangle$ denotes the state of an individual qubit. The integer k indexes the grid points and is related to the qubit states through the binary expansion

$$k = k_0 2^0 + \cdots + k_{n-1} 2^{n-1}. \tag{2.4}$$

Since each $k_j \in \{0, 1\}$, the register yields 2^n possible values of k, in one-to-one correspondence with the 2^n grid points.

Extending this construction to multiple dimensions, the system size depends not only on the discretisation per dimension but also on the total number of degrees of freedom. By allocating n qubits per register, a d-dimensional system requires only dn qubits, demonstrating linear scaling with dimensionality, in contrast to the exponential 2^{dn} bits required classically.

For a given discrete wavefunction defined over 2^n grid points, the amplitude c_k at each point x_k is encoded as the probability of the corresponding qubit state $|k\rangle$,

$$\underbrace{\sum_{k=0}^{2^n-1} c_k \, |x_k\rangle}_{\text{pixels in grid-based space}} \quad = \quad \underbrace{\sum_{k=0}^{2^n-1} c_k \, |k\rangle}_{\text{amplitudes in quantum computer}} \quad , \tag{2.5}$$

with the number of stored amplitudes growing exponentially with the total qubit count n. While the grid-based representation of quantum states is outlined here only at a conceptual level, the explicit discussion of initial state preparation on quantum architectures is deferred to later chapters where it is naturally incorporated into the corresponding studies.

2.2 SO-QFT Scheme for Time Evolution

The SO-QFT scheme partitioned the time evolution operator into alternating kinetic and potential operator actions, from which inherent errors occur due to the non-commutativity between the decomposed Hamiltonian terms. Based on the first-order Lie–Trotter product formula [116], many further studies were conducted to develop high-order variations [117–119] and characterise the Trotter error [120–122]. Adopting a second-order form [123–125] bounds this error scaling within $\mathcal{O}(dt^3)$:

$$e^{-iHdt} = e^{-iVdt/2} e^{-iKdt} e^{-iVdt/2} + \mathcal{O}(dt^3), \tag{2.6}$$

where the Hamiltonian takes the form $H = K + V$, and dt denotes the spacing interval between adjacent discrete time points during evolution. Within one time step dt, this symmetric decomposition proceeds through (i) a half-step potential segment $e^{-iVdt/2}$, (ii) a full-step kinetic component e^{-iKdt}, and (iii) a concluding half-step potential update $e^{-iVdt/2}$. The gate complexity associated with implementing the relevant unitary time-evolution operators on quantum hardware necessarily depends on the specific structure of the Hamiltonian. A detailed treatment of the corresponding circuit constructions and gate-depth estimates will therefore be provided in subsequent chapters in the context of each research problem.

The kinetic and potential components are applied in momentum and position spaces respectively, where they are local and diagonal-dominant matrices and thus significantly easier to evaluate. Conversion between two spaces is effected through forward or inverse Fourier Transform (FT):

$$\Psi(t+dt) \approx e^{-\frac{iVdt}{2}} \mathrm{FT}^{-1} e^{-iKdt} \mathrm{FT} e^{-\frac{iVdt}{2}} \Psi(t).$$

On classical hardware, this operation is typically realised via Fast Fourier Transform (FFT), with a computational cost scaling as $\mathcal{O}(n2^n)$ for a vector of size $N = 2^n$. On the other hand, quantum hardware executes the discrete Fourier transform through QFT. As outlined in Figure 2.1, its circuit for an n-qubit register consists of two essential components: n Hadamard gates $\mathbf{H}$, and $\frac{n\times(n-1)}{2}$ controlled rotation gates $\mathbf{R}$ [126]. Here a $\mathbf{H}$ gate transforms a qubit state $|k_j\rangle$ into a superposition as

$$\mathbf{H}\,|k_j\rangle = \frac{1}{\sqrt{2}}\left(|0\rangle + (-1)^{k_j}\,|1\rangle\right) = \frac{1}{\sqrt{2}}\left(|0\rangle + e^{\frac{2\pi i k_j}{2}}\,|1\rangle\right),\ k_j \in \{0,1\};$$

and a controlled $\mathbf{R}_a$ gate applies phase shifts on the $|1\rangle$ state of the target qubit, conditional on the control qubit state $|k_l\rangle$:

$$\mathbf{R}_a(|0\rangle + |1\rangle) = (|0\rangle + e^{\frac{2\pi i k_l}{2^a}}\,|1\rangle),\ k_l \in \{0,1\}.$$

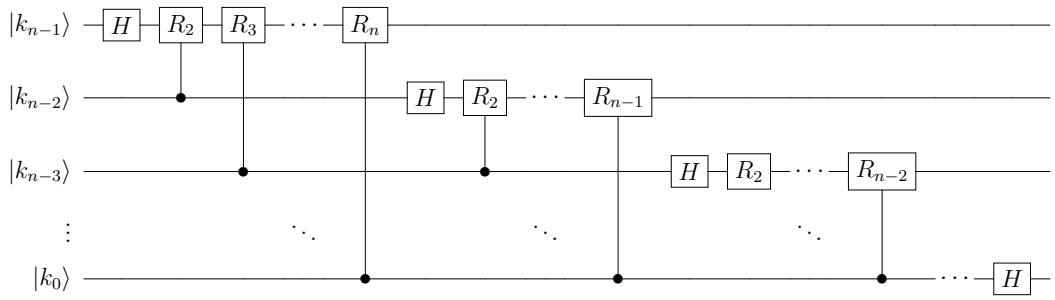

Figure 2.1: Illustrative QFT circuit for an n-qubit register.

In this circuit, the first n gates acting on k_{n-1} qubit evolve the states as follows:

$$\begin{aligned}
&|k_{n-1}k_{n-2}\dots k_1k_0\rangle \\
\xrightarrow{\mathbf{H}}\ &\frac{1}{\sqrt{2}}\left(|0\rangle + e^{\frac{2\pi i k_{n-1}}{2^1}}|1\rangle\right)\bigotimes|k_{n-2}\dots k_1k_0\rangle \\
\xrightarrow{\mathbf{R_2}}\ &\frac{1}{\sqrt{2}}\left(|0\rangle + e^{\frac{2\pi i k_{n-2}}{2^2}}e^{\frac{2\pi i k_{n-1}}{2^1}}|1\rangle\right)\bigotimes|k_{n-2}\dots k_1k_0\rangle \\
&\vdots \\
\xrightarrow{\mathbf{R}_n}\ &\frac{1}{\sqrt{2}}\left(|0\rangle + e^{\frac{2\pi i k_0}{2^n}}\cdots e^{\frac{2\pi i k_{n-2}}{2^2}}e^{\frac{2\pi i k_{n-1}}{2^1}}|1\rangle\right)\bigotimes|k_{n-2}\dots k_1k_0\rangle\,.
\end{aligned} \tag{2.7}$$

Dividing both sides of Eq. 2.4 by 2^n, we obtain

$$\frac{k}{2^n} = \frac{k_0}{2^n} + \frac{k_1}{2^{n-1}} + \dots \frac{k_{n-1}}{2^1}.$$

When this relation is substituted into the last line of Eq. 2.7, the expression becomes:

$$\frac{1}{2^{1/2}}\left(|0\rangle + e^{2\pi i\frac{k}{2^n}}|1\rangle\right)\bigotimes|k_{n-2}\dots k_1k_0\rangle\,.$$

The subsequent gate sequences evolve the remaining qubits analogously, converting each $|k_j\rangle$ into $|0\rangle + e^{2\pi i\frac{k}{2^{j+1}}}|1\rangle$. The overall action of the circuit is therefore

$$\mathrm{QFT}\,|k_{n-1}k_{n-2}\dots k_1k_0\rangle = \frac{1}{2^{n/2}}\bigotimes_{j=0}^{n-1}\left(|0\rangle + e^{2\pi i k\frac{1}{2^{j+1}}}|1\rangle\right). \tag{2.8}$$

The circuit in Figure 2.1 is presented with a reversed qubit order for clarity, where the least significant qubit $|k_0\rangle$ is positioned at the bottom and the most significant $|k_{n-1}\rangle$ at the top. While the figure does not explicitly include the SWAP gates required to restore the correct qubit ordering, these operations contribute an additional $\frac{n}{2}$ gates for even n. For odd n, we don't have to swap the middle

qubit, then the the gate count reduces to $\frac{n-1}{2}$. After SWAP operations, the original computational basis $|k\rangle$ has been mapped to the Fourier basis $|b\rangle$:

$$|k_{n-1}k_{n-2}\cdots k_1k_0\rangle \to \frac{1}{2^{n/2}} e^{2\pi ik(\frac{b_0}{2^n}+\frac{b_1}{2^{n-1}}+\cdots+\frac{b_{n-2}}{2^2}+\frac{b_{n-1}}{2^1})} |b_{n-1}b_{n-2}\cdots b_1b_0\rangle ,$$

$$\text{i.e., } |k\rangle \to \frac{1}{\sqrt{N}} \sum_{b=0}^{N-1} e^{2\pi ik\frac{b}{N}} |b\rangle , \text{ with } N = 2^n,$$

which is exactly the output of a discrete Fourier transform. The inverse QFT circuit follows a straightforward reversal of operations, applying $\mathbf{R}^{-1}$ from right to left. To conclude, for one forward or inverse QFT block, its gate depth is calculated to be

$$\begin{cases} n^2/2 + n, & \text{if } n \text{ even}, \\ n^2/2 + n - 1/2, & \text{if } n \text{ odd}. \end{cases}$$

Thus, the QFT exhibits a quadratic complexity of $\mathcal{O}(n^2)$, vastly outperforming the classical FFT, which requires $\mathcal{O}(n2^n)$ operations for the same system size.

2.3 Autocorrelation Function and Measurement

While the SO–QFT scheme efficiently implements time evolution on quantum registers, it is important to recognise that the resulting state is not directly accessible. In contrast to classical simulations, where the full wavefunction can be inspected at will after time propagation, a quantum computer encodes the state implicitly in the amplitudes of a superposition across qubits. Directly reading out these amplitudes is not possible: any measurement irreversibly collapses the superposition to a single computational basis outcome, i.e. a specific grid index drawn from the associated probability distribution, rather than the complete wavefunction. Reconstructing the full wavefunction would require exponentially many measurements via quantum state tomography [127], thereby negating the potential advantage.

Consequently, quantum simulation does not aim to recover the entire wavefunction, but instead to estimate expectation values or phase information from repeated circuit executions. This constraint fundamentally shapes the design of our algorithm and naturally leads to the use of autocorrelation functions as primary

observables. In the time-dependent picture, they capture wavepacket recurrences, i.e., overlaps of the evolving state at time t with its initial state at $t = 0$ [128]:

$$A(t) = \langle \Psi(0) | \Psi(t) \rangle = \langle \Psi(0) | e^{-iHt} | \Psi(0) \rangle. \tag{2.9}$$

All research problems in this thesis exploit this function to extract a wide array of physical properties: for ground states evolved under the corresponding Hamiltonians, the time-domain autocorrelation $A(t)$ serves to quantify evolution fidelity in terms of energy conservation and dynamical stability; in molecular spectroscopy applications, the Fourier transform of $A(t)$ delivers vibronic and vibrational spectra that can be directly compared with experimental results.

On quantum platforms, the extraction of autocorrelation values corresponds to the measurement stage of the relevant quantum algorithms and is typically realised through the single-ancilla Hadamard test. The Hadamard test is an interferometric technique widely adopted for extracting inner products and expectation values [129–133]. It works by preparing an ancillary qubit in a superposition state, applying controlled operations conditioned on this qubit, and computing the real or imaginary part of the overlap from measurement statistics of the ancilla.

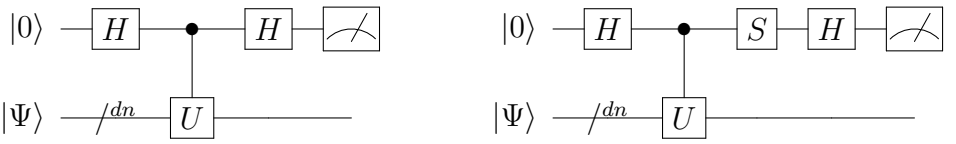

(a) $\mathbb{R}\mathrm{e}\{A(t)\} = P_{|\text{ancilla}\rangle}(0) - P_{|\text{ancilla}\rangle}(1)$ **(b)** $\mathbb{I}\mathrm{m}\{A(t)\} = P_{|\text{ancilla}\rangle}(1) - P_{|\text{ancilla}\rangle}(0)$

Figure 2.2: Ancilla-assisted measurement (Hadamard test) of (a) the real part and (b) the imaginary part of the autocorrelation at a specific time point. Here $P_{|\text{ancilla}\rangle}(0)$ and $P_{|\text{ancilla}\rangle}(1)$ represent the probability of measuring the ancilla in state $|0\rangle$ and $|1\rangle$.

We present the circuit of the Hadamard test in Figure 2.2; given a time-evolution unitary $U(t)$ controlled by a single ancillary qubit, the phase acquired by the state during the evolution is encoded in the ancillary qubit. The left panel transforms the system

$$\text{from } |0\rangle |\Psi\rangle \text{ to } \frac{1}{2}[(I+U)|0\rangle + (I-U)|1\rangle] |\Psi\rangle .$$

Specifically, the difference in measurement probabilities of the ancilla being found in $|0\rangle$ and $|1\rangle$ directly yields the real part of the autocorrelation:

$$\begin{aligned}
&P_{|\text{ancilla}\rangle}(0) - P_{|\text{ancilla}\rangle}(1) \\
&= \frac{1}{4}\langle\Psi(0)|\,(I+U)^\dagger(I+U)\,|\Psi(0)\rangle - \frac{1}{4}\langle\Psi(0)|\,(I-U)^\dagger(I-U)\,|\Psi(0)\rangle \\
&= \frac{1}{2}\langle\Psi(0)|\,U+U^\dagger\,|\Psi(0)\rangle \\
&= \mathbb{R}\mathrm{e}\{\langle\Psi(0)|\,U\,|\Psi(0)\rangle\} \\
&= \mathbb{R}\mathrm{e}\{\langle\Psi(0)|\Psi(t)\rangle\}.
\end{aligned} \tag{2.10}$$

The determination of $P_{|\text{ancilla}\rangle}(0)$ and $P_{|\text{ancilla}\rangle}(1)$ at each chosen time point relies on repeated measurements, with the statistics accumulated over multiple shots.

To obtain the imaginary counterpart, we need only add an $\mathbf{S}$ gate on the ancilla after the controlled operation and before the final Hadamard gate, as depicted in the right panel of Figure 2.2. With $\mathbf{S}\,|0\rangle = |0\rangle$ and $\mathbf{S}\,|1\rangle = i\,|0\rangle$, this circuit converts the system

$$\text{from } |0\rangle\,|\Psi\rangle \text{ to } \frac{1}{2}[(I+iU)\,|0\rangle + (I-iU)\,|1\rangle]\,|\Psi\rangle\,.$$

As with the real component, the imaginary part of the autocorrelation is obtained by evaluating probability differences following:

$$\begin{aligned}
&P_{|\text{ancilla}\rangle}(1) - P_{|\text{ancilla}\rangle}(0) \\
&= \frac{1}{4}\langle\Psi(0)|\,(I-iU)^\dagger(I-iU)\,|\Psi(0)\rangle - \frac{1}{4}\langle\Psi(0)|\,(I+iU)^\dagger(I+iU)\,|\Psi(0)\rangle \\
&= \frac{1}{2}\langle\Psi(0)|\,iU^\dagger - iU\,|\Psi(0)\rangle \\
&= \mathbb{I}\mathrm{m}\{\langle\Psi(0)|\,U\,|\Psi(0)\rangle\} \\
&= \mathbb{I}\mathrm{m}\{\langle\Psi(0)|\Psi(t)\rangle\}.
\end{aligned} \tag{2.11}$$

On the other hand, the multiple-ancilla Quantum Phase Estimation (QPE) [52, 88, 134, 135] is commonly used to determine eigenphases of unitary operators. Given $U|\psi\rangle = e^{i\phi}|\psi\rangle$, it employs a register of ancillary qubits to control successive powers of U, followed by an inverse QFT that maps phase information ϕ onto the computational basis of the ancilla register. Measurement of this register yields an estimate of the eigenphases present in the input state, with precision improving

exponentially with the number of ancillary qubits. This technique lies at the core of many quantum algorithms, and its specific implementations and error analyses have been extensively studied [106, 136–138].

In the context of this thesis, the Hadamard test facilitates the evaluation of autocorrelation functions at discrete time steps. This approach involves relatively shallow circuits and minimal ancillary overhead, but requires repeated measurements across multiple time steps. QPE offers an alternative route in which spectral information can be estimated directly without explicit time-domain sampling, but at the expense of deeper circuits and increased ancilla resources.

2.4 Limitations of the Present Framework

The quantum framework developed above should be situated within a broader landscape of established classical approaches. Techniques such as Multi-configuration Time-Dependent Hartree (MCTDH) [139–141], tensor-train network [142–144], Krylov-subspace propagation [145–147], and polynomial-expansion schemes [14, 148, 149] have demonstrated high efficiency for systems of moderate dimensionality. By exploiting structured basis representations and adaptive truncation strategies, these methods can delay the onset of exponential scaling in practice [11]. The prospective quantum advantage therefore emerges primarily in regimes with high dimensionality and long evolution times, where classical compression strategies fail to maintain tractability.

Unlike classical simulations where the full wavefunction is accessible at all times for arbitrary post-processing, intermediate state inspection is generally unavailable for quantum algorithms. Only final measurement statistics of selected observables can be obtained, at the cost of nontrivial sampling overhead. Moreover, the observable extraction, whether through Hadamard test or QPE, relies on controlled time-evolution operators. These global controls introduce additional circuit-depth costs by limiting opportunities for parallel execution of gates acting on disjoint registers.

The practical advantage of quantum algorithms is therefore intrinsically regime-dependent, shaped by system dimensionality, required evolution time, observable design, and measurement-induced sampling requirements. These considerations frame the resource analyses presented in the following chapters and motivate the critical appraisal of broader limitations in Chapter 6.

3

Multi-Mode Vibronic Dynamics under Conical Intersections

Contents

The work of this chapter has been submitted for publication. Minor editorial changes have been made to conform to the formatting of this thesis.

3.1 Introduction

In this chapter, we numerically investigate an end-to-end error-corrected, fault-tolerant digital quantum simulation of molecular photo-electron absorption spectra and the associated state population dynamics after photo-excitation, focusing on efficient quantum circuit design, feasibility assessments and cost estimations. We choose the pyrazine molecule as a case study because it is a well-studied prototypical system in photoinduced vibronic dynamics, featuring well-characterised inter-state transitions via the conical intersection. The availability of extensive experimental and theoretical data allows us to validate our simulation framework and directly compare it with existing results in the literature.

As one of the essential building blocks of many organic compounds [150], different abstractions of pyrazine have been explored and the *ab initio* Potential Energy Surfaces (PES) have been characterised using Complete Active Space Self Consistent Field (CASSCF), Multi-Reference Configuration Interaction (MRCI), Second-Order Møller-Plesset Perturbation Theory (MP2) and Configuration Interaction Singles (CIS) techniques [151, 152]. Many standard techniques for modelling molecular quantum dynamics on conventional computers have been applied to this system, including the path integral approach [153, 154], the Multi-configuration Time-Dependent Hartree (MCTDH) method [155–158], semiclassical descriptions [159], Time-Dependent Discrete Variable Representation (TDDVR) approach [160], Matching-Pursuit/Split Operator-Fourier Transform (MP/SOFT) methods [161], and also short-time trajectories techniques [162–164].

Among these aforementioned approaches, the grid-based SO-FT method stands out because it can be straightforwardly translated into a quantum algorithm by performing the QFT in place of the discrete Fourier transform. The SO-QFT approach is well-suited to vibrational dynamics, because, in contrast to electronic wavefunctions, the quantum states do not exhibit derivative discontinuities and accurate grid-based representations can be realised with relatively few qubits per degree of freedom.

While pyrazine in a reduced dimensional representation is considered a classically 'solved' problem, understanding the requirements for performing a quantum simulation of this model helps us to extrapolate to more meaningful systems, where classical computers are expected to struggle. We first assess the performance of the grid-based SO-QFT method for the quality of the pyrazine spectrum and the accuracy of the population dynamics. Since grid-based modelling has been widely discussed as a potential application area for fault-tolerant quantum computers, this work focuses on illustrating the quantum implementation of our algorithm and evaluating the quantum resources required. Specifically, we examine initial state preparation, circuit design for the time-evolution process, appropriate measurement techniques of both absorption spectra and population dynamics, and present the corresponding calculations of relevant gate depths.

3.2 Systems and Observables

3.2.1 The Pyrazine Photosystem

The three lowest-energy electronic states of pyrazine are the ground state S_0, the dark S_1 $n\pi^*$ state, and the bright S_2 $\pi\pi^*$ state. Photo-excitation from the ground S_0 state initially populates the S_2 state, after which the vibronic coupling between the S_2 and S_1 states triggers an extremely fast and efficient $S_2 \rightarrow S_1$ internal conversion process resulting in a broadband S_2 absorption spectrum and significant population transfer from the S_2 to the S_1 state [158, 159, 163].

The conical intersection of the S_1 and S_2 states of pyrazine has been thoroughly characterised in previous studies [151, 165–169]. A full 24-dimensional vibronic model Hamiltonian has also been developed based on *ab initio* calculations [151, 156, 160, 170]. Of the 24 vibrations, only 4 of the modes $\nu_{6a}, \nu_1, \nu_{9a}, \nu_{10a}$ (see Figure 3.1) are directly active in the dynamics and are sufficient for a low-dimensional, qualitative description of the vibronic spectrum [151, 155, 159, 171]. According to group-theoretical considerations, totally symmetric modes ($\nu_{6a}, \nu_1, \nu_{9a}$) modulate the energy separation between S_1 and S_2 states without mixing the electronic states

and therefore act as tuning modes. The non-totally symmetric ν_{10a} mode induces inter-state mixing and provides the primary vibronic coupling channel [151, 153].

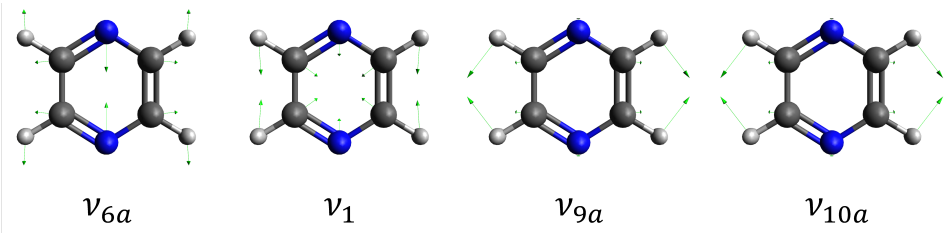

Figure 3.1: The four normal modes included in the 4D model Hamiltonian of pyrazine.

The terms of the 4D linear vibronic model Hamiltonian of pyrazine are collected into diagonal kinetic and potential terms, and off-diagonal coupling terms:

$$H = \underbrace{-\sum_k \frac{\omega_k}{2}\frac{\partial^2}{\partial Q_k^2}}_{K} + \underbrace{\begin{pmatrix} V_{S1} & 0 \\ 0 & V_{S2} \end{pmatrix}}_{V_{\text{diag}}} + \underbrace{Q_{10a}\begin{pmatrix} 0 & \lambda \\ \lambda & 0 \end{pmatrix}}_{V_{\text{c}}} \tag{3.1}$$

where

$$V_{S1} = -\Delta + \sum_j \kappa_j^{(1)} Q_j + \frac{1}{2}\sum_k \omega_k Q_k^2 \tag{3.2}$$

$$V_{S2} = \Delta + \sum_j \kappa_j^{(2)} Q_j + \frac{1}{2}\sum_k \omega_k Q_k^2 \tag{3.3}$$

and $k \in \{6a, 1, 9a, 10a\}$, $j \in \{6a, 1, 9a\}$. Here, the coordinates Q_k are the dimensionless ground-state normal-mode coordinates, and this Hamiltonian is constructed in a diabatic representation, where the nonadiabatic effects are incorporated as coordinate-dependent off-diagonal potential terms. In this model, the vibrational modes are approximated as displaced harmonic oscillators, while the electronic subspace is spanned by the two excited states:

$$|S_1\rangle : \begin{pmatrix} 1 \\ 0 \end{pmatrix}, \quad |S_2\rangle : \begin{pmatrix} 0 \\ 1 \end{pmatrix}, \tag{3.4}$$

with 2Δ denoting the vertical energy gap between the two states at the reference geometry. The vibrational frequencies ω are derived from the MP2 ground-state Hessian. The intra-state coupling constants κ correspond to excited-state energy gradients evaluated at the MRCI level. The inter-state coupling constant λ is extracted by least-squares fitting of the vibronic Hamiltonian to the MRCI adiabatic

energies along Q_{10a}. The complete parameter set follows Woywod et al. [151] and Worth et al [155], and is listed in Table 3.1.

$\lambda = 0.1825$, $\Delta = 0.4617$			
	ω	$\kappa^{(1)}$	$\kappa^{(2)}$
ν_{6a}	0.0740	-0.0964	0.1194
ν_1	0.1273	0.0470	0.2012
ν_{9a}	0.1568	0.1594	0.0484
ν_{10a}	0.0936	\	\

Table 3.1: Values of parameters $\{\omega, \kappa, \lambda, \Delta\}$ used in the 4D model Hamiltonian (units: eV).

The initial wavepacket is the vibrational ground state of the harmonic S_0 potential, projected onto the S_2 state. In the position space, it is represented as a tensor product state on a uniform five-dimensional rectangular grid, consisting of four normal mode coordinates $\mathbf{Q}$ and one electronic state coordinate s:

$$\Psi(\mathbf{Q}s, t = 0) = \left(\bigotimes_k \psi(Q_k) \right) \otimes |S_2\rangle \,, \tag{3.5}$$

where each $\psi(Q_k)$ is a Gaussian ground state.

3.2.2 Observable Properties

Under the Franck–Condon approximation [172–175], the intensities of vibronic spectra are given by the vibronic transition moments, which are proportional to the overlap of the Born–Oppenheimer vibrational states in the two electronic PESs [176]. In this framework, vertical excitation occurs under the sudden approximation, where the initial state for time-evolution is the zero point vibrational wavefunction of the S_0 PES projected into the S_2 electronic PES [177]. The initial wavefunction is propagated with the 4D Hamiltonian for the S_1-S_2 system and the absorption spectrum is given by the Fourier transform of the autocorrelation function of the wavefunction [155]:

$$I(\omega) \propto \int_{-\infty}^{\infty} \langle \Psi(0) | \Psi(t) \rangle \, e^{i\omega t} \mathrm{d}t. \tag{3.6}$$

This is a Franck–Condon weighted vibronic spectrum of the Hamiltonian, rather than a full absorption cross-section, since the transition dipole is assumed to be coordinate-independent and therefore factors out of the dynamics. Population dynamics are extracted directly from the probability distribution across the S_1 and S_2 states.

It is worth clarifying why a time-dependent formulation is adopted to obtain the absorption spectrum of a time-independent Hamiltonian. In classical approaches, one may instead directly diagonalize the Hamiltonian to determine its eigenvalues and eigenvectors, and then assemble the spectrum from transition matrix elements between eigenstates. The time-domain autocorrelation used here is formally equivalent: expanding the propagated state in the eigenbasis of H as $|\Psi(t)\rangle = \sum_x c_x e^{-iE_x t}|x\rangle$, the autocorrelation function reads $A(t) = \sum_x |c_x|^2 e^{-iE_x t}$, so that its Fourier transform recovers the spectral distribution associated with E_x.

Rather than explicitly resolving the full eigenbasis, the time-dependent approach extracts spectral information from repeated applications of unitary propagators. On quantum hardware, unitary time evolution constitutes a native operation, whereas matrix diagonalization has no straightforward analogue at the circuit level. The propagation-based framework therefore aligns naturally with the operational primitives available on quantum computers, providing a representation compatible with scalable quantum architectures.

Lines in the experimental spectra are broadened due to spectrometer resolution and the inherent ultrafast photorelaxation of the system. Since the 4D model neglects the other 20 normal modes, which are responsible for fast vibrational relaxation, homogeneous phenomenological broadening is accounted for by multiplying the autocorrelation function in the integrand of Eq. 3.6 by a time-dependent broadening function:

$$B(t) = \exp\left(-\frac{t}{\tau}\right). \tag{3.7}$$

Following previous work on this system, the short effective relaxation time is selected to be $\tau = 30$ fs [155]. In practical simulations the state is evolved for a finite time

T, which gives rise to artificial features in the spectrum resulting from the Fourier Transform in Eq. 3.6. Another damping function:

$$D(t) = \cos\left(\frac{\pi t}{2T}\right) \tag{3.8}$$

that simultaneously adds broadening due to the spectral resolution, and reduces artefacts due to the Gibbs phenomenon is therefore also applied.

3.3 Quantum Implementation

Our goal is to establish and analyse the performance characteristics of the SO-QFT quantum algorithm for computing the absorption spectrum and population dynamics of photo-chemical systems, using the 4D model for pyrazine as a prototypical test case where full classical emulation is feasible. The end-to-end quantum algorithm consists of three steps: preparation of a relevant initial state on a register of qubits; application of the SO-QFT time-propagation circuit; qubit measurement for the extraction of time-dependent system properties. This is summarised in Figure 3.2.

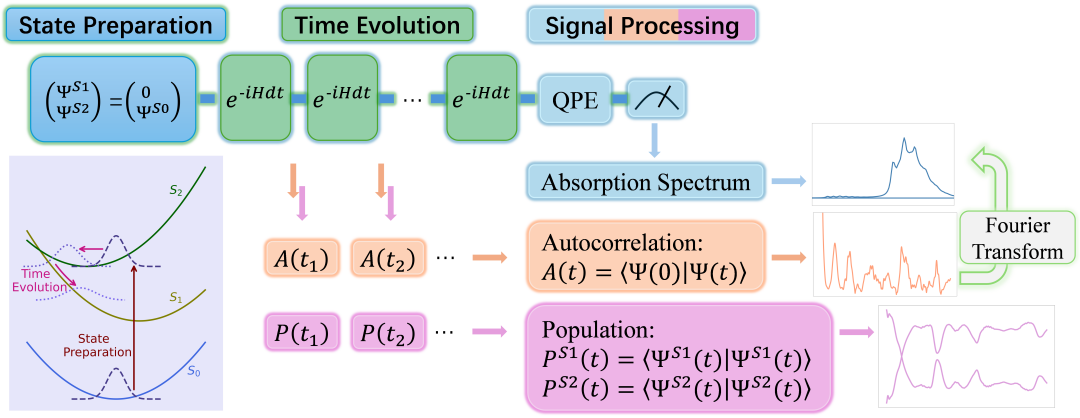

Figure 3.2: Schematic overview of the proposed end-to-end quantum algorithmic framework, comprising three main stages: state preparation, time evolution, and signal processing. Each component is discussed in detail in Sections 3.3.1- 3.3.3.

3.3.1 State Preparation

As shown in Eq. 3.5, the initial state for the model system is the tensor product of independent Gaussian distributions in four normal modes, each centred at $Q = 0$,

and the electronic state vector in the S_2 state. Several efficient approaches have been proposed for preparing Gaussian distributions across the amplitudes of a qubit register, including the uniformly-controlled rotation method [178], the Matrix Product State technique [179], the Fourier Series Loader method [180], the Mid-Circuit Measurement and Reuse scheme [181], the Kitaev-Webb algorithm [182], etc. Here we choose the uniformly-controlled rotation approach, which uses only rotational and **CNOT** gates, and where all the angles of rotational gates are conveniently calculated from the wavefunction amplitudes.

We first allocate 2^n grid points to each normal mode; this is achieved by assigning n-qubit sub-registers to the representation of each normal mode, and therefore dn qubits in total to represent d spatial degrees of freedom:

$$\overbrace{\underbrace{|k_{n-1}\cdots k_2k_1k_0\rangle}_{n\text{-qubit sub-register}}\otimes\underbrace{|k_{n-1}\cdots k_2k_1k_0\rangle}_{n\text{-qubit sub-register}}\otimes\cdots}^{d\text{ sub-registers}}, \tag{3.9}$$

One further qubit is allocated to represent the electronic degree of freedom. The quantum resource for encoding the molecular system counts to $dn + 1$. For our numerical emulations, we select $n = 4$ (i.e., 16 grid points per normal mode, determined through systematic analyses in Section 3.4.1), and the 4D pyrazine model requires overall 17 qubits for the molecular state register.

We then present the details of the quantum circuit and how the angles of gates relate to the wavefunction amplitudes. In our current settings, the amplitudes are all real and positive, and hence only $\mathbf{R_y}$ and **CNOT** gates are needed to load the target wavefunction, as suggested in [178, 180]. For each 4-qubit register, the corresponding quantum circuit is built from four uniformly j-controlled rotation sequences with $j = 0, 1, 2, 3$, as shown in Figure 3.3. Summing over the four j sequences results in a total circuit depth of 29 gates, which generalises to $2^{n+1} - 3$ for an arbitrary n-qubit register.

To be specific, the rotation angle of the u^{th} $\mathbf{R_y}$ gate in the j-controlled rotations are determined by

$$\theta^{(y)}_{3-j,u} = \sum_{w=0}^{2^j-1} M_{uw}\alpha^{(y)}_{3-j,w}, \tag{3.10}$$

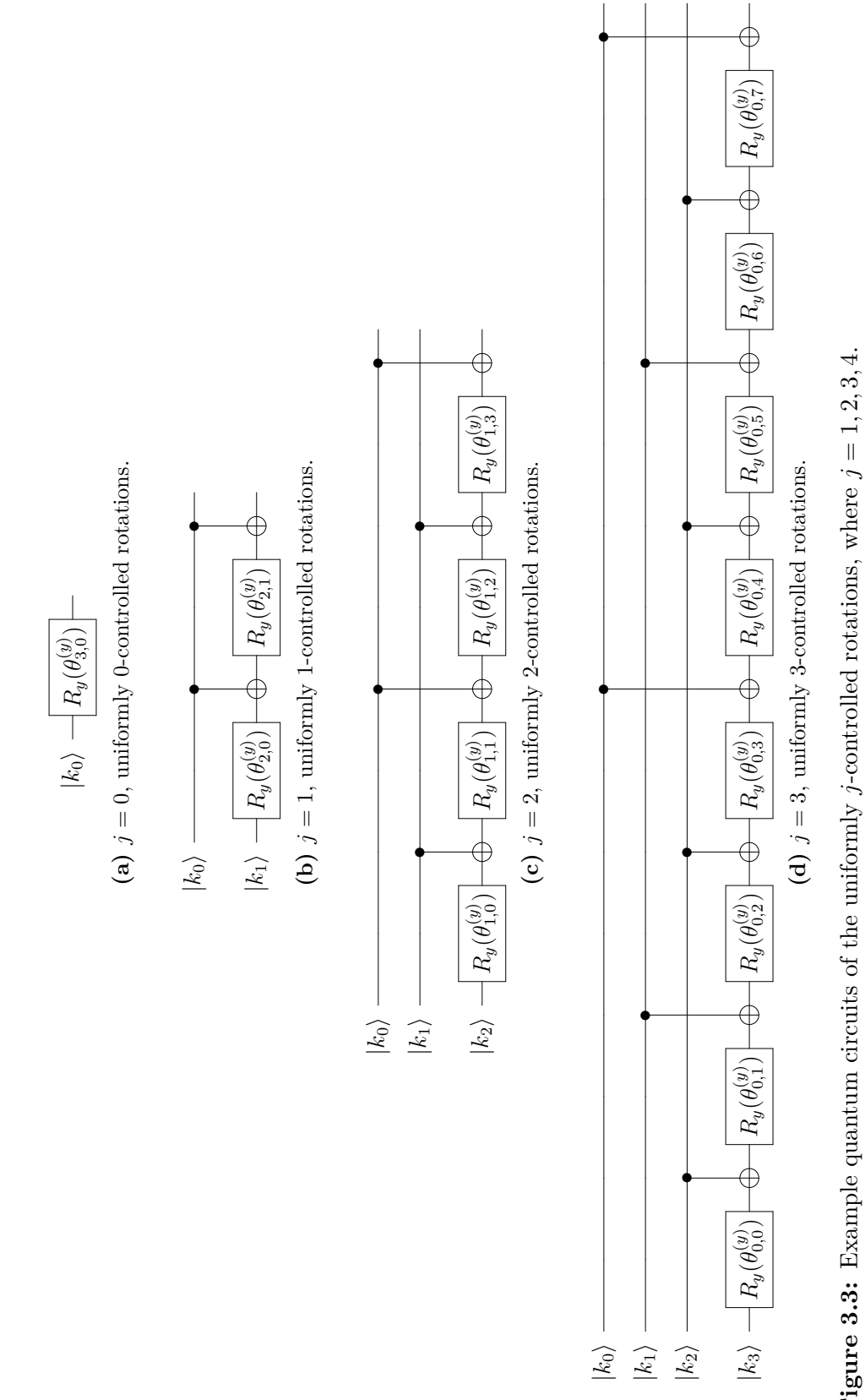

(a) $j = 0$, uniformly 0-controlled rotations.

(b) $j = 1$, uniformly 1-controlled rotations.

(c) $j = 2$, uniformly 2-controlled rotations.

(d) $j = 3$, uniformly 3-controlled rotations.

Figure 3.3: Example quantum circuits of the uniformly j-controlled rotations, where $j = 1, 2, 3, 4$.

where j indicates the target qubit $|k_j\rangle$ of the corresponding $\mathbf{R_y}$ gates. The coefficient $M_{uw} = 2^{-j}(-1)^{b_u g_k}$ contains the binary code b_w and binary reflected Gray code g_u of the integer w and u. By denoting $p = 3 - j$, the $\alpha_{3-j,w}$ is calculated from wavefunction amplitudes according to

$$\alpha_{p,w}^{(y)} = 2 \arcsin \sqrt{\frac{\sum_{l=0}^{2^p-1} |\Psi_{(2w+1)2^p+l}|^2}{\sum_{l=0}^{2^{p+1}-1} |\Psi_{w2^{p+1}+l}|^2}}. \tag{3.11}$$

Here Ψ_r denotes the target wavefunction amplitude associated with the r^{th} computational basis state, i.e. the r^{th} grid point, and the summation index l runs over the ranges explicitly indicated.

To determine the rotation angles of $\mathbf{R_y}$ gates acting on the qubit $|k_j\rangle$ (for fixed j), one first computes the coefficients $\alpha_{p,w}^{(y)} = \alpha_{3-j,w}^{(y)}$ for all $w \in \{0, \cdots, 2^j - 1\}$ according to Eq. 3.11. The rotation angle of a specific $\mathbf{R_y}$ gate, indexed by u and denoted $\theta_{3-j,u}^{(y)}$, is then obtained by combining these $\alpha_{3-j,w}^{(y)}$ values following the rule given in Eq. 3.10.

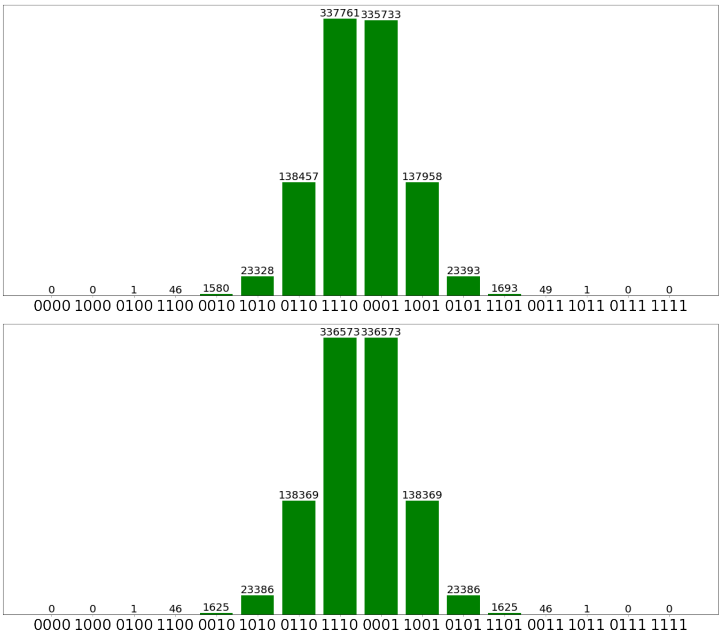

Figure 3.4: Emulated random measurement outcomes of the state preparation circuit with 1×10^6 shots from Qiskit (top panel), and the analytical probability distribution of the target wavefunction (bottome panel).

We demonstrate the veracity of the circuit through emulated random measurement outcomes of the tuning mode state prepared using Qiskit [183]. Taking one of the tuning modes, namely ν_{6a}, as an illustrative example, Figure 3.4 presents the

measurement outcomes from 1×10^6 shots performed on Qiskit. The numerical bar chart aligns exceptionally well with the analytical probability distribution of the target wavefunction. This strong agreement proves the effectiveness and precision of encoding the desired initial harmonic state using uniformly controlled rotations on quantum registers with modest qubits.

The complete state preparation across four normal mode registers consists of four identical uniform-rotation circuits applied in parallel. This procedure readily extends to higher-dimensional vibronic models without additional gate depth or time overhead, as the registers are prepared simultaneously.

3.3.2 Time Evolution

The SO-QFT method has previously been applied to first-quantised real-space quantum simulation of a simplified Marcus model with two coupled 1D harmonic PESs [184]. We extend their time evolution decomposition to second order to obtain

$$e^{-iHdt} \approx U_{\text{diag}} U_{\text{c}} U_{\text{QFT}}^{-1} U_K U_{\text{QFT}} U_{\text{diag}} U_{\text{c}} \tag{3.12}$$

where

$$U_{\text{diag}} = e^{-\frac{iV_{\text{diag}}dt}{2}}, \quad U_{\text{c}} = e^{-\frac{iV_{\text{c}}dt}{2}}, \quad U_K = e^{-iKdt}.$$

The approximation symbol arises from both the splitting between K and V, and the additional factorisation of the non-commuting components V_{diag} and V_{c} within V.

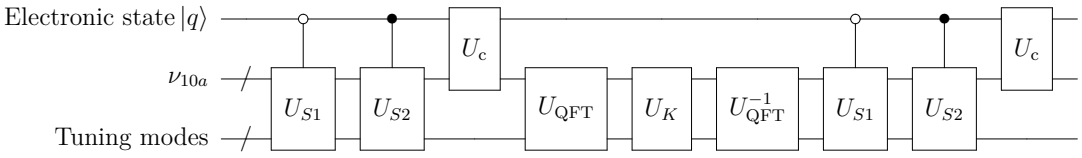

Figure 3.5: Quantum circuit of time evolution for one time step dt.

Figure 3.5 summarises the quantum circuit schematically for one time step. This sequence is repeated n_t time steps to evolve for a total time of $T = n_t dt$. U_{diag} is decomposed into two controlled unitary operators U_{S1} and U_{S2}. As shown in Eq. 3.1, V_{diag} and K involve 0^{th}-, 1^{st}- and 2^{nd}-order polynomial terms in either position or momentum coordinates. Re-writing the time evolution operators by expressing Q

as a binary expansion is equivalent to applying various combinations of elementary gates including $\mathbf{U_1}$, Pauli $\mathbf{X}$ and controlled $\mathbf{R_x}$. The rotation angles are functions of the time resolution and the parameters used in the Hamiltonian.

We now briefly illustrate quantum circuits applicable to the time evolution operators in the 4D model simulation, taking one n-qubit normal mode as an example. Specifically, $\mathbf{U_1}$ gates are frequently used when encoding U_{diag} and U_K. This single-qubit rotation gate applies a phase operation around the Z-axis of the Bloch sphere, with $\mathbf{U_1}(\theta)(\alpha\,|0\rangle + \beta\,|1\rangle) = \alpha\,|0\rangle + e^{i\theta}\beta\,|1\rangle$.

The 0^{th}-order term in V_{diag} builds the energy gap between S_1 and S_2 states by 4 single-qubit gates. Figure 3.6 shows a repetitive sequence of $\mathbf{U_1}(\theta_0)$ gates and Pauli $\mathbf{X}$ gates utilised to apply the constant phase

$$e^{i\theta_0} = e^{-\frac{i(-\Delta)dt}{2}}, \text{ with } \theta_0 = -\frac{-\Delta dt}{2},$$

onto the S_1 state (replace $-\Delta$ by Δ for the S_2 state). As the $\mathbf{U_1}(\theta_0)$ gate only rotates the phase of state $|1\rangle$, a following Pauli $\mathbf{X}$ gate is required to invert the original $|0\rangle$ to $|1\rangle$. Then another $\mathbf{U_1}(\theta_0)$ gate is applied on this new $|1\rangle$. The final Pauli $\mathbf{X}$ gate restores everything.

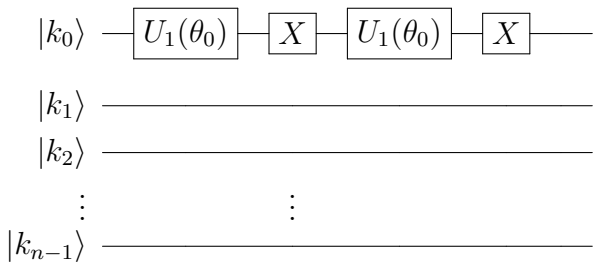

Figure 3.6: Quantum circuit of the time evolution operator with 0^{th}-order polynomial term in the exponent.

The interpretation of the 1^{st}-order intra-state coupling term (with κ parameters in Eq. 3.1) solely requires $\mathbf{U_1}$ gates. Re-writing the coordinate Q in binary expansion

$$Q = k_0 2^0 + k_1 2^1 + \cdots + k_{n-1} 2^{n-1}$$

indicates a 2^i term in the rotation angle of the $\mathbf{U_1}$ gate on the k_i qubit, as presented in Figure 3.7. These individual $\mathbf{U_1}(\theta_1 2^i)$ gates can, in principle, be applied in

parallel to encode

$$e^{-\frac{i\kappa^{(1)}Qdt}{2}}, \text{ with } \theta_1 = -\frac{\kappa^{(1)}dt}{2},$$

for the U_{S1} block (replace $\kappa^{(1)}$ by $\kappa^{(2)}$ for the U_{S2} block). However, because either the U_{S1} or U_{S2} block is controlled by the electronic state degree of freedom as a whole, these single-qubit $\mathbf{U_1}$ gates, though acting on different qubits, cannot be executed concurrently, giving an n-gate rather than a one-gate contribution to the circuit depth.

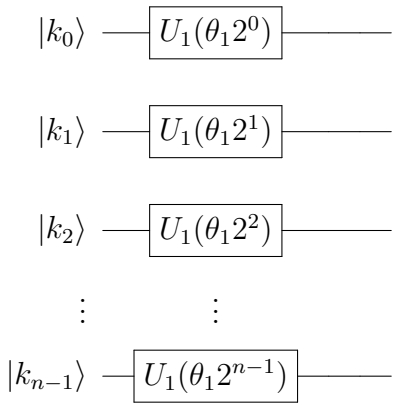

Figure 3.7: Quantum circuit of the time evolution operator with 1st-order polynomial term in the exponent.

Both the K term in momentum space and the vibrational frequency term in V_{diag} are quadratic polynomials. Taking V_{diag} as an example, we re-calculate Q^2 in binary expansion:

$$Q^2 = (\sum_{i=0}^{n-1} k_i 2^i)(\sum_{j=0}^{n-1} k_j 2^j).$$

Each component in this expression translates to regarding i as the order of the controlling qubit and j as the order of the target qubit for one $\mathbf{U_1}$ gate (or vice versa), leading to elimination of the controlling dot when $i = j$. By allocating the corresponding 2^{i+j} in the rotation angle, n^2 $\mathbf{U_1}(\theta_2 2^{i+j})$ gates in Figure 3.8 collectively apply

$$e^{-\frac{i\omega Q^2 dt}{4}}, \text{ with } \theta_2 = -\frac{\omega}{2}\frac{dt}{2},$$

to the corresponding normal mode Q. Still, all the above operations of U_{diag} or U_K permit concurrent execution across different normal modes if they were not subject to global control. Since they are now collectively controlled by either the same electronic state register or the same ancilla qubit in the Hadamard test, this enforces sequential executions and causes the circuit depth to scale with the number of normal mode registers.

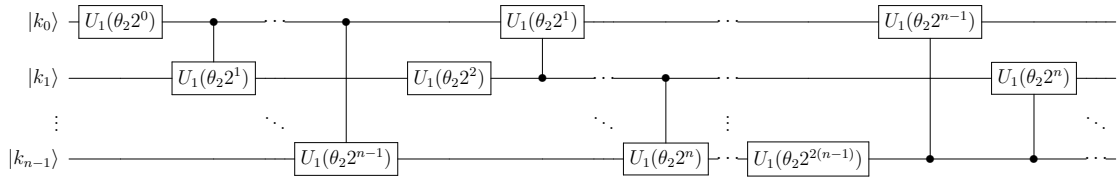

Figure 3.8: Quantum circuit of the time evolution operator with 2^{nd}-order polynomial term in the exponent.

To incorporate the linear vibronic coupling term V_{c}, successive $\mathbf{R_x}(\theta_{\text{c}} 2^i)$ gates targeting on the 1-qubit register representing the electronic state are employed to recover the U_{c} block

$$e^{-\frac{i\lambda Q_{10a} dt}{2}\mathbf{X}}, \text{ with } \theta_{\text{c}} = \lambda dt,$$

as indicated in Figure 3.9. Here the off-diagonal matrix, implemented by the Pauli $\mathbf{X}$ operation, is naturally included in the $\mathbf{R_x}$ gate as

$$\mathbf{R_x}(\theta) = e^{-i\frac{\theta}{2}\mathbf{X}}.$$

All these n $\mathbf{R_x}$ gates are controlled by the register representing Q_{10a} normal mode, with a 2^i term specified in the rotation angle of the $\mathbf{R_{x_i}}$ gate controlled by the k_i qubit of the Q_{10a} register.

When allocating n qubits to each normal mode sub-register and combing the resulting blocks, each U_{S1} or U_{S2} consist of $d(n^2 + n) + 4$ gates, with $d = 4$ corresponding to four normal modes of the 4D model Hamiltonian. Together, the two U_{S1} and U_{S2} blocks contribute $2d(n^2 + n) + 8$ gates to the entire U_{diag} section. The U_{c} and U_K blocks add a further n and dn^2, respectively. For one forward or inverse U_{QFT} block within a specific register, its gate depth is $n^2/2 + n$ and

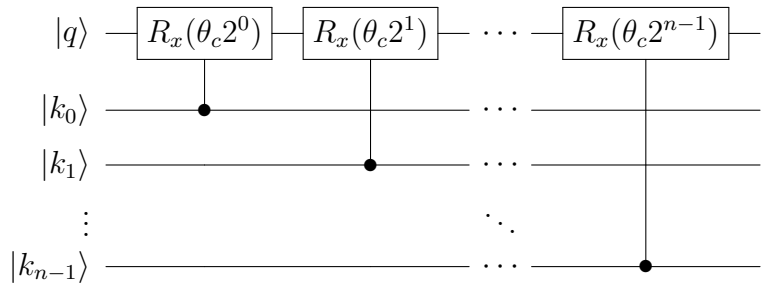

Figure 3.9: Quantum circuit of the time evolution operator with off-diagonal linear term in the exponent.

$n^2/2 + n - 1/2$ for even and odd n, respectively, according to Chapter 2. As the full time evolution is controlled by a single ancilla qubit in the Hadamard test, the number of normal modes d scales the overall depth proportionally.

Consequently, the time evolving operations of one single time step illustrated in Figure 3.5, including all the U_{diag}, U_{c}, U_K and U_{QFT} blocks, generate $6dn^2 + (6d+2)n + 16$ gates for even n (or $6dn^2 + (6d+2)n + 16 - d$ in the case of odd n). The 4D model with $n = 4$ and $d = 4$ presents a total gate count of 504 for the time propagation within one dt. The total circuit depth then depends on the number of discrete time steps n_t.

We also note that we can select an alternative second-order split with comparable accuracy by performing a half time step of the kinetic operator and a full time step of the potential operator. As the circuit for U_K is shorter than $U_{\text{diag}}U_{\text{c}}$, this reversed split saves $dn^2 + (2d+1)n + 8$ gates per time step, but requires additional QFTs at the beginning of the time evolution and at the end, before each measurement.

3.3.3 Signal Processing

Absorption Spectrum Measurement

The absorption spectrum is obtained from the Fourier Transform of the autocorrelation time function, as shown in Eq. 3.6. The autocorrelation signal will be extracted from digital quantum time propagation experiments based on single-ancilla-qubit measurements, using techniques such as the iterative phase estimation or the Hadamard test (see Section 2.3), which requires repeated measurement 'shots' sampling at multiple time steps to get an accurate signal.

This procedure is suitable when the qubit budget is limited, since it only requires a single ancilla qubit for autocorrelation extraction. With this approach, the final frequency spectrum is obtained by classical post-processing of the measured autocorrelation signal in the time domain. Advanced post-processing techniques used in related algorithms, such as statistical phase estimation, can also be used here to extract the absorption spectrum using fewer measurements [185–187].

An alternative approach to extracting the absorption spectrum, shown in Figure 3.10, is to simply apply the canonical Quantum Phase Estimation (QPE). This approach uses multiple ancilla qubits to directly sample the spectrum, bypassing the measurement of the autocorrelation signal. It generalises the single ancilla Hadamard test and replicates that across multiple ancilla qubits, each controlling time evolution to different time steps, capturing the autocorrelation signal in the time domain across the ancilla qubit register.

As shown in Figure 3.10, the time evolution in a single time step is denoted as

$$U\left|\Psi\right\rangle = e^{-iHdt}\left|\Psi\right\rangle = e^{2\pi i\theta}\left|\Psi\right\rangle.$$

Here U^{2^j} indicates repeated operations to the system:

$$U^{2^j}\left|\Psi\right\rangle = e^{2^j 2\pi i\theta}\left|\Psi\right\rangle, \text{ with } j \in [0, m).$$

The controlled U^{2^j} architecture encapsulates 2^j time steps within each block. The structure of the time register is therefore dictated by the total number of evolution steps, necessitating m qubits to represent 2^m discrete time steps within the simulation.

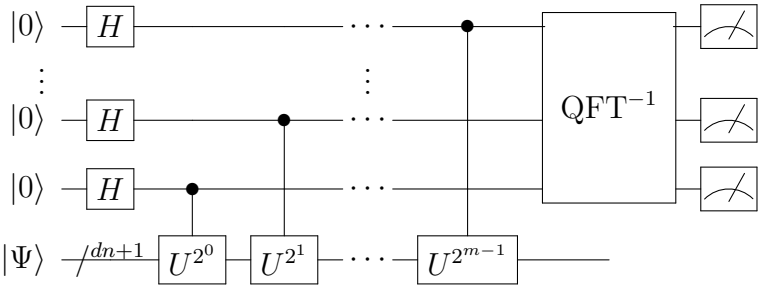

Figure 3.10: Spectrum signal measurements using canonical QPE techniques, with m qubits in the time register.

The transformation of quantum states throughout the QPE process is schematically described as follows. The Hadamard gate, in conjunction with the controlled U sequence, evolves the system

$$\text{from } |0\rangle^{\otimes m} \otimes |\Psi\rangle \text{ to } \frac{1}{2^{m/2}} \sum_{j=0}^{2^m-1} e^{2\pi i\theta j} |j\rangle \otimes |\Psi\rangle ,$$

with j constrained to $j \in [0, 2^m - 1)$ (rather than the one $j \in [0, m)$ mentioned above). Here $|j\rangle$ represents the binary encoding of index j.

After the full time evolution, the inverse QFT is applied to the time register to retrieve the phase corresponding to eigenvalues of the unitary time evolution operator. As the eigenvalues are easily deduced from the measured phases, the probability of occurrences of one specific phase is proportional to the intensity of the corresponding eigenvalue. Specifically, upon the final QFT^{-1}, measurements of the qubit states $|\theta_i\rangle$ $(i \in [0, m))$ within the time register enable recovery of the phase θ that resides in the interval $[0, 1]$. The retrieved phase appears as a binary fraction,

$$0.\theta_{m-1}\theta_{m-2}\cdots\theta_1\theta_0 = \frac{\theta_0}{2^m} + \frac{\theta_1}{2^{m-1}} + \cdots + \frac{\theta_{n-2}}{2^2} + \frac{\theta_{n-1}}{2^1},$$

from which the spectral peak positions are further determined.

The precision of θ is intrinsically linked to the number of fractional digits, with error suppression achieved by increasing the quantity of qubits encoded within the time register. Given that the quantum system exists as a superposition of multiple eigenstates, each associated with a distinct energy level, repeated executions of the circuit generate measurement outcomes that manifest as peaks centred around the corresponding eigenvalues. The statistical distribution of these peaks, governed by the inherent vibronic properties of the pyrazine system, reflects the desired characteristic spectrum. The frequency range and spectra intensity are therefore accumulated until convergence after sufficiently many repeated measurements.

Note that canonical phase estimation cannot be used to obtain the absorption spectrum directly if the damping functions $D(t)$ and $B(t)$ are required; classical post-processing of the autocorrelation signal will have to take place before computing the spectrum via Fourier transform, implying the use of techniques like single-qubit

statistical phase estimation. It is likely that neither damping function would be necessary in at-scale, fault-tolerant applications, where all modes are explicitly represented in long time propagations and multi-ancilla canonical QPE is relevant – the function $B(t)$ is needed to account for the neglected modes in low-dimensional models, and $D(t)$ to remove artefacts arising from short time propagation.

Population Dynamics Measurement

Throughout the photorelaxation process, the populations of the two states fluctuates due to the transfer through the conical intersection. The instantaneous populations are simply extracted by sampling the electronic qubit in the Z basis. The probability of measuring the $|0\rangle$ and $|1\rangle$ states reflects the population of S_1 and S_2 states:

$$P_{S1} = \frac{C_0}{C_0 + C_1} \text{ and } P_{S2} = \frac{C_1}{C_0 + C_1},$$

where C_0 and C_1 are the frequencies with which the $|0\rangle$ and $|1\rangle$ states are measured, respectively.

The population extraction described above is inherently compatible with the Hadamard-test circuit, where the electronic state at each discrete time step can be directly sampled. On the other hand, extraction of the absorption spectrum via canonical QPE necessitates coherent time evolution until the final inverse QFT, thereby precluding intermediate measurements of the electronic-state qubit. Therefore, if the time-dependent population dynamics are to be evaluated alongside the spectrum within the same circuit, the spectrum must be obtained using the Hadamard-test approach rather than canonical QPE.

3.4 Cost Evaluation

In this section, we analyse the minimum resources required to execute the SO-QFT algorithm for simulating the absorption spectrum and population dynamics of the 4D model of pyrazine. We will first characterise the number of qubits, entangling gates and repeated measurements needed to obtain expected vibronic properties, before generalising to the case of a model Hamiltonian in higher dimensions.

To quantify the resource cost of implementing the algorithm, we need to ascertain the spatial- and time-resolution necessary for obtaining accurate results with controlled simulation errors; these parameters will determine the number of qubits required to represent the state and the number of time steps required for the time-evolution. Furthermore, the resolution of the resulting spectrum is limited by the number of sampled time points in the autocorrelation signal, which need not have the same density as the SO-QFT propagated time steps. A higher sampling density means higher spectrum measurement costs in both the statistical and canonical phase estimation.

We therefore start this section with a series of numerical experiments aimed at identifying optimal simulation spatial size, spatial resolution, total simulation time and time resolution, such that the computed autocorrelation signal, population dynamics and absorption spectra closely reproduce benchmark results reported in Ref. [153, 155], which were in agreement with experimental data [188]. Given the absence of large-scale fault-tolerant quantum hardware, our numerical experiments reported here were performed via high-performance classical emulation.

3.4.1 Spatial Size and Spatial Resolution

In grid-based methods, the size of the simulation environment and the density of grid points over this space must be selected such that the wavefunction is accurately represented throughout the simulated time window without using an excessively dense grid. We also need to make sure that the simulation environment is large enough to model the physics without introducing any significant artificial reflections at the boundaries.

In Tables 3.2 and 3.3, we report the Zero Point Energy (ZPE) of the initial state as a function of the spatial range and grid density in dimensionless normal coordinates; the energies were calculated as

$$\langle E \rangle = \langle \Psi_0 | \, V \, | \Psi_0 \rangle + \langle \Psi_0 | \, K \, | \Psi_0 \rangle \, , \tag{3.13}$$

with each term evaluated in real and momentum space respectively. We conducted two sets of systematic convergence tests: first, by fixing the spatial resolution and

N	Range	ZPE/eV
8	$[-2.5 : 2.5]$	0.2254839449
16	$[-5 : 5]$	0.2258500005
32	$[-10 : 10]$	0.2258500001
64	$[-20 : 20]$	0.2258500001

Table 3.2: ZPE of the initial state Ψ_0 expressed using N grid points over dimensionless normal coordinates that span $[Q_{\min} : Q_{\max}]$.

N	Spacing	ZPE/eV
4	3.33	0.6524371769
8	1.43	0.2340338987
16	0.67	0.2258500005
32	0.32	0.2258500000
64	0.16	0.2258500000

Table 3.3: ZPE of Ψ_0 using N grid points between $[-5, 5]$ in dimensionless normal mode coordinates.

varying the spatial range (Table 3.2) to determine the smallest domain ensuring energy convergence, and second, by fixing this optimal size and adjusting the spatial resolution (Table 3.3) to identify the minimal number of grid points that retains accuracy. After testing a range of spatial parameters, we found that the computed ZPE is fully converged to within 0.5 neV of the exact value when 16 grid points are used to express each dimensionless normal mode, where each mode has a range of $Q = [-5, 5]$.

In addition, we validate that the size of the simulation environment is large enough to capture the essential time-dependent physics. Taking the simulation coordinates of $Q = [-5, 5]$ and 16 grid points for each coordinate, we performed a time evolution of the system using 2,048 time steps within a total time of around 264 fs. Figure 3.11 shows the maximum values of the probability density at the extreme ends of the simulation range during that simulated time, evaluated as:

$$P_i(t) = \max \langle \Psi_t | \, \delta(Q_i \pm 5) \, | \Psi_t \rangle \, . \tag{3.14}$$

We see that the probability amplitudes of the wavefunction at edges of the simulation

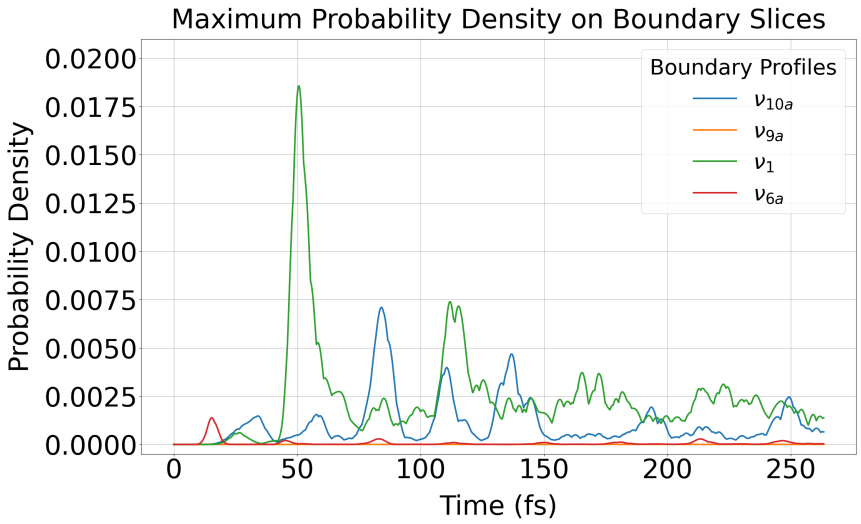

Figure 3.11: Maximum values of the probability density at the boundaries of the simulation box for each normal mode as a function of time. The persistently low amplitudes indicate that the chosen simulation size is sufficient to contain the evolving wavefunction.

range remain persistently low throughout the time evolution, confirming that the size of the simulation environment is sufficient.

Nevertheless, these amplitudes do not vanish entirely. Residual boundary interactions may introduce weak artificial reflections at longer propagation times and affect the long-time behaviour of the autocorrelation function. In the frequency domain, such late-time distortions lead to subtle intensity variations in the spectrum, while the dominant spectral structure remains stable. In future work, these boundary effects could be systematically suppressed by enlarging the spatial domain and employing a denser grid.

3.4.2 Total Time and Time Resolution

To obtain an accurate absorption spectrum, the dynamics must be simulated for a sufficiently long time to record the features of the vibronic dynamics. Furthermore, the granularity of the SO-QFT decomposition (time resolution) must be sufficiently small to control the Trotter error. Finally, the autocorrelation sampling must also be frequent enough to resolve the relevant features of the spectrum. The overall quantum resource, gate depth and measurement requirements will depend on these algorithmic parameters.

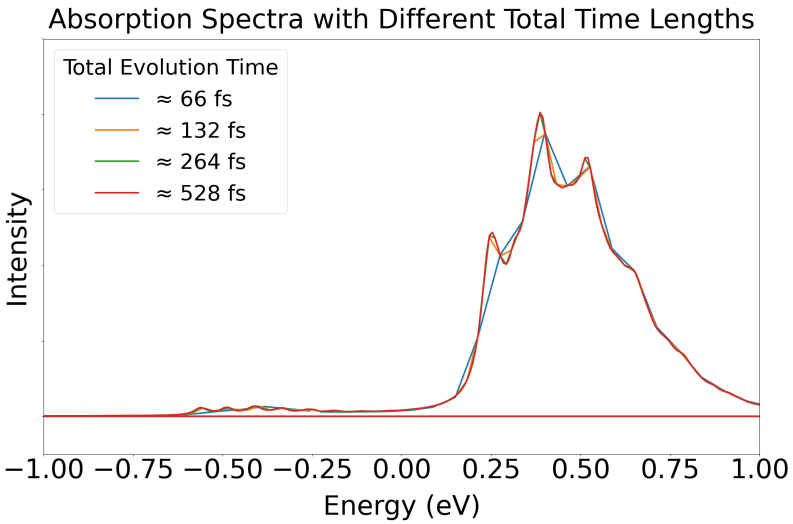

Figure 3.12: Comparison of absorption spectra across various time propagation lengths, with the number of time steps set to 512, 1,024, 2,048 and 4,096 for total time lengths of 66, 132, 264, 528 fs, respectively. This setup ensures a time resolution of $dt = 0.13$ fs in all cases.

We first performed simulations to determine the necessary total simulation time for capturing the correct dynamics by simulating increasing periods of total evolution time T but with the same time resolution $dt = 0.13$ fs. The autocorrelation function was recorded at every time step. Figure 3.12 shows the resulting absorption spectra. We see that a total simulated time of 264 fs suffices to produce an accurate absorption spectrum. For simulations of this length, we found the inclusion of the damping function $D(t)$ has negligible impact on the resulting spectrum; we therefore omit its use for the remainder of this work.

We then explored, using a total simulation time of $T \approx 264$ fs, how the time step affects the time propagation errors. Figure 3.13 reports the autocorrelation function, absorption spectra, and population dynamics resulting from simulations that used between 128-2,048 time steps. The autocorrelation function was again sampled at the same frequency as the time resolution dt. The minimum number of time steps that yields a qualitative spectrum and population dynamics is 512 (corresponding to a time resolution of $dt = 0.52$ fs). Further increasing the number of time steps to 1,024 (i.e., $dt = 0.26$ fs) ensures a converged quantitative reproduction of the vibronic dynamics.

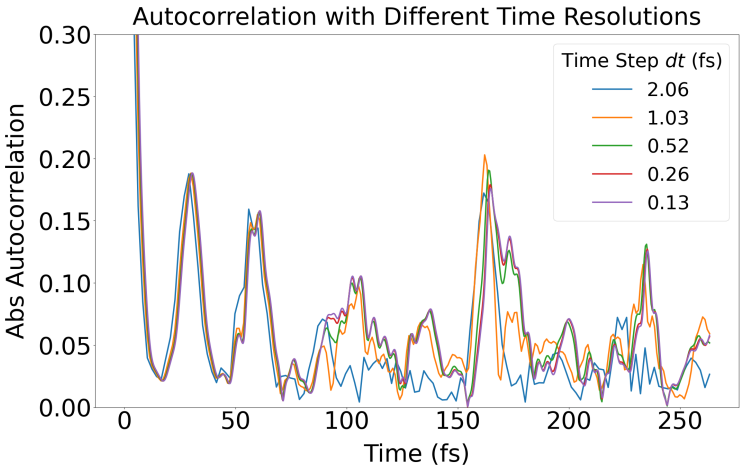

(a)

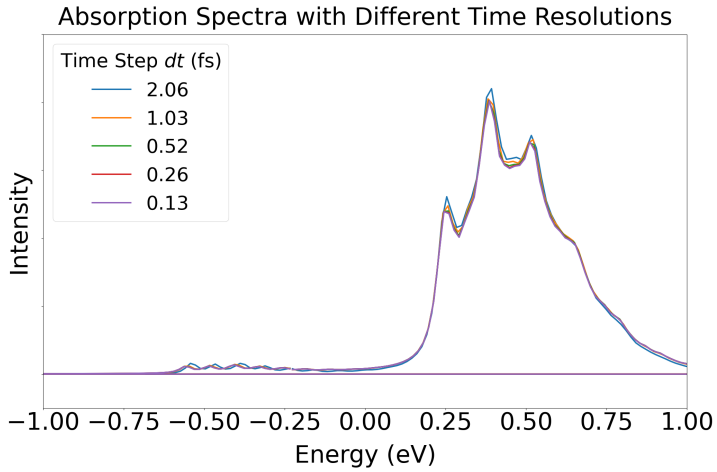

(b)

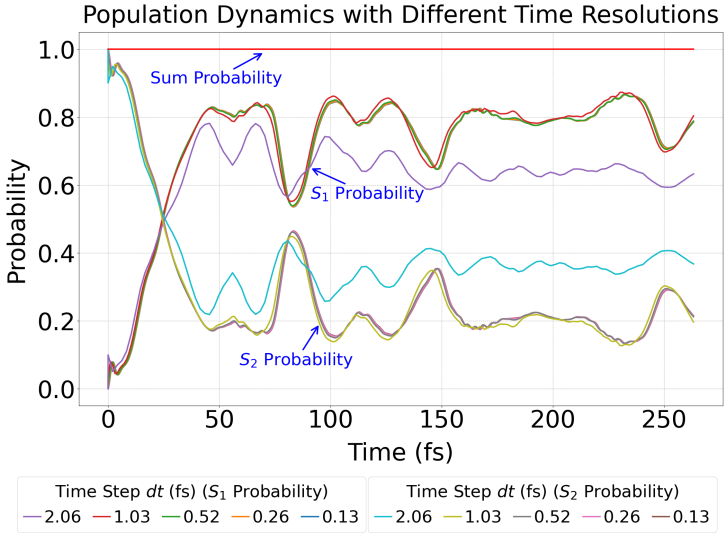

(c)

Figure 3.13: Comparison of (a) absolute autocorrelation, (b) absorption spectra, and (c) population dynamics with 128, 256, 512, 1,024 and 2,048 time steps used within a fixed total evolution time of around 264 fs.

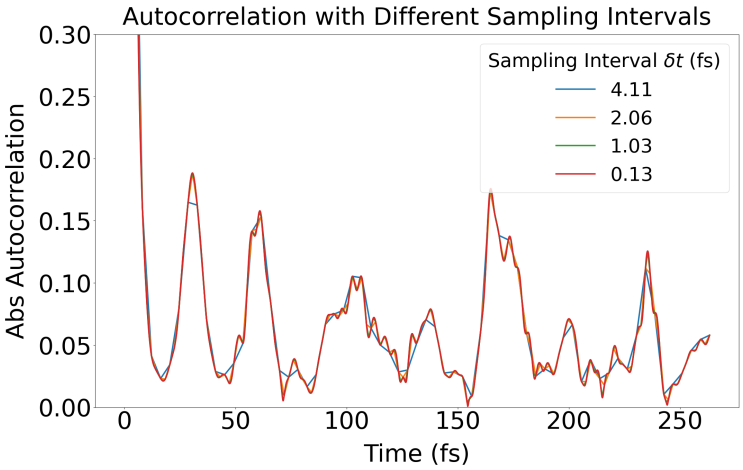

(a)

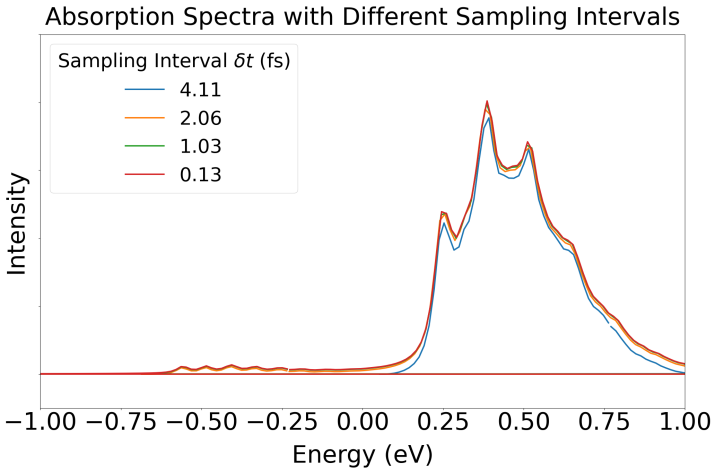

(b)

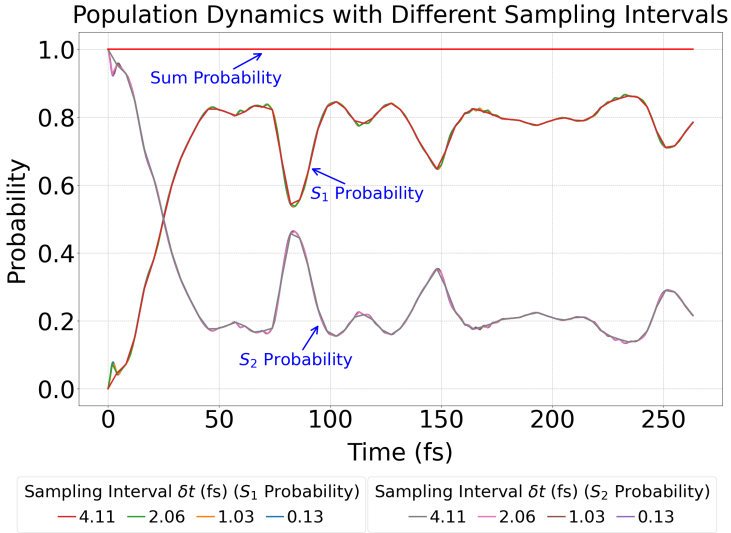

(c)

Figure 3.14: Comparison of (a) absolute autocorrelation, (b) Absorption spectra, and (c) population dynamics with different sampling time intervals, while keeping the time evolution setting fixed at 2,048 steps within 264 fs.

As discussed, it is not necessary to sample the autocorrelation signal at every time step in the Trotter evolution. To investigate this, we computed autocorrelation signals obtained from simulating $T \approx 264$ fs with a Trotter step of 0.13 fs, but sampled at longer intervals: every 32, 16 and 8 time steps. The resulting autocorrelation functions and corresponding absorption spectra are compared in Figure 3.14, where we visualise the severity of under-sampling with a smooth interpolation between the recorded data points. Similarly, the coherence of population dynamics curvatures across S_1 and S_2 states is also presented to assess the reliability and fidelity of the chosen sampling strategy. To obtain an accurate spectral function, it is only necessary to sample the autocorrelation function through quantum circuit measurements at a frequency of once every 2.06 fs, which can significantly reduce the measurement overhead.

We also digitised the published four-mode MCTDH results of Ref. [155] and re-plotted them in Figure 3.15 for comparison. Over the shared time window of 0–120 fs, the SO-QFT curves presented in this section reproduce the principal features of these benchmarks across all reported observables.

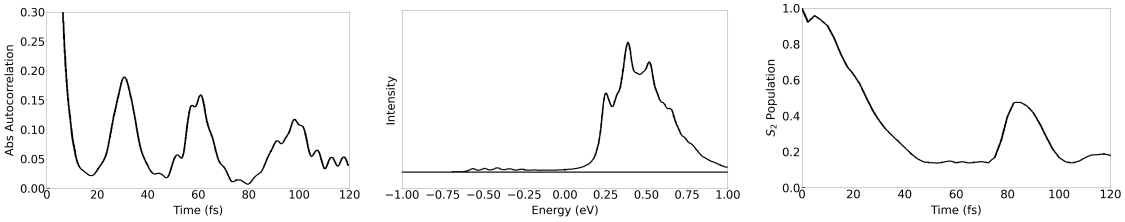

(a) Autocorrelation function **(b)** Absorption spectrum **(c)** Population dynamics

Figure 3.15: MCTDH benchmark results (Ref. [155]) for (a) autocorrelation function, (b) absorption spectrum, and (c) population dynamics. These curves are digitised from the published figures and serve as reference for comparison with the present calculations.

3.4.3 Gate Depth Calculation

We now present a quantitative estimate of the gate depth required for a simulation using the spatial and time resolutions established in the preceding sections. Many of the operations act on each of the registers representing the normal modes separately, and we are concerned with the number of gates that must be performed in sequence.

From Section 3.3.1 we concluded that the initial state preparation using uniformly controlled rotations has a gate depth of $2^{n+1} - 3$, where n is the number of qubits in each normal mode register. Section 3.3.2 concludes that the time evolution adds $6dn^2 + (6d + 2)n + 16$ gates per time step. As mentioned in Section 3.3.3, an additional ancillary qubit is necessary to accomplish Hadamard tests when extracting the autocorrelation signal statistically. The initial Hadamard gate can be performed in parallel to the state preparation, but the Hadamard gate at the end of the test contributes one additional gate. The **S** gate required to measure the imaginary part of the signal contributes one further gate.

We now consider the gate depth for performing time evolution to obtain the autocorrelation signal and population dynamics. Recall that we must first propagate the initial state to a particular point in 'simulated' time, then measure the Hadamard test ancillary qubit for deriving the autocorrelation signal, or the qubit representing the electronic states to get the population dynamics. To obtain the next time point, the workflow must be restarted from the very beginning. The circuit contributing the greatest depth is therefore that for extracting the imaginary part of the autocorrelation at the last time point. Note that the population measurement requires two fewer gates, as it does not involve ancilla manipulation.

	Gate depth	$n = 4$, $n_t = 512$	$n = 5$, $n_t = 1{,}024$
State Preparation	$N_\mathrm{i} = 2^{n+1} - 3$	29	61
Time Evolution	$N_\mathrm{t} = (6dn^2 + (6d + 2)n + 16)(n_t - 1)$ for even n $N_\mathrm{t} = (6dn^2 + (6d + 2)n + 16 - d)(n_t - 1)$ for odd n	257,544	759,066
Signal processing	$N_\mathrm{m} = (\log_2 n_t)^2/2 + \log_2 n_t$ for even $\log_2 n_t$ $N_\mathrm{m} = (\log_2 n_t)^2/2 + \log_2 n_t - 1/2$ for odd $\log_2 n_t$	49	60
Full algorithm A	$N_\mathrm{i} + N_\mathrm{t} + 2$	257,575	759,129
Full algorithm B	$N_\mathrm{i} + N_\mathrm{t} + N_\mathrm{m}$	257,622	759,187

Table 3.4: Cost evaluation through gate depth for 4D simulations ($d = 4$) of pyrazine photodynamics in terms of the number of qubits per mode n and the number of time steps n_t. Algorithm A is the classical post-processing approach where the autocorrelation function is obtained through measurement, and B is the fully quantum approach which directly obtains spectral signals through QPE.

In Table 3.4, we present the full cost in terms of quantum gate depth. n represents the number of qubits per vibrational mode and n_t represents the number

of time steps evolved within 264 fs. The circuit associated with preparing the initial $t = 0$ as an individual time point always contributes. To illustrate the estimation concretely, we provide representative costs in two regimes: a simulation with $n = 4$ and $n_t = 512$, and a more expensive simulation with $n = 5$ and $n_t = 1{,}024$. The deepest circuits involve 257,575 and 759,129 gates, respectively.

In the case where no explicit broadening or damping functions for post-processing the autocorrelation function is necessary, a fully quantum canonical QPE approach provides one of the most direct ways to derive the spectrum. This approach requires an auxiliary register of m qubits instead of just one, where the number of time points sampled is 2^m. The initial Hadamard gates applied to qubits on this time register are applied in parallel with the initial state preparation on the state registers encoding the normal modes. However, much like the single-ancilla, statistical version of phase estimation, the final inverse QFT on the ancilla register adds another $m^2/2 + m$ gate counts after the time evolution. Table 3.4 summarises the generalised formula calculating the circuit depth required for the canonical QPE approach. For the exploratory run with $n = 4$ and $n_t = 512$, the deepest circuits involve 257,622 gates and for the production run with $n = 5$ and $n_t = 1{,}024$ the gate depth becomes 759,187.

3.4.4 Measurement Shot Estimation

We now give an assessment of the minimum number of measurement shots necessary to reproduce the absorption spectrum, relevant to both the statistical autocorrelation-based and direct spectrum sampling scenarios, using a total simulation time of $T \approx 264$ fs, a time step of $dt = 0.26$ fs and autocorrelation sampling of $\delta t = 0.26$ fs. Our target is for the empirical spectrum to achieve a Total Variation Distance (TVD) below a specified threshold. Here the TVD is defined as a unitless relative error measure:

$$\frac{1}{2}\sum_i \left| \frac{I(\omega_i)^{\text{empirical}}}{\sum_j I(\omega_j)^{\text{empirical}}} - \frac{I(\omega_i)^{\text{target}}}{\sum_j I(\omega_j)^{\text{target}}} \right|. \tag{3.15}$$

Our first investigation separately sampled real and imaginary parts of the autocorrelation function $A(t)$, as would be done on a real quantum hardware. We classically mimicked this process by drawing binary outcomes from the target binomial distributions:

$$\begin{aligned}
&\text{sampling of the real part follows} \\
&P(|0\rangle) = \frac{1 + \mathbb{R}\mathrm{e}\{A(t)\}}{2},\ P(|1\rangle) = 1 - P(|0\rangle); \\
&\text{sampling of the imaginary part follows} \\
&P(|1\rangle) = \frac{1 + \mathbb{I}\mathrm{m}\{A(t)\}}{2},\ P(|0\rangle) = 1 - P(|1\rangle).
\end{aligned} \tag{3.16}$$

For each discrete time point, sampling counts ranged from 1,000 to 300,000, with increments of 1,000. After combining real and imaginary parts, we performed the Fourier Transform to obtain the estimated spectrum and evaluated its fidelity via TVD against the target spectrum.

In the second assessment of the full QPE approach, we treated the target spectrum as a normalised probability distribution and drew samples directly from it using a discrete random variable model. At each iteration, we simulated M measurements and the empirical spectrum was constructed and compared to the target spectrum via TVD, with M increasing from 1,000 to 200,000 in steps of 1,000.

For both methods, we track the evolution of TVD as a function of measurement counts in Figure 3.16a and 3.16b, report the measurement counts required to achieve TVD thresholds of 4%, 3%, 2%, and 1% in Table 3.5, and visualise the recovered spectra at selected measurement counts in Figure 3.16c and 3.16d.

The differing ranges of the horizontal axes in Figures 3.16a and 3.16b reveal the variations in sampling efficiencies: the direct spectrum sampling exhibits a steeper decline in TVD with increasing samples, compared to the autocorrelation-based sampling. In other words, reaching high accuracy levels requires fewer measurements for the full QPE approach.

As illustrated in Figure 3.16c and 3.16d, both methods demonstrate systematic improvement of the reconstructed spectrum as the sample size grows. Table 3.5 lists the measurement counts at which each TVD threshold is first met and then sustained

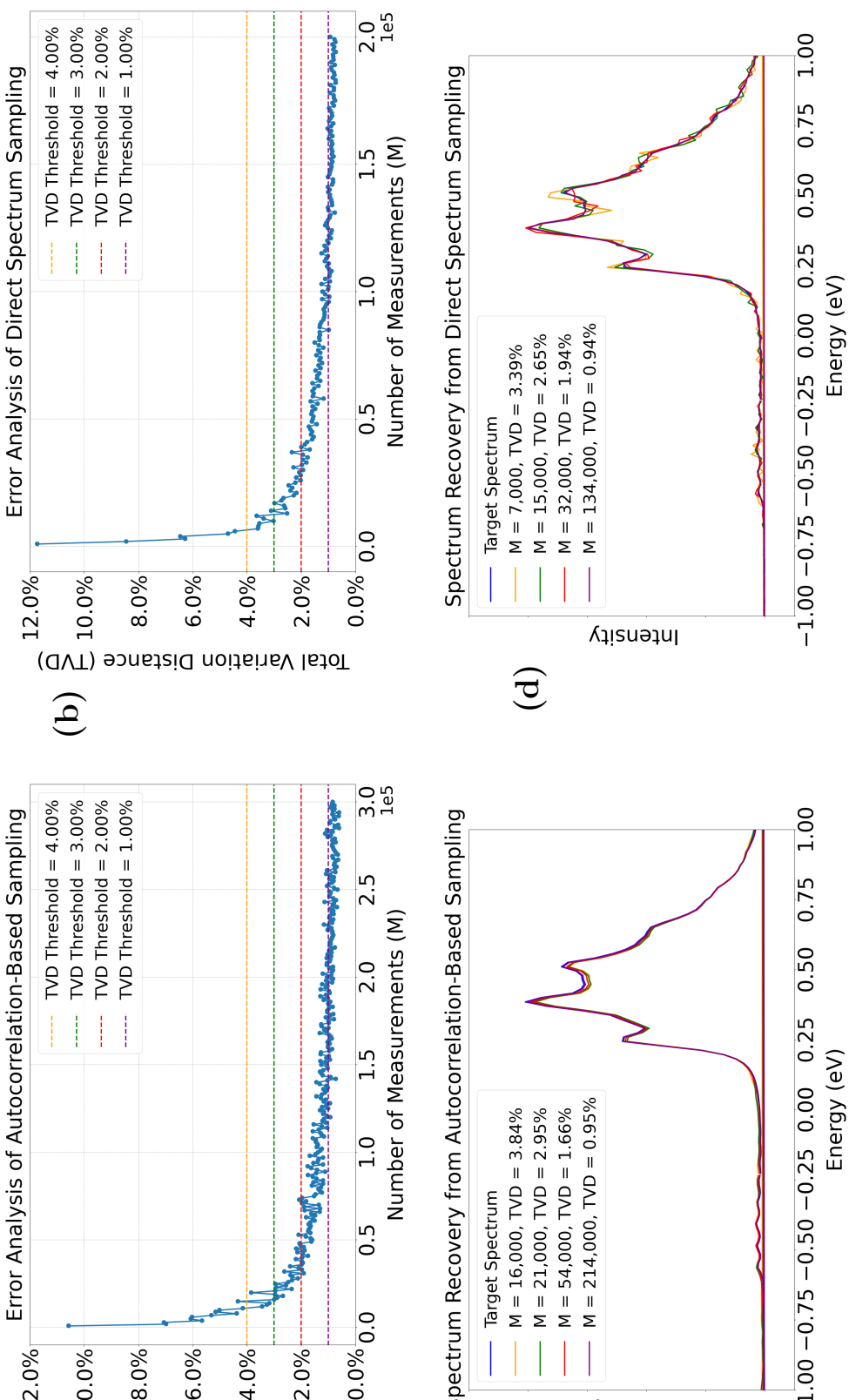

Figure 3.16: Estimating measurement requirements for two different sampling strategies: left panels depict results from autocorrelation-based sampling, while the right panels correspond to direct spectrum sampling. Panels (a) and (b) plot the TVD between the simulated and target spectra as a function of the number of measurements. Panels (c) and (d) show the recovered spectra under four selected TVD thresholds (4%, 3%, 2%, and 1%). These results serve to calibrate the measurement cost required for each approach to reach practical TVD thresholds.

Autocorrelation Sampling		Direct Spectrum Sampling	
M	TVD	M	TVD
16,000	3.84%	7,000	3.39%
22,000	2.95%	15,000	2.65%
54,000	1.66%	32,000	1.94%
214,000	0.95%	134,000	0.94%

Table 3.5: Measurement counts M required for achieving TVD thresholds of 4%, 3%, 2% and 1% using autocorrelation-based sampling or direct spectrum sampling schemes.

across five consecutive evaluations. This criterion ensures robust convergence, reducing the likelihood of reaching the threshold by chance fluctuation. Notably, a measurement count of 134,000 is sufficient to bring the TVD below 1.00% in the direct spectrum sampling case, whereas the autocorrelation-based method demands 214,000 shots at each time point to reach the same threshold.

3.5 Extension To Higher Dimensions

Quantum algorithms are attractive because the exponential growth in the computational space provided by linear addition of qubits makes it possible to embed the many coupled degrees of freedom in a molecule as a large state vector on a quantum computer. We now extend our cost evaluation to the full 24D treatment of pyrazine, quantifying both the qubit requirements and the circuit depth estimates.

The simplest 24D model treats the remaining 20 modes as an external bath represented by displaced harmonic oscillators [154, 156, 159, 160]. Since the Hamiltonian has the same functional structure as the 4D treatment in Eq. 3.1, the depth of the circuit incorporating bath-mode operations can be evaluated by substituting $d = 24$ into the scaling relations in Section 3.3.2. Extra costs also stem from the additional number of qubits necessary for building expanded normal mode register, which increases the qubit requirement to 97 when 4 qubits are used for each vibrational mode.

A more complete 24D model Hamiltonian of pyrazine includes all terms up to second order:

$$H = \begin{pmatrix} K + V_{\text{diag}}^{S1} & 0 \\ 0 & K + V_{\text{diag}}^{S2} \end{pmatrix} + \begin{pmatrix} 0 & V_{\text{off}} \\ V_{\text{off}} & 0 \end{pmatrix} \tag{3.17}$$

where

$$K = -\sum_k \frac{\omega_k}{2} \frac{\partial^2}{\partial Q_k^2} \tag{3.18}$$

$$\begin{aligned} V_{\text{diag}}^{S1} &= \Delta + \sum_{j \in G_1} \kappa_j^{(1)} Q_j + \frac{1}{2} \sum_k \omega_k Q_k^2 + \sum_{(l,m) \in G_2} \gamma_{l,m}^{(1)} Q_l Q_m \\ V_{\text{diag}}^{S2} &= -\Delta + \sum_{j \in G_1} \kappa_j^{(2)} Q_j + \frac{1}{2} \sum_k \omega_k Q_k^2 + \sum_{(l,m) \in G_2} \gamma_{l,m}^{(2)} Q_l Q_m \\ V_{\text{off}} &= \sum_{j \in G_3} \lambda_j Q_j + \sum_{(l,m) \in G_4} \mu_{l,m} Q_l Q_m. \end{aligned} \tag{3.19}$$

In this expression, k spans 24 normal modes, all of which are represented as displaced harmonic oscillators. The linear on-diagonal expansion terms involve modes in the G_1 set characterised by A_g symmetry, and pairs of modes with identical symmetry, collectively labeled as G_2 set. Meanwhile, off-diagonal components capture interactions from the set of $G_3 = \nu_{10a}$ with B_{1g} symmetry and the G_4 set containing all pairs of modes whose product exhibit B_{1g} symmetry, i.e., pairs formed by combinations of $A_g \times B_{1g}$, $B_{2g} \times B_{3g}$, $A_u \times B_{1u}$ and $B_{2u} \times B_{3u}$ [156]. The number of modes within each symmetry class is listed in Table 3.6. From these counts, and applying the corresponding symmetry-combination rules, we obtain the number of terms in each set to be $d_{G_1} = 5$, $d_{G_2} = 31$, $d_{G_3} = 1$, and $d_{G_4} = 29$.

Symmetry	A_g	B_{1g}	B_{2g}	B_{3g}	A_u	B_{1u}	B_{2u}	B_{3u}
Number of Modes	5	1	2	4	2	4	4	2

Table 3.6: Number of modes in different symmetry groups.

To estimate the quantum gate depth we adopt the same range of time and spatial discretisation parameters determined from our 4D model of pyrazine. While this extrapolation does not account for dimension-dependent increases in Trotter error due to the growing number of Hamiltonian terms, we note that discretisation

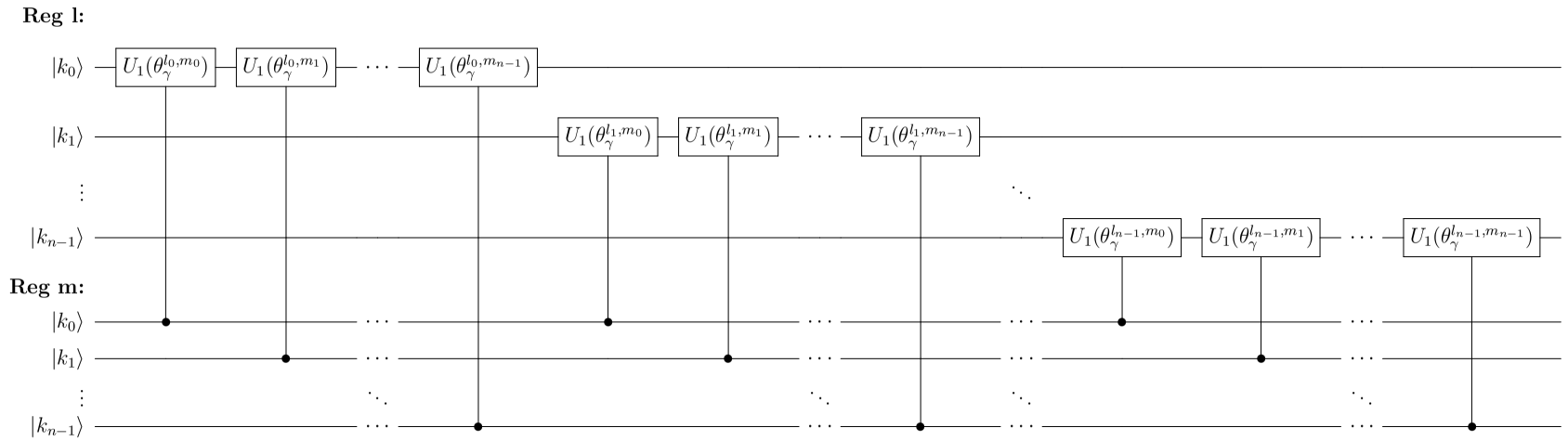

Figure 3.17: Quantum circuit for $e^{-i\gamma_{l,m}Q_lQ_mdt}$, the time evolution operators of on-diagonal bilinear terms.

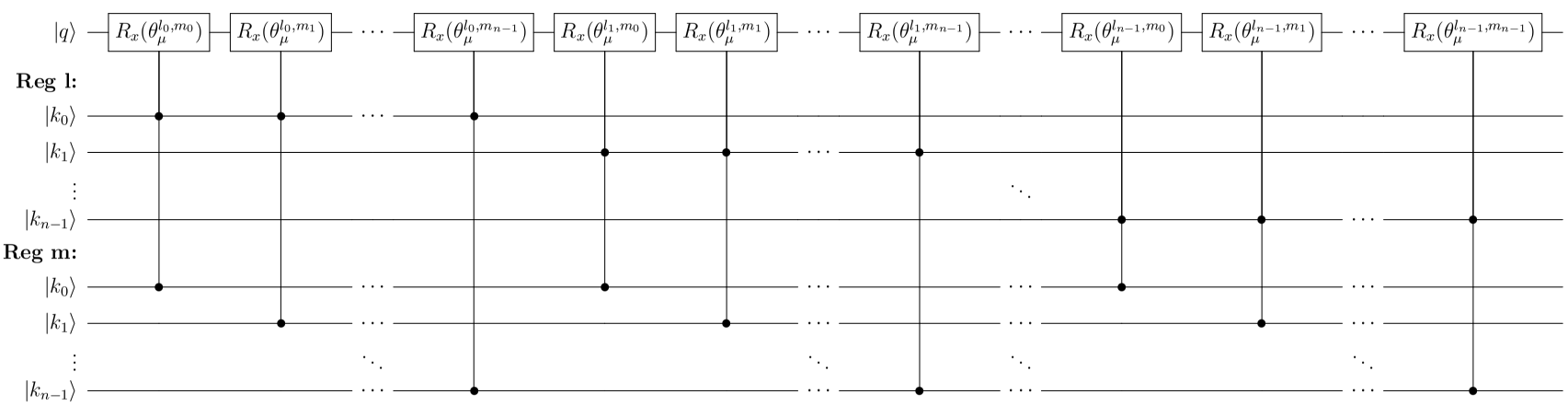

Figure 3.18: Quantum circuit for $e^{-i\mu_{l,m}Q_lQ_mdt}$, the time evolution operators of off-diagonal bilinear terms.

schemes with similar parameters have been successfully employed in classical full-dimensional simulations of 24D pyrazine using SOFT-based approaches with either adaptive coherent-state expansions (Matching Pursuit-SOFT) [161] or tensor-train compression techniques (Tensor Train-SOFT) [189]. Assuming that the time resolution demands do not vary significantly with dimensionality allows us to derive more generalised resource projections of the quantum implementation.

In adapting the quantum circuits to the 24D model Hamiltonian, we observe that the kinetic terms as well as the constant, linear and quadratic potential terms mirror those used in the 4D simulation. However, new circuits are required to implement the polynomials for the bilinear on-diagonal elements associated with the G_2 set and the bilinear off-diagonal elements stemming from the G_4 set. The quantum circuits to handle these terms are depicted in Figure 3.17 and Figure 3.18. The phase angles of $\mathbf{U_1}$ gates in Figure 3.17 are defined as

$$\theta_{\gamma}^{l_i,m_j} = -\gamma_{l,m} dt 2^{l_i} 2^{m_j},$$

where l_i and m_j denote the respective positions of the target qubit in register of normal mode l and the controlling qubit in register of normal mode m. The $\mathbf{R_x}$ gates in Figure 3.18 have phase angles specified by

$$\theta_{\mu}^{l_i,m_j} = \mu_{l,m} dt 2^{l_i} 2^{m_i},$$

with l_i and m_j indicating the controlling qubit positions in their respective l and m normal mode registers. As detailed in these figures, each bilinear on-diagonal term maps to n^2 two-qubit gates, and each off-diagonal term necessitates n^2 controlled-controlled-rotation gates.

To remain consistent with gate depth analyses of the 4D model, each three-qubit gate needs to be further translated into a sequence of two-qubit operations. Following the decomposition scheme outlined in [54], one $\mathbf{C^2R_x}$ gate can be implemented using 5 two-qubit gates. Accordingly, each term in the G_4 set contributes $5n^2$ gates to the total circuit depth. Summing over all terms in the 24D model Hamiltonian,

	Gate depth	$n = 4$, $n_t = 512$	$n = 5$, $n_t = 1{,}024$
State Preparation	$N_\mathrm{i} = 2^{n+1} - 3$	29	61
Register Preparation	$N_\mathrm{p} = n^2/2 + n$ for even n $N_\mathrm{p} = n^2/2 + n - 1/2$ for odd n	12	17
Time Evolution	$N_\mathrm{t} = 2N_\mathrm{p} + ((5d + 5d_{G_4} + 2d_{G_2})n^2 + (2d + 2d_{G_1} + d_{G_3})n + 8)(n_t - 1)$ for even n $N_\mathrm{t} = 2N_\mathrm{p} + ((5d + 5d_{G_4} + 2d_{G_2})n^2 + (2d + 2d_{G_1} + d_{G_3})n + 8 - d)(n_t - 1)$ for odd n	2,798,260	8,648,476
Signal processing	$N_\mathrm{m} = (\log_2 n_t)^2/2 + \log_2 n_t$ for even $\log_2 n_t$ $N_\mathrm{m} = (\log_2 n_t)^2/2 + \log_2 n_t - 1/2$ for odd $\log_2 n_t$	49	60
Full algorithm A	$N_\mathrm{i} + N_\mathrm{t} + 2$	2,798,291	8,648,539
Full algorithm B	$N_\mathrm{i} + N_\mathrm{t} + N_\mathrm{m}$	2,798,338	8,648,597

Table 3.7: Cost evaluation through gate depth for 24D ($d = 24$) simulations of pyrazine photodynamics in terms of the number of qubits per mode n and the number of time steps n_t. Algorithm A is the classical post-processing approach where the autocorrelation function is obtained through measurement, and B is the fully quantum approach which directly obtains spectral signals through QPE.

the U_{S1} and U_{S2} blocks together contributes $2((d + d_{G_2})n^2 + d_{G_1}n + 4)$ gates, while the U_c block adds $5d_{G_4}n^2 + d_{G_3}n$.

In the 24D simulation, the time evolution operators for the potential term in the Hamiltonian is notably more computationally demanding than the kinetic part. A more efficient operator-splitting scheme thus begins with a half time step of kinetic operators, followed by a full time step of potential operators, and concludes with another half time step of kinetic operators, represented as:

$$e^{-iHdt} \approx e^{-\frac{iKdt}{2}} U_{\mathrm{QFT}} e^{-iVdt} U_{\mathrm{QFT}}^{-1} e^{-\frac{iKdt}{2}}, \tag{3.20}$$

instead of the previous Eq. 3.12. For the 4D simulations we were able to verify that this reordering has an insignificant impact on the accuracy of the results. The gate count per time step thus includes contributions from two kinetic propagation operators, one potential propagation operator, and two QFT subroutines, giving $(5d + 5d_{G_4} + 2d_{G_2})n^2 + (2d + 2d_{G_1} + d_{G_3})n + 8$ gates. In addition to this, another two QFT processes are required at the initial and final time points to prepare the registers in the appropriate position or momentum spaces. In Table 3.7, we report the full gate depth evaluation associated with full 24D simulations.

For runs where $n = 4$ qubits are used for each normal mode register and employing $n_t = 512$ time steps, they result in circuit depths of around 2.8×10^6 for both statistical and canonical phase estimation approaches. For production runs with $n = 5$ and $n_t = 1{,}024$, this increases to 8.6×10^6.

More generally, the present framework assumes access to pre-constructed vibronic Hamiltonians when considering extensions to larger dimensionality. For more complex systems, however, the classical preprocessing required to generate such models, including electronic-structure calculations, diabatization, and extraction of coupling parameters, may itself become computationally intensive and constitute a practical bottleneck depending on molecular complexity and the level of electronic-structure theory employed. These upstream costs are intrinsic to Hamiltonian construction and arise independently of the subsequent propagation algorithm.

3.6 Conclusions

Classical simulation methods for investigating the photodynamics of molecular systems with more than a handful of degrees of freedom rely on sophisticated numerical techniques to approximate the exponential complexity of coherent quantum dynamics using a polynomial number of parameters, and quickly become limited in the size of system that can be treated reliably. Quantum simulation methods are not limited in this way. In particular, through the grid-based SO-QFT approach the exponentially large quantum state can be stored using a linear number of qubits and the state can be time-evolved according to the Hamiltonian with a polynomial number of quantum gates. The SO-QFT approach to molecular photodynamics is thus a plausible candidate for examining the prospects of quantum advantage in scientific computing.

This work presents and assesses an end-to-end SO-QFT quantum algorithm for simulating the vibronic dynamics of photoexcited pyrazine, encompassing initial state preparation, time evolution and signal processing through measurement. Through a full resource assay, using realistic algorithmic parameters for the temporal and spatial resolutions required to obtain scientifically meaningful results, we have determined the qubit budget and gate depth that would be required for this approach once fault tolerant devices of sufficient scale become available. We chose pyrazine as a case study since it has been studied extensively and is well understood, but the algorithm extends naturally to general treatments of the photodynamics through conical intersections of more complicated molecular systems [190]. We find that the time and space resolutions and extents required in practice for the quantum algorithm are commensurate with those used for the classical analogues.

The number of qubits required scales linearly with the number of degrees of freedom and logarithmically with the number of time steps: $dn + 1 + \log_2 n_t$. The depth of the deepest quantum circuit required for the calculation scales only quadratically with the size of the maximum qubit register used to encode an individual normal mode, linearly with the number of normal modes, and linearly with the number of Trotter steps in the time evolution, i.e., asymptotically $\mathcal{O}(dn^2 n_t)$

plus overhead. For a 24D simulation of pyrazine using a vibronic Hamiltonian complete to second order, exploratory calculations can be performed using 4 qubit normal mode registers, corresponding to 16 grid points, and 512 time steps spanning the 264 fs dynamics. This requires 106 qubits and 2.8×10^6 sequential gates. Production calculations with 5 qubit normal modes registers and 1,024 time steps requires 131 qubits and 8.6×10^6 sequential gates. We find that the number of measurements required to obtain an accurate spectrum is around 2×10^5.

The two measurement strategies for the absorption spectrum exhibit comparable circuit-depth scaling in propagation cost. While multiple-ancilla QPE reduces measurement repetitions, its functionality is restricted to spectral estimation. The single-ancilla Hadamard test allows the simultaneous extraction of additional time-dependent observables such as population dynamics, albeit at the cost of repeated sampling across discrete time steps. As quantum hardware continues to mature, these trade-offs between qubit budget, measurement overhead, and target observables are expected to determine which approach becomes preferable in practice.

The framework and cost analyses developed in this work provide a solid foundation for quantum algorithms aimed at simulating vibronic dynamics of complex molecular systems. Although the 24D pyrazine example is tractable using the best-in-class classical algorithms for simulating quantum dynamics, the addition of just a few more atoms increases the dimensionality to above 30, which is currently out of reach. Our cost estimates therefore provide lower bound on the resource required for achieving quantum advantage through this approach and a target for hardware development.

From a hardware perspective, the resource estimates reported here place vibronic simulations of pyrazine well beyond the reach of current NISQ devices, primarily due to the stringent logical error rates required to preserve phase coherence over deep sequential circuits. As such, the present algorithmic framework should be regarded as a target for early fault-tolerant quantum processors rather than near-term hardware. Future analysis incorporating error-correction overhead, gate-set compilation, and

architecture-level constraints will be essential before such high-dimensional vibronic simulations become experimentally feasible.

4

Infrared Spectra of Vibrational Systems

Contents

4.1 Introduction

The simulation of Infrared Spectra has long been a significant topic in molecular characterisation, as it is crucial for interpreting molecular structures and predicting vibrational behaviours. It proceeds by first constructing Potential Energy Surface (PES) and Dipole Moment Surface (DMS) from electronic-structure calculations and then solving nuclear-vibrational dynamics on these surfaces. The former typically relies on Density Functional Theory [191–193] or Post-Hartree-Fock methods [194–197], optionally followed by quartic force-field expansions. Established nuclear-vibrational treatments for infrared spectroscopy can be broadly classified into time-independent and time-dependent approaches. Time-independent methods construct an anharmonic vibrational Hamiltonian and solve for its eigenvalues and eigenstates, from which band positions and intensities are obtained via energy differences and transition dipole matrix elements, respectively. Within this regime, vibrational perturbation theory (VPT2 and higher-order variants) [198–200] treats anharmonicity as corrections to harmonic reference states through low-order perturbative expansions, offering favourable computational efficiency but potentially reduced accuracy in the presence of strong anharmonicity or resonances. Variational vibrational calculations [201–204] explicitly diagonalize the anharmonic Hamiltonian in a truncated basis, providing systematically improvable accuracy, albeit with rapidly increasing cost as the vibrational basis expands with mode number.

Alternatively, molecular spectra can be computed from the Fourier transform of time-dependent autocorrelation functions without explicit eigenstate construction [205]. In *ab initio* molecular dynamics (AIMD) [206–209], nuclei are propagated classically in real time with on-the-fly evaluations of the PES and DMS, avoiding the pre-construction of global surfaces at the expense of requiring long trajectories and extensive sampling for spectral convergence. Path integral techniques [210–213] incorporate quantum nuclear effects through imaginary-time sampling, but rely on additional semi-classical approximations to access real-time correlation functions.

These mature classical approaches have proven highly effective for small to medium-sized molecules. However, as molecular complexity increases, their scalability becomes a critical bottleneck. Eigenstate-based methods encounter rapidly growing basis sizes or high-order force-field complexity, whereas dynamical approaches are constrained by the cost of long-time propagation and extensive statistical sampling. In both paradigms, these factors lead to steeply increasing computational demands for large systems. In contrast, quantum algorithms encode the exponential growth of the vibrational Hilbert space naturally in the qubit register, shifting the scalability challenge from state representation to the availability of fault-tolerant resources.

Vibrational problems, which are central to understanding phenomena like energy transfer and spectral properties, are identified as more tractable on quantum hardware compared to electronic structure problems [214]. In spite that significant progress has been made in applying quantum computing to tackling molecular vibrational problems [214–222], there is limited focus on IR-specific applications. Our work bridges this critical gap by introducing a grid-based quantum framework capable of deriving IR spectra from time-evolved molecular wavefunctions.

Among the representation schemes essential for vibrational dynamics modelling, grid-based methods, benefited from efficient strategies such as Smolyak quadrature [223, 224] or tensor-train decompositions [225], distinguish themselves by enabling flexible discretisation of spatially localized vibrational modes.

Building on the SO-QFT method, we develop a time-dependent quantum algorithm for computing IR spectra and validate it on the water system using a quartic expansion of the PES. This framework manipulates the wavefunction of water vibrational modes in the grid-based space and the infrared information is extracted through the time propagating process. To map the proposed algorithm onto quantum registers, we design a customised set of quantum circuits that optimise qubit utilisation and minimise gate depth. Since quantum circuits are restricted to reversible and norm-preserving transformations, only unitary operations can be implemented directly. The non-unitary dipole operator therefore cannot be directly represented as a gate sequence acting solely on the system register. To

address this challenge, we introduce a probabilistic scheme that embeds the operator into a higher-dimensional unitary block using a single ancillary qubit. Classical emulation is employed to evaluate the feasibility of this algorithm, which successfully reproduce the desired vibrational characteristics including both fundamental and overtone bands with high fidelity.

The remainder of this chapter is structured as follows: Section 4.2 provides the theoretical and methodological foundation underlying the workflow developed for this work. Section 4.3 outlines the complete quantum circuit design in detail, from the initial state preparation, through the implementation of the non-unitary dipole operator and the SO-QFT time evolution scheme, to the measurement strategies utilised for deriving IR spectral information. Based on classical emulation results of the water molecule, Section 4.4 assesses the performance of this algorithm in its general feasibility, the sensitivity to varying simulation time parameters, and the quantitative impact of replacing exact components with approximate counterparts. Finally, Section 4.5 summarises the conclusions and suggestions for future research.

4.2 Theoretical Framework

In this work, the IR spectrum is obtained via the Fourier Transform of a dipole-dipole autocorrelation function sampled at discrete time points during real-time quantum evolution. We will first introduce the background elements of our approach in this section, including the Hamiltonian structure, the definition of dipole operator function, the chosen time-evolution scheme, and the theoretical basis for extracting band information, before presenting corresponding quantum circuits in the next section.

We employ the vibrational Watson Hamiltonian $H = K + V$ for water in dimensionless normal-mode coordinates Q, omitting pseudo-potential and Coriolis couplings. When denoting p_i as the dimensionless momentum conjugate to Q_i, the kinetic operator becomes:

$$K = -\sum_{i=1}^{3\mathcal{N}-6} \frac{\omega_i}{2} \frac{\partial^2}{\partial Q_i^2} = \sum_{i=1}^{3\mathcal{N}-6} \frac{\omega_i}{2} p_i^2. \tag{4.1}$$

Here ω_i are the harmonic vibrational frequencies and i runs over all vibrational normal modes. Specifically, for a non-linear molecule of $\mathcal{N}$ atoms, the vibrational dimension is $3\mathcal{N}-6$, which for triatomic water equals to three normal modes.

The PES is represented by a Taylor expansion and truncation of anharmonicities up to the fourth order gives the quartic force fields [226, 227]:

$$V = \frac{1}{2}\sum_{i=1}^{3\mathcal{N}-6}\omega_i Q_i^2 + \sum_{ijk} m_{ijk} Q_i Q_j Q_k + \sum_{ijkl} m_{ijkl} Q_i Q_j Q_k Q_l. \tag{4.2}$$

where m_{ijk} and m_{ijkl} are the cubic and quartic anharmonic force constants.

Within the Born–Oppenheimer approximation, the DMS is defined as the expectation value of the electronic dipole operator μ_{el} with respect to the electronic ground-state wavefunction $\Psi_{\mathrm{el}}(\mathbf{Q})$ at a fixed nuclear geometry:

$$\mu^{(\alpha)}(\mathbf{Q}) = \langle \Psi_{\mathrm{el}}(\mathbf{Q}) |\, \mu_{\mathrm{el}} \,| \Psi_{\mathrm{el}}(\mathbf{Q}) \rangle\,. \tag{4.3}$$

Expanding the DMS in normal-mode coordinates about the equilibrium geometry and truncating at third order yields a polynomial representation of the dipole moment:

$$\mu^{(\alpha)} = \sum_i u_i^{(\alpha)} Q_i + \sum_{ij} u_{ij}^{(\alpha)} Q_i Q_j + \sum_{ijk} u_{ijk}^{(\alpha)} Q_i Q_j Q_k, \tag{4.4}$$

where $\alpha = \{x, y, z\}$ are the axes of the body-fixed Eckart frame.

The parameters entering the equations above are derivatives of the electronic PES and DMS with respect to dimensionless normal mode coordinates. For example, the force constants ω_i, m_{ijk} and m_{ijkl} correspond to second-, third- and fourth-order derivatives of the PES, respectively. In practice, these quantities are typically computed from correlated electronic-structure calculations, either through analytic derivative techniques where available or by numerical differentiation of electronic energies and dipoles evaluated at displaced geometries.

A naive construction of the full multidimensional PES or DMS by direct evaluation on dense nuclear grids becomes computationally prohibitive beyond small systems. Consequently, practical treatments rely on parameterised representations, such as polynomial force fields, n-mode expansions, or other fitted models derived

from a finite set of electronic-structure calculations [228–232]. Although this approach avoids dense-grid sampling, the number of expansion coefficients grows rapidly with dimensionality and expansion order, and each coefficient ultimately depends on electronic structure data whose cost itself increases steeply with molecular size. For the water system considered here, we adopt the force constants and dipole coefficients reported by [227], which were obtained from correlated *ab initio* calculations at a finite set of geometries and subsequent least-squares fitting in normal coordinates.

We conduct the time dependent calculation of IR spectra within a wavefunction-based framework, where we represent the wavefunction on a discrete grid-based space. The dipole moment operator is subsequently applied on the initial state, resulting in the transformed state $|\Psi_\mu(t_0)\rangle = \mu\,|\Psi(t_0)\rangle$, so as to extract the dynamics of dipole-induced transitions [233–235]. We then adopt the second-order SO-QFT method to evolve the dipole operated ground state wavefunction by time. The high-order polynomial structure of V presents a considerable gate depth demands in the quantum circuit. To address this, we select a more efficient scheme where the kinetic energy operator takes on the half-time step split rather than the potential operator:

$$|\Psi_\mu(t+dt)\rangle = e^{-iHdt}\,|\Psi_\mu(t)\rangle \approx U_K U_V U_K\,|\Psi_\mu(t)\rangle\,, \tag{4.5}$$

with time evolution operators $U_K = e^{-iKdt/2}$ and $U_V = e^{-iVdt}$ implemented in the momentum and position spaces, respectively. This adjustment allows us to minimise gate depth, as each time step only requires a single potential operation. Although two additional QFT operations are needed at the initial and final time points, the overall gate count is still considerably lower than that of the more conventional splitting pattern, where the potential is split across half-time steps. We confirm from classical emulation results that the IR spectral outcomes derived from these two patterns are comparable, with no significant difference exhibited.

During the propagating time length T, we conduct separate simulations for different Eckart directions and record their corresponding dipole-dipole autocorrelations

$$A_\mu(t) = \langle\Psi_\mu(t_0)|\,e^{-iHt}\,|\Psi_\mu(t_0)\rangle$$

at each time point t. While we are assuming an infinite time of the propagation by practically recording a finite autocorrelation function, a damping function $D(t)$ is multiplied onto the autocorrelation function $A_\mu(t)$ to reduce the artifacts resulted from Gibbs phenomenon. It is equivalent to manually damp the autocorrelation to zero for the unreached regions out of our propagation window. In specifying $D(t)$, several options are available, such as $\cos(\pi t/2T)$ [140, 234] and $\cos\left(\pi t/2T^2\right)$ [235], both of which yield similar outputs with no significant deviations observed between them.

Under this time-dependent framework, the IR cross section per molecule is expressed as [233–235]:

$$\sigma(E) = \frac{E}{3c\epsilon_0\hbar^2}\mathbb{R}e\int_0^\infty e^{i(E+E_0)t}A_\mu(t)dt, \tag{4.6}$$

which in practice equals to applying Fourier Transform on the post-modified $A_\mu(t)$, followed by multiplication of specific scaling factors along with the total dipole strength $\langle\Psi_\mu(t_0)|\Psi_\mu(t_0)\rangle$. Here the E_0 term represents the ZPE calculated based on the initial ground state, and functions as a reference baseline. It is necessary to apply a ZPE shift when determining band positions from the final IR spectrum and the E term therefore denotes the vibrational energy relative to this ZPE.

To obtain a commonly reported integrated intensity in km/mol, we first form the molar cross section and integrate over the selected spectral window:

$$I_{\mathrm{IR}} = \int N_A\sigma(E)\mathrm{d}E. \tag{4.7}$$

The contributions from different Eckart directions are then combined to produce absolute band intensity calculations.

4.3 Quantum Implementation

We aim to develop scalable quantum circuit architectures that are directly applicable to future noise-free, fault-tolerant quantum hardwares. The complete quantum implementation for simulating IR spectral data is structured into four key components: approximating and preparing the initial state, applying the non-unitary dipole operator, evolving the system via SO-QFT time operators constructed from

polynomial Hamiltonian terms, and measuring the dipole-dipole autocorrelation $A_\mu(t)$ throughout the time evolution process. The IR spectra is eventually produced through Fourier Transform on the time-dependent autocorrelation. In contrast to Chapter 3, here we restrict the measurement strategy to the Hadamard-test approach. In the present IR simulations, the autocorrelation decays too slowly within the finite propagation window, rendering damping functions indispensable for obtaining well-resolved spectra. This requirement necessitates explicit access to $A_\mu(t)$ and therefore favours the Hadamard formulation over QPE, as the latter does not readily accommodate such time-domain modifications. Since the measurement of the autocorrelation function using the Hadamard test has already been detailed in Section 2.3, the following analysis will focus on the first three components.

4.3.1 Initial State Preparation

The discretisation of grid-based spaces facilitates the use of adaptive grid densities to either optimise state fidelity or reduce computational resources. Due to the absence of singularities in the potential, vibrational wavefunctions are smooth and a low grid density will suffice to represent the relevant normal modes. For each normal mode, we allocate $2^4 = 16$ grids within a spatial range of [-5, 5] in dimensionless unit, corresponding to $n = 4$ qubits per quantum register. In terms of water, this context leads to a total 12 qubits distributed across 3 registers.

Here we consider two possibilities for the initial state: the harmonic ground state, used as a cost-saving approximation, and the true ground state of the anharmonic Hamiltonian introduced in Section 4.2. We prepare the latter state via Imaginary Time Evolution (ITE) [236, 237] on our grid-based spaces. In this approach, the system is evolved in imaginary time $\tau = it$, under which higher-energy components exponentially decay, thereby driving the system towards its ground state. The tensor product of the approximated harmonic wavefunctions acts as a suitable initial guess, allowing a rapid convergence to the target anharmonic ground state.

To clarify the convergence mechanism, let $\{|E_x\rangle\}$ denote the orthonormal eigenbasis of H with eigenvalues $E_0 < E_1 \leq E_2 \leq \cdots$. Expanding the initial

guess in this basis gives $|\Psi_{\text{Gauss}}\rangle = \sum_x c_x |E_x\rangle$. After imaginary time τ, and subsequent normalisation, the state becomes

$$\begin{aligned} |\Psi_{\text{ITE}}\rangle &= \frac{e^{-H\tau}\,|\Psi_{\text{Gauss}}\rangle}{\|\, e^{-H\tau}\,|\Psi_{\text{Gauss}}\rangle\|} = \frac{\sum_x c_x e^{-E_x\tau}|E_x\rangle}{\sqrt{\sum_x |c_x|^2 e^{-2E_x\tau}}} \\ &= \frac{c_0|E_0\rangle + \sum_{x\geq 1} c_x e^{-(E_x-E_0)\tau}|E_x\rangle}{\sqrt{|c_0|^2 + \sum_{x\geq 1}|c_x|^2 e^{-2(E_x-E_0)\tau}}}. \end{aligned} \tag{4.8}$$

Here the global factor $e^{-E_0\tau}$ cancels under normalisation. Since $E_x > E_0$ for $x \geq 1$, all excited-state contributions are exponentially suppressed relative to the ground-state component. The normalised state therefore converges to $|E_0\rangle$ in the limit $\tau \to \infty$, provided that $c_0 \neq 0$, i.e., the initial guess has nonzero overlap with the true ground state. In practice, the imaginary time τ is increased until observables, such as the energy expectation value, converge within a prescribed tolerance.

Implementing the ITE procedure is straightforward on classical computers, though it becomes rather tedious and expensive when applied to quantum devices. Quantum algorithms, including variational [238, 239], probabilistic [240, 241], and fully quantum methods [242, 243], provide diverse circuits for this purpose. However, the presence of polynomial terms as high as fourth order in the potential operator makes the quantum implementation of ITE significantly more computationally demanding.

To improve efficiency and lower costs, we further explore strategies for circuit-depth reduction. Results derived from classical emulation of the water system (see Section 4.4) confirm that directly using harmonic wavefunctions for its initial state preparation is sufficient to meet our requirements in precision and accuracy. As long as the potential operator for following real time evolution preserves its anharmonicities, the harmonic wavefunctions without further ITE process delivers spectrum outputs comparable to those obtained from the anharmonic version of the ground state, suggesting its viability.

One key advantage of using these harmonic wavefunctions is the ability to prepare initial states for various normal modes in parallel. Such approximation greatly simplifies the computational complexity as each wavefunction is generated independently

in its own register. This architecture makes scaling to higher-dimensional vibrational systems highly efficient by merely adding more registers without increasing gate depth for state preparation. On the other hand, the construction of Gaussian distribution benefits from its smoothness, which eliminates the need for high grid densities. In this chapter, we still select uniformly controlled rotations, i.e., $\mathbf{R_y}$ and **CNOT** gates, to prepare the initial real-valued harmonic states for each normal mode with a gate depth of only 29, as demonstrated in Chapter 3.

4.3.2 Non-Unitary Dipole Operator

The quantum simulation begins with the application of the dipole operator onto the initial state. As discussed in Section 4.3.1, a harmonic approximation to the initial state is feasible and effective. Similarly, approximations in the dipole operator are also explored to reduce computational complexity. In agreement with standard practice in vibrational spectroscopy, we find that truncating the dipole operator to first order is sufficient to reproduce the fundamental bands (see section 4.4). Strictly speaking, a purely linear dipole leads to vanishing intensity for overtone transitions. However, in the context of our simulations, the anharmonic Hamiltonian produces state mixing that yields non-zero overtone signals even when the dipole is linear, although accurate calculations of their absolute intensities does require inclusion of higher-order terms. No matter how high or low the polynomial truncation is taken, difficulties in quantum implementation arise due to the inherently non-unitary nature of the dipole operator, which inevitably requires another approximation strategy that balances computational feasibility with physical fidelity for its quantum circuit constructions.

The non-unitary challenge presented from the dipole operator is similar to that of imaginary time evolution in requiring a non-unitary operation, where probabilistic quantum circuit designs become highly applicable. Drawing inspiration from the probabilistic imaginary time evolution illustrated in [244], we build on their circuit architecture for applications of our non-unitary dipole operator. The

realisation of $\mu^{(\alpha)}$ requires an ancillary qubit to mediate probabilistic control, together with a phase operator

$$\Theta = \arccos \frac{\tilde{\mu}^{(\alpha)} + \sqrt{1 - (\tilde{\mu}^{(\alpha)})^2}}{\sqrt{2}}. \tag{4.9}$$

To define this phase angle, we rescale the physical dipole operator by a fixed constant β with the same physical units and introduce the dimensionless quantity $\tilde{\mu} = \mu/\beta$. For Eq. 4.9 to be well defined, β is chosen to satisfy $\|\tilde{\mu}\|_\infty \leq 1$, ensuring Θ is real-valued.

Since the exact calculation of Θ is analytically intractable, we therefore expand it as a Taylor series in powers of $\tilde{\mu}^{(\alpha)}$ about the origin to overcome the hurdle:

$$\Theta \approx \frac{\pi}{4} - \tilde{\mu}^{(\alpha)}. \tag{4.10}$$

This approximation is a small-parameter expansion and thus requires $\|\tilde{\mu}\|_\infty \ll 1$, so that the neglected $\mathcal{O}(\tilde{\mu}^2)$ terms are negligible. Consequently, the choice of β is not unique, as long as it is sufficiently large to ensure that the overall magnitude of $\tilde{\mu}$ lies within the regime of validity of the Taylor truncation. Accordingly, the practical circuit employs two explicit phases, $\theta_0 = \frac{\pi}{4}$ and $\theta_1 = -\tilde{\mu}^{(\alpha)}$, as depicted in Figure 4.1.

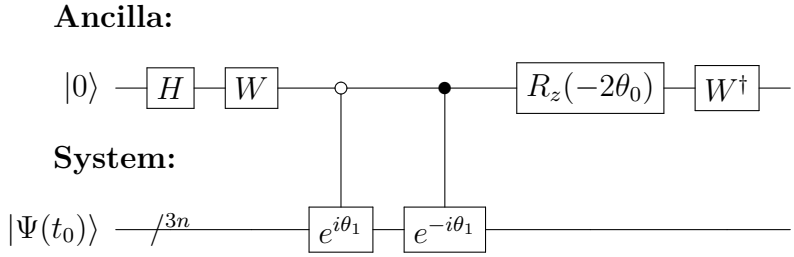

Figure 4.1: Quantum circuit for implementing the non-unitary dipole moment operator. The single-qubit gate $\mathbf{W}$ is defined as $\mathbf{W} = \frac{1}{\sqrt{2}} \begin{pmatrix} 1 & -i \\ 1 & i \end{pmatrix}$.

This circuit converts the $|\Psi(t_0)\rangle \otimes |0\rangle$ to the

$$\tilde{\mu}^{(\alpha)} |\Psi(t_0)\rangle \otimes |0\rangle + \sqrt{1 - (\tilde{\mu}^{(\alpha)})^2} |\Psi(t_0)\rangle \otimes |1\rangle ,$$

which indicates that the successful application of $\tilde{\mu}^{(\alpha)}$ is contingent on measuring the ancilla qubit in the $|0\rangle$ state, with failure cases (ancilla in $|1\rangle$) rendering the

results invalid. Despite the inherent probabilistic nature, this approach offers exceptional adaptability in tackling non-unitary operations for quantum hardware implementation.

We evaluate the inner product between the exact dipole-operated state and the approximate counterpart generated by the circuits in Figure 4.1, obtaining an overlap greater than 0.99999. Furthermore, across simulations with various time parameters, the fundamental bands derived from the approximate preparation, where first-order dipole operators are implemented via the approximate preparation circuit and applied to the approximate harmonic ground state (see Table A.1 in the Appendix A), show excellent agreement with those from the corresponding exact preparation (see the last row of Table 4.5 in Section 4.4.2). The band positions are essentially identical, and the maximum deviation in band intensities remains below 9.5%. Such close correspondence demonstrates the robustness of Eq. 4.10, enabling us to bypass the mathematical complexity related to Θ and simplify the circuit with high fidelity.

Concretely, the operation $e^{\pm i\theta_1}$ used in Figure 4.1 is decomposed into a sequence of unitary blocks specified as:

$$e^{\pm i\theta_1} = e^{\pm i\tilde{\mu}^{(\alpha)}} = \prod_i U^{(\alpha)}_{\mathrm{DM},i} \prod_{ij} U^{(\alpha)}_{\mathrm{DM},ij} \prod_{ijk} U^{(\alpha)}_{\mathrm{DM},ijk} \cdots \tag{4.11}$$

where

$$\begin{aligned} U^{(\alpha)}_{\mathrm{DM},i} &= e^{\pm i\tilde{u}^{(\alpha)}_i Q_i}, \\ U^{(\alpha)}_{\mathrm{DM},ij} &= e^{\pm i\tilde{u}^{(\alpha)}_{ij} Q_i Q_j}, \\ U^{(\alpha)}_{\mathrm{DM},ijk} &= e^{\pm i\tilde{u}^{(\alpha)}_{ijk} Q_i Q_j Q_k}. \end{aligned}$$

Here the dipole moment operator $\tilde{\mu}^{(\alpha)}$ accommodates polynomial terms of different orders, depending on the level of truncation selected. While Eq. 4.11 provides an exact factorisation, its implementation via ancilla-assisted post-selection renders the procedure intrinsically probabilistic. The associated success probability directly impacts the expected number of repetitions required per time step. Because autocorrelation functions are evaluated over many time steps, this sampling overhead

accumulates and substantially increases the total runtime unless mitigated, for instance through amplitude amplification [245, 246].

In Chapter 3, we detail the implementation of circuits for e^{if} with f being first- and second-order polynomials using $\mathbf{U_1}$ gates, while the extension to third-order cases is reserved for further illustration in Section 4.3.3. Allocating n qubits in each normal mode register, the resulting circuit depths for unitaries $U^{(\alpha)}_{\mathrm{DM},i}$, $U^{(\alpha)}_{\mathrm{DM},ij}$, and $U^{(\alpha)}_{\mathrm{DM},ijk}$ are summarised in Table 4.1, corresponding to n, n^2 and $\mathcal{O}(n^3)$ gates, respectively. The ancilla-specific gates in Figure 4.1, such as $\mathbf{H}$, $\mathbf{W}$, $\mathbf{R_z}$ and $\mathbf{W}^\dagger$, are aligned in parallel with neighbouring initial state preparation and time evolution segments, thereby avoiding any contribution to overall circuit depth.

Terms in $e^{\pm i\tilde{\mu}^{(\alpha)}}$		Gate Depth	n=4
$U^{(\alpha)}_{\mathrm{DM},i}$		n	n
$U^{(\alpha)}_{\mathrm{DM},ij}$	$i=j$	n^2	16
	$i\neq j$	n^2	16
$U^{(\alpha)}_{\mathrm{DM},ijk}$	$i=j=k$	$5n^3-12n^2+8n$	160
	$i=j\neq k$	$5n^3-4n^2$	256
	$i\neq j\neq k$	$5n^3$	320

Table 4.1: Gate depths for the constituent terms arising in applying the non-unitary dipole moment operator.

As an illustrative case, we consider the water system with dipole operators $\mu^{(x)}$ and $\mu^{(z)}$, both truncated at third order. The unitary operations required for their implementation are explicitly shown as circuit blocks in Figure 4.2. Using the gate counts from Table 4.1, the depth associated with a single unitary block, $e^{\pm i\tilde{\mu}^{(\alpha)}}$, scales as $20n^3-18n^2+9n$ gates for $\alpha=x$ and $30n^3-36n^2+18n$ gates for $\alpha=z$ (e.g. 1,028 and 1,416 gates when $n=4$). As both the positive and negative exponentials must be executed under ancilla control, the total cost for each dipole operator is twice these values. Comparatively, a first-order truncation in $\mu^{(\alpha)}$ offers a low-depth alternative, demanding only $2n$ and $4n$ gates for $\alpha=x$ and $\alpha=z$, respectively.

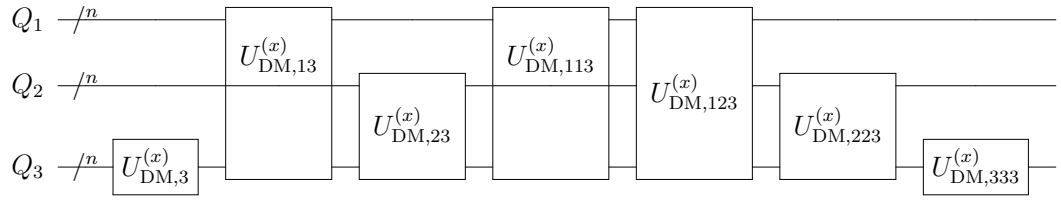

(a) $e^{\pm i\tilde{\mu}^{(x)}}$

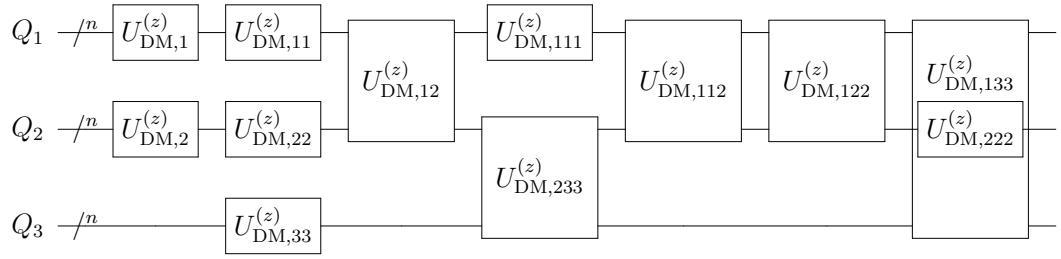

(b) $e^{\pm i\tilde{\mu}^{(z)}}$

Figure 4.2: Unitary operations required for implementing $e^{\pm i\tilde{\mu}^{(\alpha)}}$ on the water system.

4.3.3 SO-QFT Time Evolution

The preliminary operation of dipole moment functions establishes a dipole operated ground state as the starting state for the following time evolution, which we perform using the second-order SO-QFT method. In the potential component of the time evolution operator, polynomial terms often appear in the exponentials as second-order, third-order, and fourth-order forms:

$$e^{-iVdt} = \prod_{ij} U_{V,ij} \prod_{ijk} U_{V,ijk} \prod_{ijkl} U_{V,ijkl} \cdots , \tag{4.12}$$

with

$$\begin{aligned} U_{V,ij} &= e^{-i\omega_i Q_i Q_j dt}, \\ U_{V,ijk} &= e^{-im_{ijk} Q_i Q_j Q_k dt}, \\ U_{V,ijkl} &= e^{-im_{ijkl} Q_i Q_j Q_k Q_l dt}, \end{aligned}$$

each demanding tailored quantum circuit design. Here the indices $\{i, j, k, l \cdots\}$ are not necessarily distinct and need not correspond to different normal modes. It is common to encounter coinciding indices, in which case identical indices indicate the same normal mode coordinates and thus the same quantum register. For

example, when $i = j$, $U_{V,ij}$ reduces to a specific class whose exponent involves quadratic-order polynomials.

In general, the polynomial order in the exponentials of these unitaries determines the associated gate complexities, with $U_{V,ij}$, $U_{V,ijk}$, and $U_{V,ijkl}$ requiring n^2, $\mathcal{O}(n^3)$, $\mathcal{O}(n^4)$ gates, respectively. In the following discussions, qubits within a register of normal mode Q_i are denoted as $q_{i'}$ accordingly. With n qubits assigned to a specific Q_i register, the number of the possible i' values becomes n, i.e., $q_{i'} \in \{q_0, q_1, \cdots, q_{n-1}\}$.

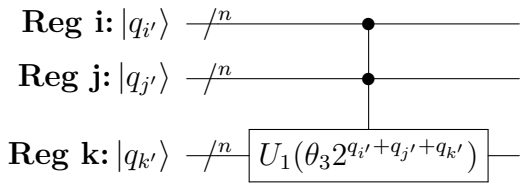

Figure 4.3: Quantum circuit for implementing $U_{V,ijk}$, the time evolution operators of third-order potential terms.

We first illustrate the general strategy for building circuits that implement $U_{V,ijk}$ in Figure 4.3, accompanied by an angle definition of $\theta_3 = m_{ijk}dt$. In this structure, we assign registers of the two normal modes, Q_i and Q_j, as controlling registers, while the third Q_k one serves as the target register accommodating $\mathbf{U_1}$ gates. This schematic circuit corresponds to the case $i \neq j \neq k$, where all indices differ and three distinct normal modes are involved. Its fully expanded representation can be depicted by traversing all control-target configurations across the three registers, which manifests as n^3 possible combinations of the involved qubits $\{q_{i'}, q_{j'}, q_{k'}\}$ and consequently n^3 controlled-controlled gates.

In cases where two or all three indices in $\{i, j, k\}$ coincide, the overlap of registers reduces the number of control nodes. For the $i = j = k$ case, all controlling and target qubits ($q_{i'}$, $q_{j'}$ and $q_{k'}$) reside within the same n-qubit register. Similarly, in the $i = j \neq k$ case, the circuit complexity is reduced as Q_i and Q_j refer to the same normal mode, allowing $q_{i'}$ and $q_{j'}$ within the same register to coincide under certain configurations. When allocating $n = 4$ qubits for each register, we present two example fragment circuits in Figure 4.4 to illustrate $i = j = k$ and $i = j \neq k$

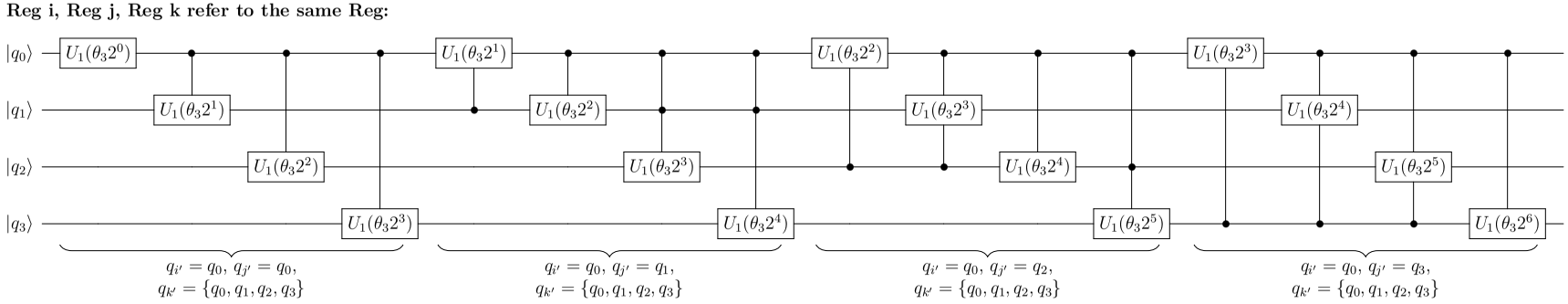

(a) When $i = j = k$, the operation only involves one register.

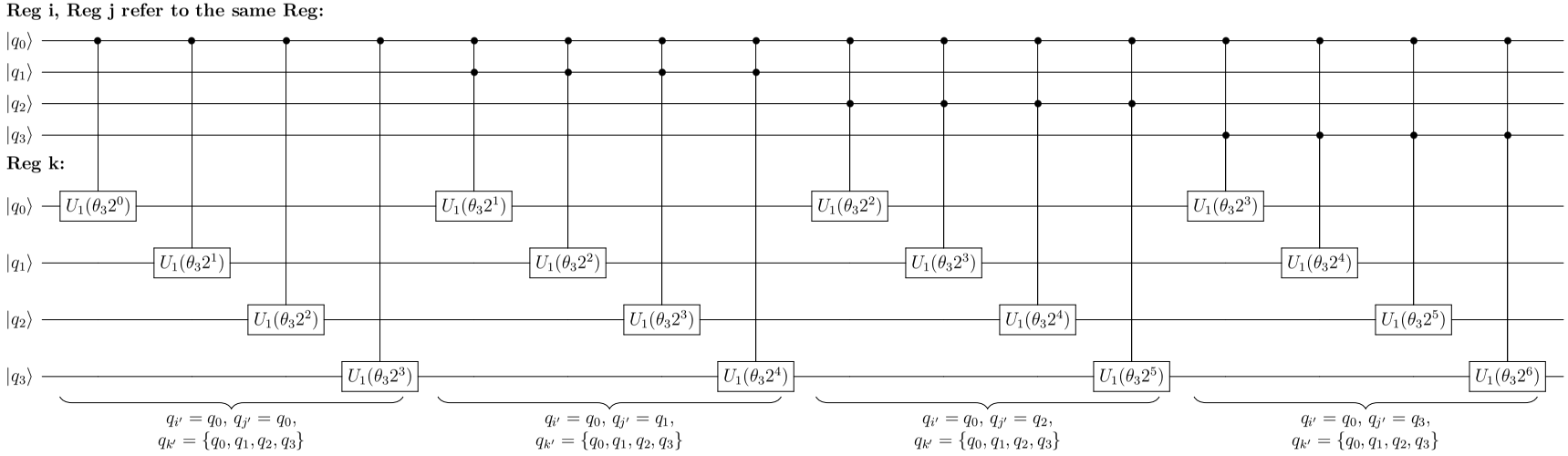

(b) When $i = j \neq k$, the operation involves two register.

Figure 4.4: Example fragment quantum circuit of $U_{V,ijk}$ operators when fixing $q_{i'} = q_0$ and each register has 4 qubits.

cases. These examples fix the controlling qubit $q_{i'} = q_0$ and iteratively traverse all possible controlling $q_{j'}$ and target $q_{k'}$ options. The proposed architecture is readily adaptable to other values of $q_{i'}$ (i.e., $\{q_1, q_2, q_3\}$), by following the consistent logic.

Scaling to the total circuit depth involves summing contributions from individual fragment circuits. Given that there are 4 possible values of $q_{i'}$ under the $n = 4$ setting, the full circuit depth for either $i = j = k$ or $i = j \neq k$ cases is 4 times the 16 gate count of the fragment circuits depicted in Figure 4.4. Extending this approach to n-qubit registers also yields a generalised gate count of n^3.

We further decompose these multi-controlled structures into circuits operating at a more elementary level. As a controlled-controlled gate, $\mathbf{C^2U}$, can be implemented using 5 two-qubit gates [54], we accordingly convert the naive gate estimate of n^3 for $U_{V,ijk}$ to $5n^3 - 12n^2 + 8n$, $5n^3 - 4n^2$ and $5n^3$ for the cases $i = j = k$, $i = j \neq k$ and $i \neq j \neq k$, respectively, as listed in Table 4.2.

U_V		Gate Depth	$n = 4$
$U_{V,ij}$		n^2	16
$U_{V,ijk}$	$i = j = k$	$5n^3 - 12n^2 + 8n$	160
	$i = j \neq k$	$5n^3 - 4n^2$	256
	$i \neq j \neq k$	$5n^3$	320
$U_{V,ijkl}$	$i = j = k = l$	$21n^4 - 96n^3 + 148n^2 - 72n$	1,312
	$i = j = k \neq l$	$21n^4 - 48n^3 + 28n^2$	2,752
	$i = j \neq k = l$	$21n^4 - 32n^3 + 12n^2$	3,520
	$i = j \neq k \neq l$	$21n^4 - 16n^3$	4,352
	$i \neq j \neq k \neq l$	$21n^4$	5,376

Table 4.2: General gate depth calculations of time evolution operators $U_{V,ij}$, $U_{V,ijk}$ and $U_{V,ijkl}$.

The fourth order terms in the Hamiltonian generates time evolution operators of the form $U_{V,ijkl}$, which requires circuits with up to 3-controlled operations. By defining $\theta_4 = m_{ijkl}dt$, Figure 4.5 schematically illustrates the circuit structure of $U_{V,ijkl}$ for the generic case $i \neq j \neq k \neq l$ (i.e., Q_i, Q_j, Q_k and Q_l correspond to four different normal modes). This configuration results in n^4 $\mathbf{C^3U_1}$ gates.

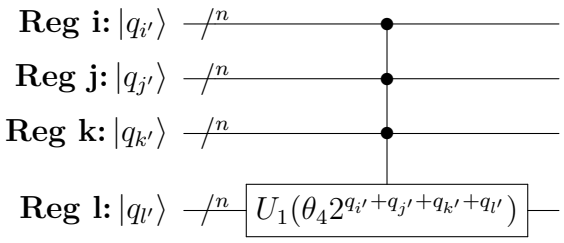

Figure 4.5: Quantum circuit for implementing $U_{V,ijkl}$, the time evolution operators of fourth-order potential terms.

As illustrated in Figure 4.6, a $\mathbf{C^3U}$ gate requires 2 ancillary qubits and decomposes into 4 $\mathbf{C^2U}$ gates and 1 two-qubit gate. Given that each $\mathbf{C^2U}$ decomposes into 5 two-qubit gates, the total cost amounts to 21 two-qubit gates. The circuit shown in Figure 4.5 therefore translates to $21n^4$ two-qubit gates. More generally, any multi-controlled gate $\mathbf{C^nU}$ (with $\mathbf{n} > 2$) can be constructed from $2(\mathbf{n}-1)$ $\mathbf{C^2U}$ plus a two-qubit operations, using a minimal number of $\mathbf{n}-1$ ancillary qubits initialised and returned to the state $|0\rangle$.

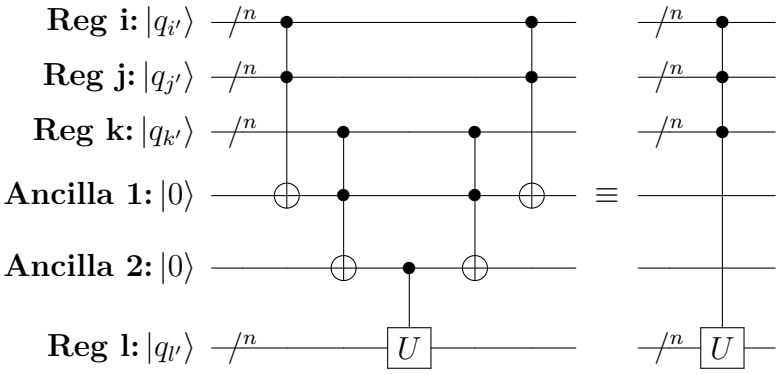

Figure 4.6: Decomposition of one $\mathbf{C^3U}$ gate through sequences of two-qubit and three-qubit gates.

Other scenarios of $\{i, j, k, l\}$, where some of the indices coincide, exhibit reduced circuit depth due to overlaps in control qubits. Figure 4.7-4.10 display representative circuit fragments for the remaining index patterns, drawn with $n = 4$ qubits per normal mode register for illustration. Each figure consists of two subplots: panel (a) depicts the case $q_{i'} = q_0$ and $q_{j'} = q_0$, while panel (b) exemplifies $q_{i'} = q_0$ and $q_{j'} = q_1$.

To evaluate the full gate depth, we systematically traverse all qubit assignments. Starting with fixed $q_{i'} = q_0$, one must account for all possible values of $q_{j'}$. The circuit in panel (a) covers one case, while three additional circuits identical in depth

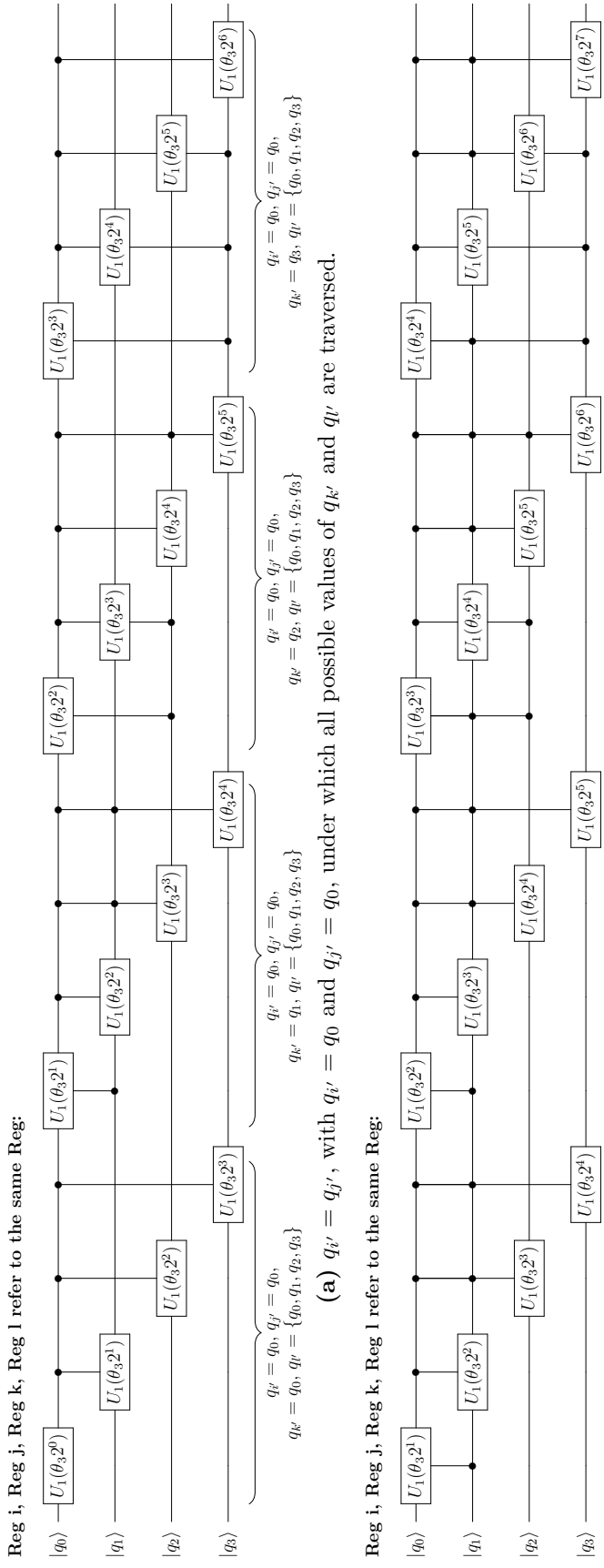

(a) $q_{i'} = q_{j'}$, with $q_{i'} = q_0$ and $q_{j'} = q_0$, under which all possible values of $q_{k'}$ and $q_{l'}$ are traversed.

(b) $q_{i'} \neq q_{j'}$, with $q_{i'} = q_0$ and $q_{j'} = q_1$, under which all possible values of $q_{k'}$ and $q_{l'}$ are traversed.

Figure 4.7: Example fragment circuit of $U_{V;ijkl}$ when $i = j = k = l$ (i.e., Q_i, Q_j, Q_k and Q_l indicate the same 4-qubit register).

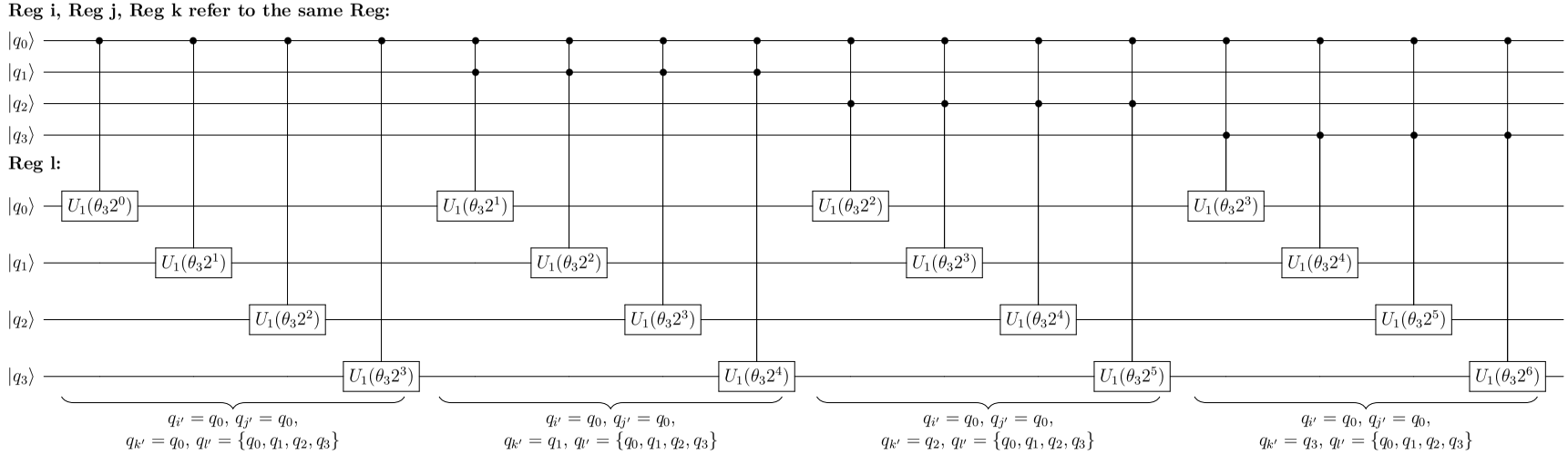

(a) $q_{i'} = q_{j'}$, with $q_{i'} = q_0$ and $q_{j'} = q_0$, under which all possible values of $q_{k'}$ and $q_{l'}$ are traversed.

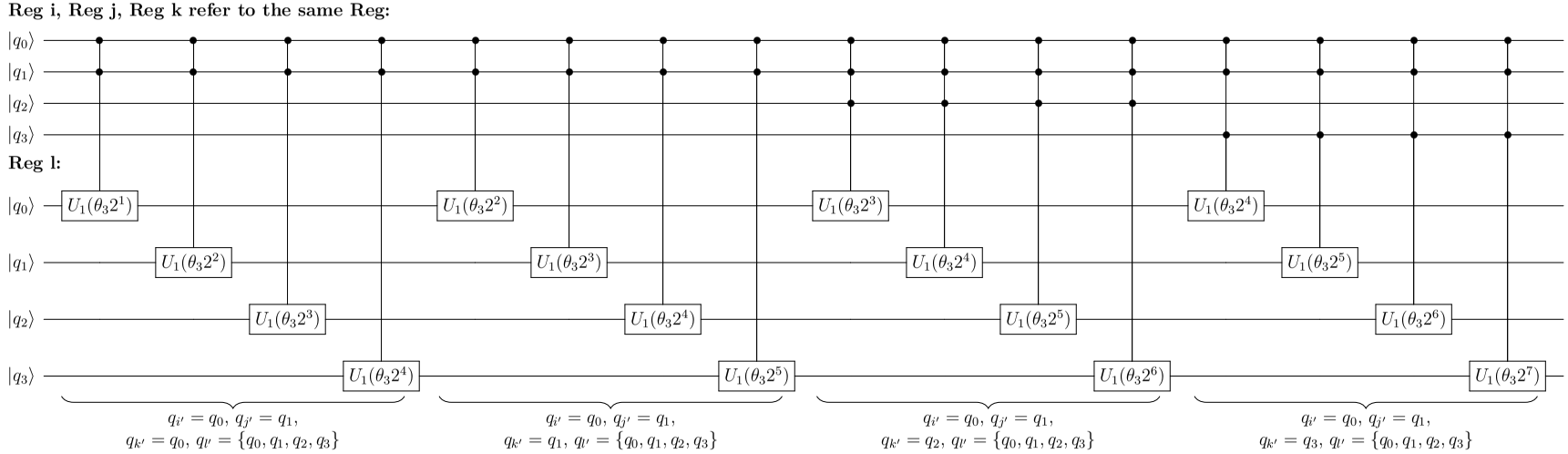

(b) $q_{i'} \neq q_{j'}$, with $q_{i'} = q_0$ and $q_{j'} = q_1$, under which all possible values of $q_{k'}$ and $q_{l'}$ are traversed.

Figure 4.8: Example fragment circuit of $U_{V,ijkl}$ when $i = j = k \neq l$ (Q_i, Q_j and Q_k indicate the same register) with 4 qubits in each register.

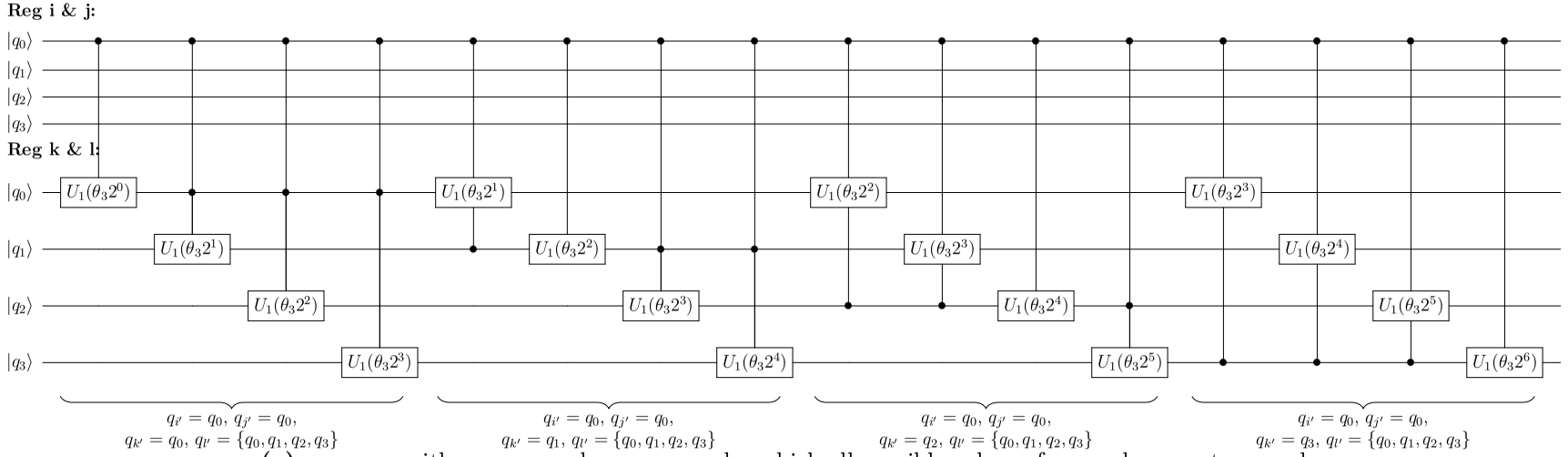

(a) $q_{i'} = q_{j'}$, with $q_{i'} = q_0$ and $q_{j'} = q_0$, under which all possible values of $q_{k'}$ and $q_{l'}$ are traversed.

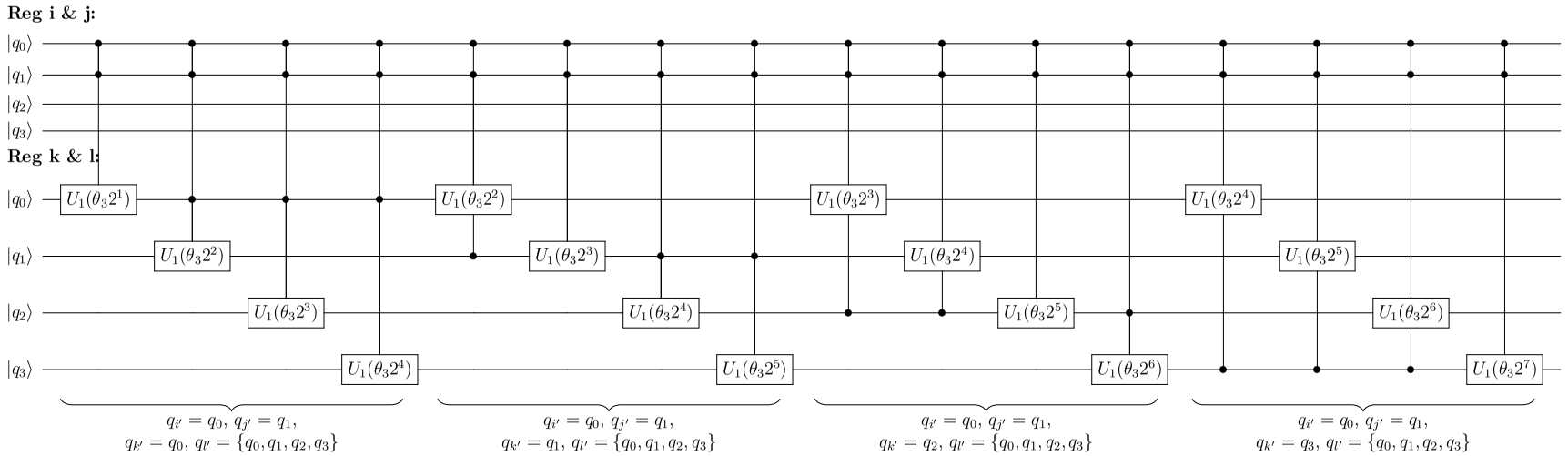

(b) $q_{i'} \neq q_{j'}$, with $q_{i'} = q_0$ and $q_{j'} = q_1$, under which all possible values of $q_{k'}$ and $q_{l'}$ are traversed.

Figure 4.9: Example fragment circuit of $U_{V,ijkl}$ when $i = j \neq k = l$ (Q_i and Q_j indicate the same register, Q_k and Q_l indicate the same register) with 4 qubits in each register.

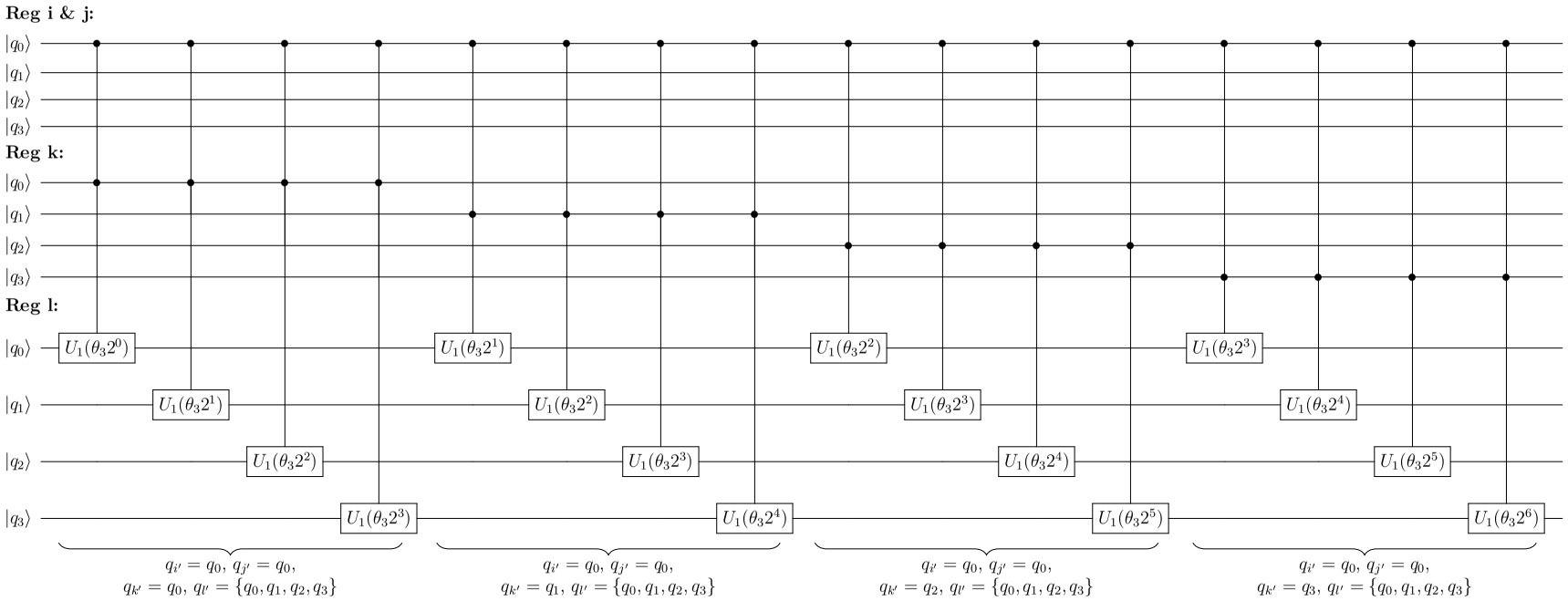

(a) $q_{i'} = q_{j'}$, with $q_{i'} = q_0$ and $q_{j'} = q_0$, under which all possible values of $q_{k'}$ and $q_{l'}$ are traversed.

Figure 4.10: Example fragment circuit of $U_{V,ijkl}$ when $i = j \neq k \neq l$ (Q_i and Q_j indicate the same register) with 4 qubits in each register, with panel (a) shown here; continued on the next page.

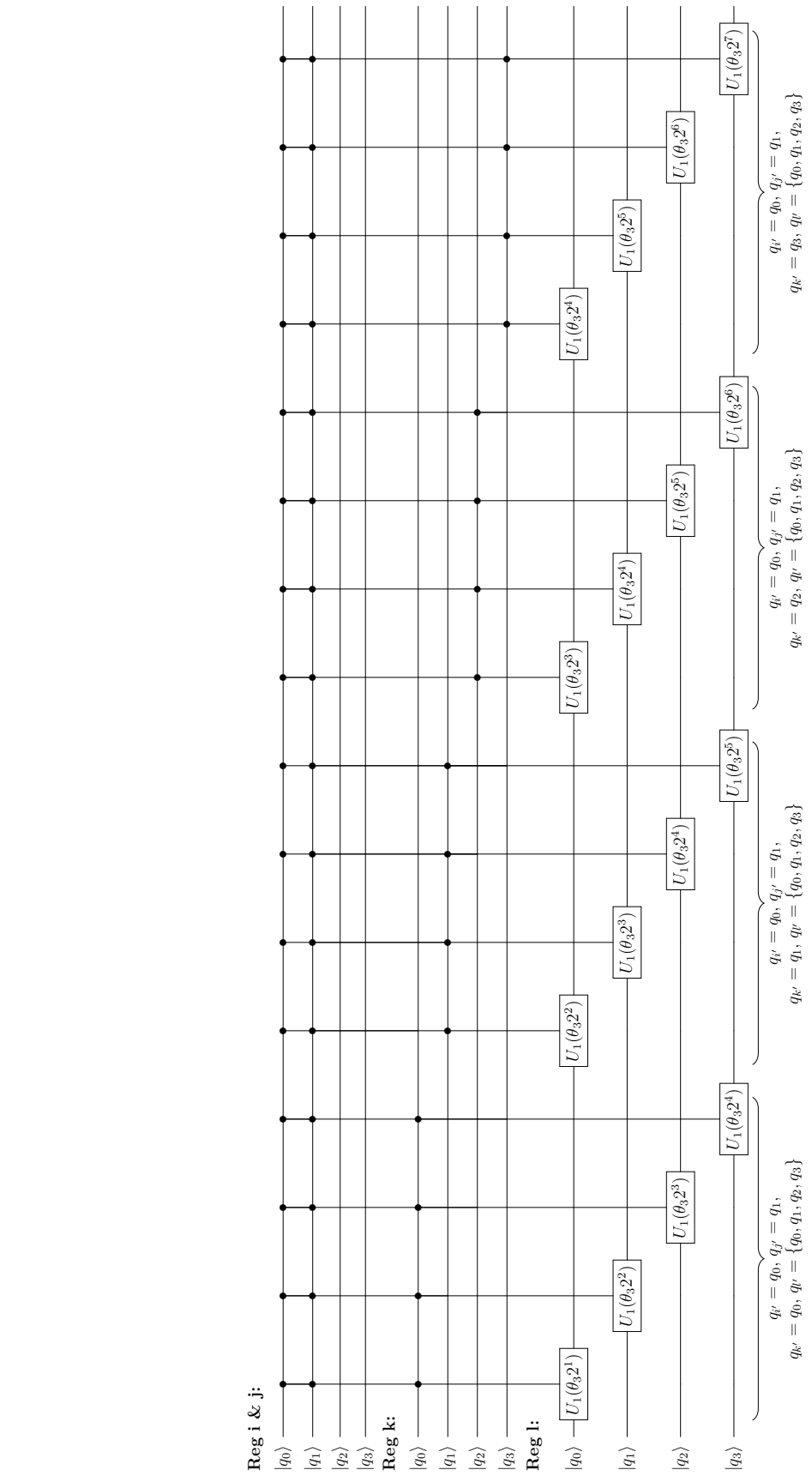

(b) $q_{i'} \neq q_{j'}$, with $q_{i'} = q_0$ and $q_{j'} = q_1$, under which all possible values of $q_{k'}$ and $q_{l'}$ are traversed.

Figure 4.10: Example fragment circuit of $U_{V;ijkl}$ when $i = j \neq k \neq l$ (Q_i and Q_j indicate the same register) with 4 qubits in each register (continued from the previous page). Panel (b).

to panel (b) cover the remaining $q_{j'} \in \{q_1, q_2, q_3\}$. Thus, the total contribution under $q_{i'} = q_0$ is $N_{(a)} + 3N_{(b)}$, where $N_{(a)}$ and $N_{(b)}$ denote the depths of the circuits in panels (a) and (b), respectively. Repeating the same procedure for $q_{i'} \in \{q_1, q_2, q_3\}$ yields three further groups of equal contribution, leading to a total of $4(N_{(a)} + 3N_{(b)})$ gates. The generalisation to arbitrary n follows straightforwardly, and the resulting classifications of gate depths across different i, j, k, l scenarios are summarised in Table 4.2.

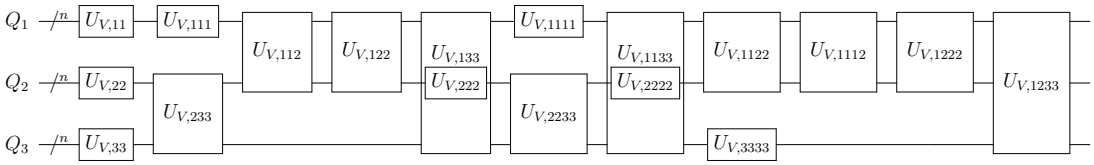

Figure 4.11: Unitary operations required for implementing $U_V = e^{-iVdt}$ on the water system.

Evolution Unitaries		Gate Depth	$n = 4$
U_V	all $U_{V,ij}$ terms	$3n^2$	48
	all $U_{V,ijk}$ terms	$30n^3 - 40n^2 + 16n$	1,344
	all $U_{V,ijkl}$ terms	$189n^4 - 496n^3 + 536n^2 - 216n$	24,352
U_K		$n^2 \times 3$ registers	48
QFT (or QFT^{-1})		$(n^2/2 + n) \times 3$ registers	36
U_KQFT$^{-1}U_V$QFTU_K		$189n^4 - 466n^3 + 508n^2 - 194n$	25,912

Table 4.3: Gate depth calculations of the time evolution section on the water system within single time step.

Using the water force field as an example, we list the unitaries responsible for implementing its U_V in Figure 4.11, together with the associated registers. The resulting single-step gate depth for implementing this U_V is reported in Table 4.3. The kinetic component U_K is local and diagonal in the momentum space with a quadratic form as shown in Eq. 4.1. Thus, it exhibits a gate complexity similar to $U_{V,ij}$, scaling as n^2 gates for an n-qubit register. When incorporating contributions from all potential and kinetic components with the QFT processes, a single time step of time evolution on the water system involves $189n^4 - 466n^3 + 508n^2 - 194n$ gates (i.e., 25,912 gates for $n = 4$). Extending this to the complete time evolution

segment, the cumulative circuit depth becomes n_t multiples of the single time step gate count, with n_t being the time steps propagated.

4.4 Characteristic Peak Analysis

This work employs the time-dependent SO-QFT framework to extract infrared properties in grid-based representations, offering an alternative to the widely used time-independent methodologies. We now use the illustrative water system to evaluate the overall performance of our algorithm, examining across three aspects: 1) its fidelity in reproducing characteristic IR bands against exact variational references, 2) the optimal selection of time evolution parameters, and 3) the robustness of approximation schemes applied in the initial state and dipole operator expressions. Specifically, we focus on two critical spectroscopic metrics: band positions and their absolute band intensities.

The determination of band positions is achieved through calculating the centroid $\widetilde{\upsilon}_c$ of the spectral data, i.e., the weighted average of wavenumbers based on their intensities:

$$\widetilde{\upsilon}_c = \frac{\sum_i \widetilde{\upsilon}_i \sigma_i}{\sum_i \sigma_i}, \tag{4.13}$$

where $\widetilde{\upsilon}_i$ and σ_i are the wavenumber and IR cross section at the i^{th} data point, respectively. For each band, the analysis window is empirically chosen by inspection of the spectrum so as to capture the full extent of the target peak while minimising contamination from neighbouring bands. 95% confidence intervals (CI) for centroids are estimated based on the weighted standard deviation and the t-distribution. Variations in window width across bands lead to variations in the spectral sample counts entering the analysis, and hence the width of the CI. Moreover, the Fourier Transform of the time-dependent autocorrelation sets the wavenumber resolution to be inversely proportional to the total propagation time T. Thus, even for a fixed band window, datasets obtained from larger T yield finer wavenumber resolution, more data points within that window, and correspondingly narrower CIs.

Additionally, the absolute band intensity is calculated through numerical integration as described in Section 4.2, where scaling factors with properly selected units adjust the final intensity to units of km/mol. Collectively, these calculations provide a detailed characterisation of the IR spectrum and critical insights into the fundamentals and overtones.

4.4.1 Fidelity Assessment Against References

We first evaluate the feasibility of our approach by comparing the simulated ZPE and characteristic fundamental bands against reference values derived from time-independent calculations. Coefficients used in constructing PES and DMS (see Eq. 4.2 and 4.4) of water are cited from [227], based on TZ + 2P basis sets at the SD-CI level of approximation. In contrast to the full Watson Hamiltonian exemplified in [226, 227], our simulations exclude the Watson U-term and Coriolis couplings in the Hamiltonian, primarily due to the computational inefficiency of incorporating these terms within the grid-based representation.

Following these considerations, we run a trial simulation starting from the ground state prepared via ITE, followed by applying dipole operators defined as Eq. 4.4, and then going through evolution of 300,000 time steps over a 19750 fs propagation window. To benchmark our time-dependent SO-QFT IR results, we assembled three sets of time-independent reference data. The first consists of Vibrational Configuration Interaction (VCI) band positions computed with PyVCI program [247] under our working Hamiltonian, with intensities calculated from VPT2. The second is constructed in the same manner but employs the full Watson Hamiltonian. The third set corresponds to vibrational Full Configuration Interaction (vFCI) results reported in [227], likewise derived with the full Watson Hamiltonian. The agreement between the latter two sets justifies the use of the first, obtained under our Hamiltonian, as a benchmark for assessing SO-QFT performance. As outlined in Table 4.4, our results exhibit excellent agreement with the VCI + VPT2 reference that also omits pseudo-potential and Coriolis terms, consequently validating the reliability of our time-dependent approach. Specifically, the deviations

in ZPE and band positions do not exceed 0.6 cm^{-1}, and the relative error in band intensities remains below 9.5%. Compared to the harmonic frequencies derived from the quadratic force field, the present anharmonic SO-QFT results exhibit a clear improvement in reproducing fundamental band positions.

	Our Hamiltonian		Full Hamiltonian	
	SO-QFT	VCI + VPT2	VCI + VPT2	vFCI
ZPE	4776.2	4776.5	4765.4	4765
Band Positions (cm^{-1})				
Mode 1	3809.0 ± 0.5	3808.4	3808.4	3808
Mode 2	1624.3 ± 0.2	1623.9	1637.6	1637
Mode 3	3876.2 ± 0.3	3875.6	3889.6	3889
Band Intensities (km/mol)				
Mode 1	4.7	4.3	4.5	4.7
Mode 2	78.4	76.9	76.7	76.8
Mode 3	39.4	36.6	36.9	39.9

Table 4.4: Comparison of ZPE and fundamental band positions and intensities simulated from this work (SO-QFT) against reference data. The VCI + VPT2 columns report variational band positions, obtained with PyVCI [247] using a harmonic-oscillator basis at excitation level VCI(10), and VPT2 intensities. The vFCI column lists the full vibrational CI results of Ref. [227], obtained with 10 harmonic-oscillator functions per mode.

4.4.2 Optimisation of Time Parameters

One important consideration in simulating IR spectra is the length of time evolution, which is expected to be sufficiently long to produce accurate band positions. This requirement stems from the fact that vibrational wavenumber resolutions rely on observing the full dynamic behaviour over adequate duration. A longer propagation period enables the simulation to capture subtle oscillatory components, which translates into well-defined wavenumber peaks in the IR spectrum. Additionally, a smaller time spacing size, dt, achieved by dividing T into a greater number of time steps n_t (with $T = n_t dt$), improves accuracy by reducing the Trotter error per step. Together, carefully chosen T and n_t ensure a high-quality simulation that captures fine time-dependent spectral dynamics.

T (fs)	n_t	dt (fs)	Mode 1		Mode 2		Mode 3	
			$\widetilde{\upsilon}_c$ (cm^{-1})	I_{IR} (km/mol)	$\widetilde{\upsilon}_c$ (cm^{-1})	I_{IR} (km/mol)	$\widetilde{\upsilon}_c$ (cm^{-1})	I_{IR} (km/mol)
Various total evolution time T, with a fixed time resolution dt:								
1975	30,000	0.066	3807.2 ± 17.7	4.7	1625.3 ± 4.1	80.0	3874.7 ± 9.5	38.9
3950	60,000	0.066	3809.1 ± 4.1	4.6	1625.1 ± 2.0	81.7	3876.2 ± 3.2	37.2
7900	120,000	0.066	3809.2 ± 0.9	4.6	1624.6 ± 0.9	79.2	3876.6 ± 0.8	38.9
13165	200,000	0.066	3808.9 ± 0.8	4.8	1624.2 ± 0.3	78.3	3876.6 ± 0.5	39.4
Various time resolution dt, with a fixed total evolution time T:								
3950	20,000	0.198	3814.8 ± 4.2	4.7	1627.2 ± 2.4	80.7	3882.2 ± 3.2	38.7
3950	40,000	0.099	3810.5 ± 4.3	4.7	1625.5 ± 1.6	80.7	3877.8 ± 3.3	37.9
3950	60,000	0.066	3809.1 ± 4.1	4.6	1625.1 ± 2.0	81.7	3876.2 ± 3.2	37.2
3950	80,000	0.049	3808.6 ± 4.0	4.6	1625.0 ± 2.2	81.7	3875.6 ± 3.3	37.7

Table 4.5: Fundamental bands simulated from various time parameters. Here $\widetilde{\upsilon}_c$ and I_{IR} represent the band position and absolute band intensity, respectively. All simulations start from a ground state prepared via ITE and utilise dipole operators defined as Eq. 4.4.

$\mu_{3\mathrm{rd}}\Psi_{\mathrm{ITE}}$			
$\widetilde{\upsilon}_c$ (cm^{-1})		I_{IR} (km/mol)	
T=3950 fs	T=13165 fs	T=3950 fs	T=13165 fs
3206.8 ± 6.5	3207.1 ± 3.3	0.67	0.67
4733.9 ± 16.2	4738.0 ± 8.1	0.046	0.047
5383.8 ± 6.0	5384.5 ± 2.2	0.13	0.13
5427.4 ± 3.2	5427.9 ± 0.8	8.2	8.2
6131.9 ± 14.9	6133.4 ± 6.7	0.038	0.038
6944.4 ± 14.4	6948.4 ± 7.3	0.14	0.14
7005.8 ± 17.1	7008.6 ± 4.7	0.021	0.015
7595.1 ± 6.1	7595.0 ± 2.6	0.48	0.48
7643.8 ± 4.7	7643.9 ± 1.9	2.1	2.1
7812.4 ± 37.9	7813.1 ± 4.8	0.016	0.019
8413.0 ± 15.3	8414.4 ± 5.8	0.037	0.038
8437.6 ± 37.9	8441.4 ± 4.4	0.018	0.016
/	9082.7 ± 4.4	/	0.012
/	9091.4 ± 4.9	/	0.0097
9111.3 ± 6.8	9112.1 ± 2.5	0.37	0.37
9826.8 ± 15.6	9828.8 ± 7.2	0.069	0.068
9869.0 ± 17.1	9870.6 ± 5.2	0.030	0.030
/	10532.0 ± 11.4	/	0.0067
/	10539.5 ± 4.5	/	0.013
/	10663.7 ± 4.5	/	0.013
/	11143.9 ± 5.1	/	0.010
11385.8 ± 14.6	11391.0 ± 5.6	0.051	0.054
11446.0 ± 11.6	11447.4 ± 5.2	0.12	0.12
11503.8 ± 13.7	11506.1 ± 5.1	0.057	0.056
11547.7 ± 12.4	11550.2 ± 5.6	0.11	0.11
/	11857.3 ± 11.3	/	0.0078
/	11912.9 ± 11.4	/	0.0073
11972.0 ± 17.0	11971.1 ± 5.2	0.037	0.037

Table 4.6: Overtones simulated using different total propagation time lengths and approximation schemes in $\mu\Psi$, with a fixed time step size $dt \approx 0.066$ fs. Here $\widetilde{\upsilon}_c$ and I_{IR} represent the band position and absolute band intensity, respectively. The simulations in this panel (a) start from a ground state prepared via ITE and utilise dipole operators truncated at third order, i.e., $\mu_{3\mathrm{rd}}\Psi_{\mathrm{ITE}}$. Panel (b) continues on the next page.

$\mu_{1st}\Psi_{Gauss}$			
$\widetilde{\upsilon}_c$ (cm^{-1})		I_{IR} (km/mol)	
T=3950 fs	T=13165 fs	T=3950 fs	T=13165 fs
3200.8 ± 17.6	3201.4 ± 9.3	0.076	0.078
4733.0 ± 10.6	4734.6 ± 5.4	0.10	0.10
5384.3 ± 3.0	5384.6 ± 0.7	3.9	4.0
5427.2 ± 8.2	5428.8 ± 3.5	0.26	0.26
6134.6 ± 9.0	6135.2 ± 4.0	0.10	0.10
6941.7 ± 15.4	6946.0 ± 7.9	0.12	0.12
7006.0 ± 16.8	7008.7 ± 4.5	0.021	0.015
7595.8 ± 4.4	7595.4 ± 1.7	1.2	1.2
7643.5 ± 3.8	7643.6 ± 1.2	6.0	6.0
7813.0 ± 37.5	7813.3 ± 4.1	0.022	0.025
8415.3 ± 15.2	8416.0 ± 5.5	0.046	0.045
8439.9 ± 30.6	8439.7 ± 1.8	0.16	0.15
/	9083.1 ± 4.1	/	0.014
/	9091.4 ± 5.1	/	0.0078
9112.2 ± 12.0	9114.4 ± 5.0	0.087	0.079
9826.8 ± 15.5	9828.8 ± 7.2	0.065	0.064
9869.6 ± 16.9	9871.0 ± 4.9	0.032	0.032
/	10532.4 ± 10.7	/	0.0088
/	10539.7 ± 3.2	/	0.035
/	10664.3 ± 3.2	/	0.026
/	11143.9 ± 5.0	/	0.0099
11388.6 ± 11.8	11391.5 ± 4.0	0.097	0.099
11447.7 ± 5.9	11447.9 ± 2.6	0.45	0.47
11503.8 ± 13.8	11506.1 ± 5.2	0.053	0.052
11545.6 ± 15.1	11549.3 ± 7.0	0.065	0.068
/	11857.6 ± 10.7	/	0.0099
/	11914.0 ± 5.6	/	0.045
11972.0 ± 16.2	11971.3 ± 4.9	0.038	0.038

Table 4.6: Overtones simulated using different total propagation time lengths and approximation schemes in $\mu\Psi$, with a fixed time step size $dt \approx 0.066$ fs. Here $\widetilde{\upsilon}_c$ and I_{IR} represent the band position and absolute band intensity, respectively. The simulations in this panel (b) start from an approximate Gaussian-product ground state and utilise dipole operators truncated at first order, i.e., $\mu_{1st}\Psi_{Gauss}$. (Continued from the previous page).

However, the gate depth of quantum circuits is proportional to the number of evolved time steps n_t as presented in Section 4.3.3. To ensure efficient implementation on real quantum computers, we then seek to find the optimal time settings that minimise circuit depths while maintaining high fidelity in characterising IR bands. By systematically altering the total simulated time with a constant time resolution, and varying the time resolution for a fixed simulation length, we identify the minimal T and n_t required to reproduce accurate fundamental and overtone band features.

Table 4.5 presents the sensitivity of band positions and absolute band intensities to variations in T and dt, respectively. We observe convergence behaviours of fundamental band positions as a function of the time parameters, stabilising with extended simulation durations or finer time resolutions. Among the various scenarios tested, we identify $T \approx 3950$ fs, discretised by 60,000 steps (i.e., $dt \approx 0.066$ fs), as an optimal setting that achieves quantitatively accurate band positions. While further increases in T or n_t enhance performance, the associated growth in resource demands makes such adjustments suboptimal for practical implementations. According to Section 4.3.3, with $n_t = 60,000$ time steps, the circuit depth of the time evolution section becomes 1.6×10^9 gates.

The time settings optimised for fundamental bands are subsequently extended to analyse overtone transitions, where convergence behaviours are also observed as time parameters improve (see data in the panel (a) of Table 4.6). Longer simulation time, such as $T \approx 13165$ fs, enables the identification of weaker overtone features, providing a more comprehensive depiction of the IR spectrum. While moderate time settings, such as $T \approx 3950$ fs, may miss certain weak overtone bands, they nonetheless capture the majority of significant transitions reported in [227].

4.4.3 Approximation Scheme Validation

Our framework is specifically tailored for compatibility with quantum computing paradigms, where we tend to leverage various approximations in the dipole operated ground state $\mu |\Psi\rangle$ to minimise quantum resource requirements without sacrificing the fidelity. In particular, approximations are introduced in two key areas: the

construction of the dipole operator and the representation of the ground state. For the dipole operator, we evaluate both a first-order truncated form and a more sophisticated third-order version (Eq. 4.4) that enables access to more complex dynamics. Similarly, for the ground state, we compare the simple Gaussian distribution Ψ_{Gauss}, with a more advanced representation Ψ_{ITE} derived from ITE. These choices of $\mu\,|\Psi\rangle$ with varying circuit complexity result in four datasets for comparison, all of which are systematically examined via classical emulation to assess their respective implications. Across all configurations, the potential energy terms governing time evolution retain a fourth-order force field.

As illustrated in Table 4.7, we compare all four exact or approximate representations of $\mu\,|\Psi\rangle$, in terms of their influence on simulated fundamental band positions and intensities. Our data reveal that simplifying the dipole operator from μ_{3rd} to μ_{1st}, or approximating the initial state Ψ_{ITE} with Ψ_{Gauss}, has negligible impacts on fundamental band positions. Importantly, this level of consistency persists across a range of time parameters, as confirmed by the complete datasets for different total evolution times (Table A.2 in Appendix A) and time resolutions (Table A.3 in Appendix A).

While band positions show remarkable robustness to changes in approximation schemes, band intensities are slightly more sensitive to these approximations, as evidenced by small but quantifiable deviations - well below the precision limit relevant for routine applications. The intensity variations do not exhibit a strictly monotonic dependence on the level of approximation. This behaviour arises because the dipole truncation and the ground-state approximation affect different components of the transition amplitude, such that their respective errors may partially cancel or reinforce each other, rather than producing a simple cumulative deviation. Notably, the most cost-effective $\mu_{\text{1st}}\Psi_{\text{Gauss}}$ produces intensities that deviate by no more than 2.2%, 7.5%, and 1.1% for Modes 1, 2, and 3, respectively, when compared to those obtained from the most computationally demanding $\mu_{\text{3rd}}\Psi_{\text{ITE}}$. The reported band positions and intensities collectively verify the viability

$\mu\,\lvert\Psi\rangle$	Mode 1		Mode 2		Mode 3	
	$\widetilde{\nu}_c$ (cm^{-1})	I_{IR} (km/mol)	$\widetilde{\nu}_c$ (cm^{-1})	I_{IR} (km/mol)	$\widetilde{\nu}_c$ (cm^{-1})	I_{IR} (km/mol)
$\mu_{3\mathrm{rd}}\Psi_{\mathrm{ITE}}$	3809.1 ± 4.1	4.6	1625.1 ± 2.0	81.7	3876.2 ± 3.2	37.2
$\mu_{1\mathrm{st}}\Psi_{\mathrm{ITE}}$	3809.1 ± 4.0	5.8	1625.1 ± 2.0	80.6	3876.2 ± 3.2	41.1
$\mu_{3\mathrm{rd}}\Psi_{\mathrm{Gauss}}$	3809.1 ± 4.1	4.4	1625.1 ± 2.0	77.2	3876.2 ± 3.2	34.7
$\mu_{1\mathrm{st}}\Psi_{\mathrm{Gauss}}$	3809.1 ± 4.0	4.7	1625.1 ± 2.0	75.6	3876.2 ± 3.2	36.8

Table 4.7: Fundamental band positions and intensities simulated under various approximation schemes adopted for $\mu\,|\Psi\rangle$. Here $\widetilde{\nu}_c$ and I_{IR} represent the band position and absolute band intensity, respectively. All simulation start from a ground state prepared via ITE, followed by the application of dipole operators defined as Eq. 4.4, and then goes through time evolution under 60,000 steps discretised within 3950 fs.

of using approximated $\mu\Psi$ states to achieve a meaningful reduction in computational cost without compromising the overall reliability in fundamental band predictions.

Overtone bands, similar to fundamentals, also exhibit good adaptability to the approximations in $\mu\,|\Psi\rangle$. We list out the results in Table 4.6 for the fully detailed $\mu_{\mathrm{3rd}}\Psi_{\mathrm{ITE}}$ state (panel (a)) and the most streamlined $\mu_{\mathrm{1st}}\Psi_{\mathrm{Gauss}}$ state (panel (b)), while the two intermediate approximations, $\mu_{\mathrm{1st}}\Psi_{\mathrm{ITE}}$ and $\mu_{\mathrm{3rd}}\Psi_{\mathrm{Gauss}}$, are reported in Table A.4 of the Appendix A. Even the most cost-saving $\mu_{\mathrm{1st}}\Psi_{\mathrm{Gauss}}$ scheme still recovers those overtones identified in [227]. Across all four approximation levels, and under different choices of total evolution time, the deviations in band positions remain within scientifically reasonable ranges, regardless of whether the dipole, the ground state, or both are approximated. However, the overtone intensities are sensitive to the truncation and are therefore not quantitatively reliable without including beyond-linear dipole contributions. Accordingly, when focusing on band positions and qualitative overtone structure we employ the $\mu_{\mathrm{1st}}\Psi_{\mathrm{Gauss}}$ scheme to limit circuit cost; when quantitative overtone intensities are required, a more accurate scheme of $\mu\,|\Psi\rangle$ should be adopted.

Fundamental bands indeed play a central role in characterising IR spectra, as they provide direct information about molecular vibrations and are typically the most intense features observed. While overtones and combination bands contribute additionally to the spectral profile, the calculation of their intensities is generally less significant for conventional IR characterisation. Consequently, our analysis indicates that the approximated $\mu_{\mathrm{1st}}\Psi_{\mathrm{Gauss}}$ state is sufficiently effective for uncovering essential spectral features.

4.5 Conclusions

In this work, we develop and evaluate a time-dependent wavefunction-based methodology for simulating infrared spectra, accompanied by the design of a corresponding quantum circuit framework tailored for future quantum implementation. The workflow integrates the application of the dipole operator to the vibrational ground state in a grid-based representation, followed by time evolution under a suitably

selected Hamiltonian. The dipole-dipole autocorrelation is computed at each time step and subsequently subjected to Fourier transformation which generates the final IR spectrum. Band positions and intensities are extracted through centroid and numerical integration analysis over the simulated spectrum, which deliver excellent agreement with time-independent references when using water molecule as a model system.

While the present implementation demonstrates accurate infrared spectra for the water molecule, it should be acknowledged that this system is essentially a solved problem, with classical variational calculations already reproducing its rovibrational features to near-spectroscopic accuracy [248]. The water model thus serves primarily as a benchmark for validating the proposed simulation framework. The principal merit of our quantum approach lies in its scalability to larger and more flexible molecular systems, where classical treatments become computationally prohibitive beyond a few degrees of freedom.

The quantum implementation of our approach is carefully structured to optimise resource overhead. A series of uniformly controlled rotations first gives an efficient preparation of the initial Gaussian state. For the application of the dipole function, we employ a probabilistic circuit design incorporating an ancillary qubit to handle the non-unitary nature of this operator. The time evolution is carried out using the structure-optimised SO-QFT scheme, which capitalises on the inherent efficiency of QFT. We present circuits that manage the exponentiation of Hamiltonian terms across various polynomial orders with associated gate depth evaluations. The extraction of the dipole-dipole autocorrelation is facilitated by two variations of the Hadamard test, which relies on repeated measurements of another ancillary qubit. Together, these elements form a coherent framework for implementing our approach on real quantum devices.

Within this framework, the required qubit resources grow linearly with the number of vibrational modes. For the specific water model, this translates to overall 15 qubits (4 qubits for each of the 3 normal mode register, 2 ancillary qubits for the decomposition of multi-controlled gates, 1 ancillary qubit for the Hadamard test).

The circuit depth of state preparation remains independent of the total number of modes, while the time evolution scales polynomially with the qubit count per mode and linearly with both the number of modes and the number of propagation time steps: $\mathcal{O}(dn^4 n_t)$. Here the linear dependence on the mode count arises from the global ancilla control required in the Hadamard-test measurement.

Efforts to optimise our algorithm focus on minimising the total circuit depth, from either the aspect of optimal time parameters or cost-effective approximation schemes in the dipole operated ground state. We first systematically investigate the influence of different time settings on the accuracy of the calculated water IR spectra. Our results reveal a convergence behaviour in the band positions as the total simulation time is extended and the time resolution becomes finer. Through this analysis, we identify an optimal configuration of 60,000 time steps across a total time of 3950 fs. Although longer simulation time, such as 13165 fs, captures more weak overtone features, 3950 fs is sufficient for interpreting all fundamental bands and the most significant overtones in water.

We then explore how approximating either the initial ground state or the dipole operator affects the band characterisation. These approximations introduce minimal deviations in fundamental and overtone band positions, demonstrating their suitability for practical routine use. Although the impact on overtone intensities is evident, the intensities of fundamental bands remain largely unaffected by these approximations, which ensures the overall fidelity of the spectra. As IR spectroscopy primarily emphasises fundamental bands (with overtones often playing a supplementary role), we conclude that the most cost-saving $\mu_{1\text{st}} |\Psi_{\text{Gauss}}\rangle$ scheme strikes an appropriate balance between circuit efficiency and spectral accuracy. The corresponding circuit depth including both the state preparation and the time evolution over 60,000 times steps is 1.6×10^9 gates.

As the grid-based representation and SO-QFT methodology are particularly well-suited for quantum computing, the significance of this work emerges for its great integration with future quantum computers. Our time-dependent grid-based approach not only achieves sufficient fidelity and reliability in simulating IR spectra

but also demonstrates direct compatibility required for implementation on quantum hardware. By validating the use of harmonic oscillator approximations for ground state preparation and truncated dipole functions, we effectively minimise the gate depth required.

Outlook.

Unlike the vibronic simulations in Chapter 3, the present infrared study does not include a statistical measurement analysis. In particular, the probabilistic encoding of the non-unitary dipole operator introduces additional sampling overhead beyond that of a fully unitary SO-QFT implementation. The required number of measurement repetitions depends not only on the desired spectral precision, but also on the success probability of the block-encoded operation. A systematic assessment of these measurement costs, together with the investigation of mitigation strategies such as amplitude amplification or alternative high-success block-encoding techniques, constitutes an important direction for future work.

The inherent strengths of quantum devices in handling high-dimensional problems unlock a new pathway for calculating IR spectra of complex molecules. Future work may therefore build upon the present framework to incorporate floppy molecules exhibiting torsional or large-amplitude motions. For such systems, the main challenge will shift toward constructing and encoding accurate potential energy surfaces. The overall framework, however, would remain applicable, though the torsional angle would require curvilinear coordinates and the potential energy surface needs to be appropriately expanded or tabulated.

5

Coulombic Simulations with Singular Potential Challenges

Contents

5.1 Introduction

Simulating quantum dynamics under Coulombic interactions represents one of the most well-understood yet challenging problems in quantum chemistry. Despite their conceptual simplicity under the Born-Oppenheimer approximation, simulations of hydrogenic systems allow insights into processes that are otherwise inaccessible due to experimental constraints, whether from extreme conditions or transient lifetimes [249]. They also set a foundation for tackling more complex molecular and condensed-phase phenomena. In this context, the importance of real-time simulations become particularly important, as Coulomb singularities and long-range interactions under strong or time-varying fields critically govern processes such as ionisation, rescattering and high-harmonic generation [250, 251].

A wide range of simulation techniques for Coulombic systems on classical computers have been developed and studied in depth over the years [252–258]. Grid-based approaches [259–265], such as finite difference or discrete variable representations, directly discretise the spatial domain but tend to suffer from errors due to the singular behaviour of the Coulomb potential, $-1/r$, near the nucleus. Spectral methods that employ tailored orthogonal polynomial bases [266–268] can more accurately capture bound state features; however, they introduce artificial boundary conditions that distort continuum states. Path integral techniques [269–271] use imaginary-time propagation to handle singular potentials, yet this comes at the cost of resolving real-time dynamics. Quantum trajectory theory [272–274] proceeds wavepacket evolution via stochastic averaging, but fails to resolve multi-body quantum correlations governing electron-nuclear cusp conditions.

As quantum computers mature, we anticipate that nuclei and electrons, interacting directly via electrostatic forces, can in principle be both simulated on a quantum computer with ease [75]. Recent advances in quantum computing have prompted a reexamination and advancements of classical simulation strategies. Several quantum approaches, such as the Trotter-based expansion of unitary operators for time evolution [275–278], hybrid quantum-classical Variational Quantum Algorithms [279, 280], e.g. the Variational Quantum Eigensolver [91, 92, 281] whether through

Hardware-Efficient Ansatz of Unitary Coupled Cluster [93, 282] or Adaptive Derivative-Assembled Pseudo-Trotter ansatz [283], and techniques like the quantum machine learning [284] have been extensively explored for Coulombic systems.

In this chapter, quantum dynamics under the Coulomb potential is simulated under the grid-based discretisation, where the spatially continuous potential and wavefunction are represented by their values on discrete grid points. As either attractive or repulsive Coulomb potential is centered at the origin, the singularity at $x = 0$ poses numerical difficulties. To prevent divergence, the grid is defined to avoid including this point explicitly. This exclusion, along with the sparse nature of grid-based discretisation, introduces artifacts in ground-state energies and time evolution fidelity. Denser grids mitigate this issue but at the expense of increased computational resources.

We therefore develop an optimised SO-QFT framework that incorporates pre-encoded corrections into both the initial wavefunction and the potential operator, to suppress discretisation artifacts in hydrogenic simulations. These efforts are designed to address the systematic inaccuracies caused by oversimplifying Coulomb-related terms in grid-based representations. Our study not only improves classical simulation fidelity with moderate grid sizes, but also proposes gate-efficient mappings of the correction schemes essential for adaptation to fault-tolerant quantum hardware.

This chapter is organised as follows. Section 5.2 details the systems and observables that we focus on. Section 5.3 introduces the correction schemes employed to better accommodate hydrogenic dynamics. Section 5.4 presents classical emulation results to illustrate the efficacy of these corrections. Section 5.5 outlines the corresponding quantum circuit architectures, along with an analysis of their quantum resource demands.

5.2 Systems and Observables

5.2.1 Systems of Interest

Our analyses focus on two model systems characterised by Coulombic interactions. The first is the two-dimensional hydrogen system [285], where the nucleus is treated

as a fixed Coulombic center and the electron is described by a ground-state quantum wavepacket

$$\Psi_{\text{hydrogen}} = Ce^{-2\mathbf{r}}, \tag{5.1}$$

and the 2D Hamiltonian

$$H_{\text{hydrogen}} = \underbrace{-\frac{1}{2}\frac{\partial^2}{\partial x^2} - \frac{1}{2}\frac{\partial^2}{\partial y^2}}_{K} + \underbrace{\frac{1}{\mathbf{r}}}_{V}, \tag{5.2}$$

leading to an analytical energy of -2 a.u.. Here $\mathbf{r} = \sqrt{x^2 + y^2}$ and C incorporates all constant factors in the wavefunction. The simulation box, discretised along two spatial dimensions (each 10 a.u. in length), determines the resolution of the electron's position, with higher grid density yielding finer spatial details. The second system involves two interacting electrons confined on a one-dimensional ring with the radius of $R = 1/2$ and the analytical energy of 2.25 a.u. [286]. Here, both the wavefunction,

$$\Psi_{2\text{e}} = \mathbf{u}(1 + \frac{\mathbf{u}}{2R})^{1/2}, \tag{5.3}$$

and the Hamiltonian

$$H_{2e} = \underbrace{-\frac{1}{R^2}\frac{\partial^2}{\partial \omega^2}}_{K} + \underbrace{\frac{1}{\mathbf{u}}}_{V}, \tag{5.4}$$

with $\mathbf{u} = R\sqrt{2 - 2\cos\omega}$, depend on the angular separation ω between electrons, which is defined as the intracule angle coordinate spanning $[0, 2\pi]$. This angular variable is discretised to control the spatial resolution. For consistency, all simulations are conducted in atomic units.

5.2.2 Extraction of Observables

Within the SO-QFT framework, the total evolution time is discretised into finite steps. We monitor two key observables during time evolution: the dynamic ground-state energy and the evolution fidelity. Both are derived from the time-dependent autocorrelation function,

$$A(t) = \langle \Psi(0) | \Psi(t) \rangle = e^{-iE_{\text{dynamic}}t}. \tag{5.5}$$

The cosine periodicity of its real component, $\cos(E_{\text{dynamic}}t)$, enables retrieval of this time-averaged numerical energy, E_{dynamic}, which reflects the energy scale governing long-time dynamics and serves as a robust indicator for algorithmic accuracy. Under a perfect simulation, E_{dynamic} is expected to be the exact analytical ground-state energy. Fidelity, on the other hand, is evaluated by the absolute value of the autocorrelation function. For systems initiated in eigenstates of the Hamiltonian, this modulus should ideally remain unity throughout time evolution:

$$|A(t)| = |\langle\Psi(0)|\Psi(t)\rangle| = 1.$$

Any deviation indicates fidelity loss and thus provides a quantitative measure of temporal coherence in the simulated dynamics.

5.3 Correction Schemes

We now outline the two correction strategies designed to mitigate numerical errors arising from coarse discretisations, particularly those related to singular Coulombic potentials and imperfect ground state encoding.

In conventional grid-based simulations, potentials are applied pointwise on a discretised spatial grid, implicitly assuming each basis function as a Dirac delta function. While a small number of simulation grid points suffice for smooth fields e.g. quadratic potentials, the inability to resolve the singularities near their origins introduce errors when representing dynamics with e.g. the Coulomb interaction, particularly under a limited grid resolution. The immediate assumption that a higher spatial resolution via an increased grid density leads to improved accuracy is widely held. Yet, this direct scaling of resolution, while conceptually straightforward, exhibits intensive computational burden for large systems. This trade-off becomes problematic in scenarios necessitating prolonged time propagation, rendering it less than ideal for practical applications.

To address this, we propose a correction scheme in which the Coulomb potential is re-evaluated by computing the expectation value of the original Coulomb potential within the actual pixel function $\phi_k(x)$ (see definitions in Chapter 2). At finite grid

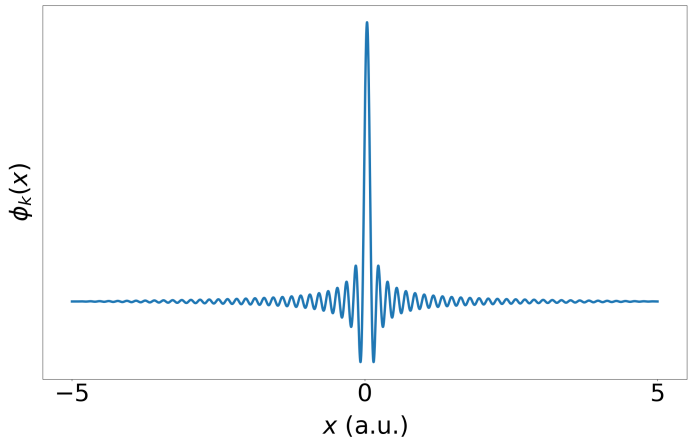

Figure 5.1: Representative one-dimensional pixel function $\phi_k(x)$ on a finite grid.

size, each $\phi_k(x)$ deviates from an ideal Dirac delta function and instead possesses a non-zero spatial extent with oscillatory side lobes, as shown in Figure 5.1. We now specifically define a corrected potential

$$\begin{aligned} V_{\text{corrected}} &= \langle \phi_i(x) | V | \phi_k(x) \rangle \text{ (in 1D)}, \\ &= \langle \phi_i(x)\phi_j(y) | V | \phi_l(y)\phi_k(x) \rangle \text{ (in 2D)}, \\ &= \cdots \end{aligned} \tag{5.6}$$

which accounts for the spatial extent and shape of the localised pixel functions and more accurately reflects the singular potential's influence over the local region. The matrix elements are evaluated numerically on an auxiliary grid with $N_{\text{correction}}$ points per dimension, which is independent of the simulation grid $N_{\text{simulation}}$. This correction grid serves purely as a quadrature tool and does not modify the Hilbert space dimension of the subsequent time-dependent simulation. For computational convenience of this work, we have limited our consideration to contributions arising solely from the diagonal elements, where $i = k$ and $j = l$. This correction can be physically interpreted as recognising that the electron is not localised at an infinitesimal point x_k, but is represented by a finite-width wavepacket defined by the grid basis function $\phi_k(x)$. The corrected potential therefore corresponds to the basis-averaged Coulomb interaction experienced by this spatially extended state.

The new set of potential values, $V_{\text{corrected}}$, is used during simulation in place of the naive point-sampling potential. Although the simulation itself still runs

on the original coarse grid $N_{\text{simulation}}$, using a denser auxiliary $N_{\text{correction}}$ for the numerical calculation of $V_{\text{corrected}}$ yields significant performance improvements in both the ground-state energy integrity throughout time-dependent dynamics and the evolution fidelity as a function of time (see Section 5.4.1). This correction leverages higher-resolution information in the preprocessing stage while keeping the computational complexity of the main simulation unchanged.

A useful comparison may be drawn with the augmented split-operator (ASO) approach introduced by [69], in which a unitary augmentation is derived to repair discrepancies between the exact and split-operator propagators within a selected core subspace. While ASO can yield substantial fidelity improvements, its derivation is non-trivial and requires additional circuit execution at every Trotter step. By contrast, the proposed potential correction only involves a one-off numerical quadrature to modify the discretised potential operator, leaving the SO-QFT structure and per-step gate complexity unchanged. The two approaches therefore target different sources of errors: ASO mitigates propagator-level inaccuracies, whereas our correction reduces errors arising from the discretisation of the singular potential.

Another challenge in grid-based simulations involving Coulomb systems lies in representing their true wavefunctions. In low-resolution grids, the exact eigenfunctions of such Hamiltonians cannot be captured faithfully, leading to instability and degradation of time fidelity. Inspired by prior analytical solutions of hydrogenic systems derived from softened Coulomb potentials [287], we adopt

$$\Psi_{\text{corrected}} = C\mathbf{r}^{\frac{Z}{\alpha}-b}e^{-\alpha\mathbf{r}}, \tag{5.7}$$

with $b = 0, -\frac{1}{2}, -1$ for 1D, 2D and 3D hydrogenic models, as a corrected wavefunction to reduce the numerical mismatch between the initial state and the grid-based Hamiltonian. In this formulation, all constant coefficients are absorbed into the prefactor C. Since E_{dynamic} varies with the grid density employed in the numerical simulation, the parameter $\alpha = \sqrt{-2E_{\text{dynamic}}}$ must be uniquely calculated for each specific grid density. Thus, by running a preliminary trial simulation at the chosen

spatial resolution, one can determine E_{dynamic}, calculate the corresponding α, and subsequently derive the corrected wavefunction $\Psi_{\text{corrected}}$.

Our results (see Section 5.4.2) on the 2D hydrogen system confirm that initialising the simulation with this corrected wavefunction yields extremely high time fidelity, validating its effectiveness. As $\Psi_{\text{corrected}}$ more closely approximates the true physical state in grid-based space, this correction scheme enables stable time-dependent studies without requiring prohibitively dense grid resolutions.

While demonstrated here for hydrogenic systems, the strategy of modifying initial wavefunctions holds potential for broader applications beyond the current context. For other Coulombic systems where analytical eigenfunctions of analogous softened potential approximations are available, similar corrections can be deduced. This offers a systematic means to enhance simulation reliability and without resorting to impractical grid refinements, thus broadening the applicability of grid-based quantum dynamics methods.

An alternative strategy is to obtain the discretised ground state directly via Imaginary Time Evolution (ITE). In a broad sense, both ITE and the present wavefunction correction aim to identify the state corresponding to a given Hamiltonian on a chosen grid. However, ITE is fundamentally a numerical eigenstate projection method, yielding a finite-dimensional vector representation of the state. By contrast, the correction proposed here provides a structure-preserving, analytically parameterised ansatz that retains explicit functional form and can therefore be systematically generalised in a controlled manner.

From a quantum algorithmic perspective, ITE requires non-unitary evolution and hence necessitates additional techniques for implementation on quantum hardware. The present correction, however, relies solely on real-time unitary evolution to extract the dynamical energy required for constructing the corrected wavefunction, making it well suited to quantum architectures.

It should be emphasised that if the Hamiltonian itself suffers from discretisation errors, ITE will faithfully return the ground state of that imperfect operator. Improvements in dynamical energies therefore require prior refinement of the

Hamiltonian, such as through potential correction, after which ITE may be applied to the corrected operator.

5.4 Performance of Corrections

We first assess the general characteristics of the SO-QFT scheme in systems featuring singular Coulombic potentials – which we will reference as the uncorrected benchmark. All simulations in this work are conducted under a sufficiently high time resolution, e.g., 30,000 steps ($dt = 0.0002$ a.u.) for the 1D two-electron ring and 6,000 steps ($dt = 0.001$ a.u.) for the 2D hydrogen system over a total duration of 6 a.u., to minimise the impact of time discretisation and enabling a focused evaluation of spatial resolution effects.

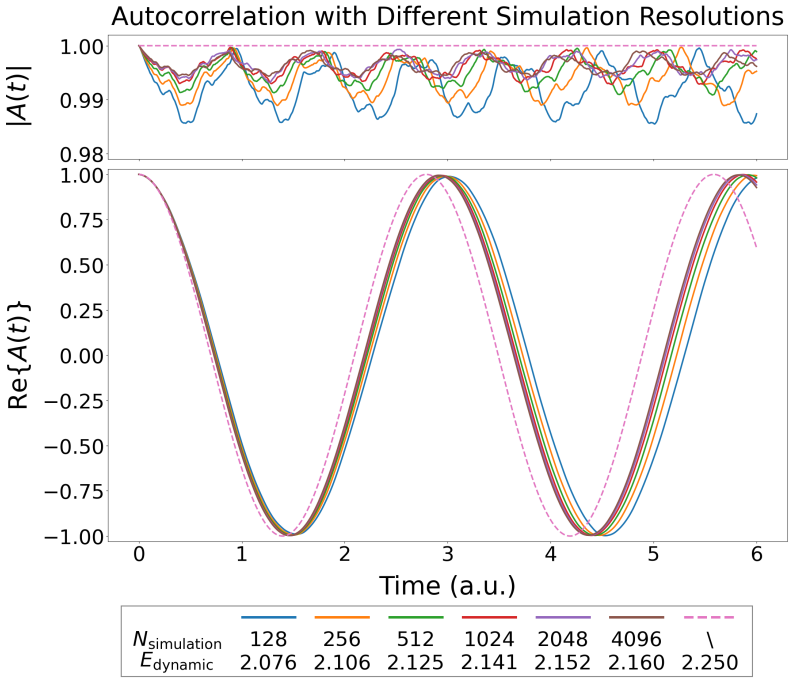

Figure 5.2: Absolute value and real part of autocorrelation functions recorded from simulating the 1D electron-electron quantum ring with different $N_{\text{simulation}}$. Analytical profiles are plotted with dashed linestyle.

As a representative case, we herein present results of the 1D two-electron quantum ring. Figure 5.2 illustrates that, in the absence of correction, the numerical ground-state energies extracted from $\mathbb{R}\text{e}\{A(t)\}$ gradually converge to the known analytical value and the $|A(t)|$ curves reflecting time fidelity present deviates less from unity, as

the spatial resolution increases (i.e., the number of grid points $N_{\text{simulation}}$ increases within the fixed angular domain $[0, 2\pi]$). As expected, increasing grid density improves energy estimate and time fidelity, but incurs a steep computational cost in terms of memory and gate complexity, posing a practical limitation on such a brute-force approach. This motivates the use of correction schemes that can suppress errors even for coarse grid settings.

We therefore evaluate the efficacy of our two correction schemes in improving overall simulation quality, still using two complementary indicators: The numerical ground-state energy E_{dynamic} for algorithmic accuracy and the modulus of the autocorrelation for fidelity retention over time.

5.4.1 Corrections on Potential Operator

Diagonal corrections on the potential operator decouple the grid density used for physical propagation from that used for numerical calculation of the basis-integrated $V_{\text{corrected}}$. We run simulations under $V_{\text{corrected}}$ with the same simulation grid size $N_{\text{simulation}}$ per dimension (as above) but vary the number of auxiliary correction grids $N_{\text{correction}}$, as shown in Figure 5.3.

Compared to uncorrected benchmarks, these numerical results confirm that simulations using $V_{\text{corrected}}$ display improved agreement with analytical energies and show enhanced time fidelity for both the 1D two-electron quantum ring and the 2D hydrogen systems. This behaviour is rationalised by the fact that the corrected potential captures more of the singular feature of the Coulomb interaction that would otherwise be missed in such low-resolution simulations.

In addition, as the density of the quadrature grid $N_{\text{correction}}$ increases, both the extracted E_{dynamic} and $|A(t)|$ exhibit improvements. By resolving more of the pixel function's structure in the correction step, we achieve better modeling of the potential landscape. Technically, we only need to calculate $V_{\text{corrected}}$ once and the computational cost involved will not be escalated during long-time propagation.

As each entry in $V_{\text{corrected}}$ is computed by integrating over $N_{\text{correction}}^{d}$ grid points for d-dimensional systems, the major limitation lies in the exponentially increasing cost

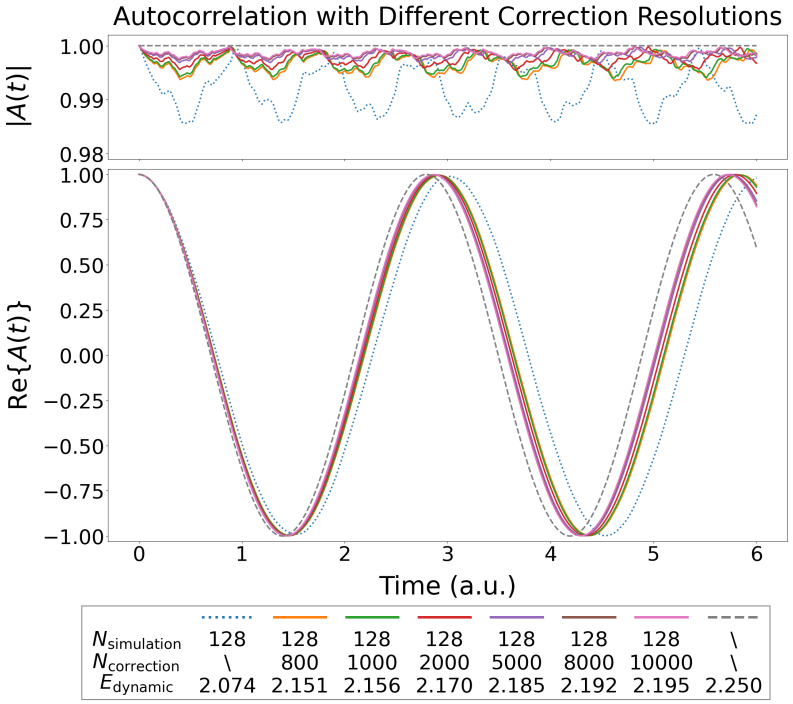

(a) Autocorrelation for the 1D two electron quantum ring

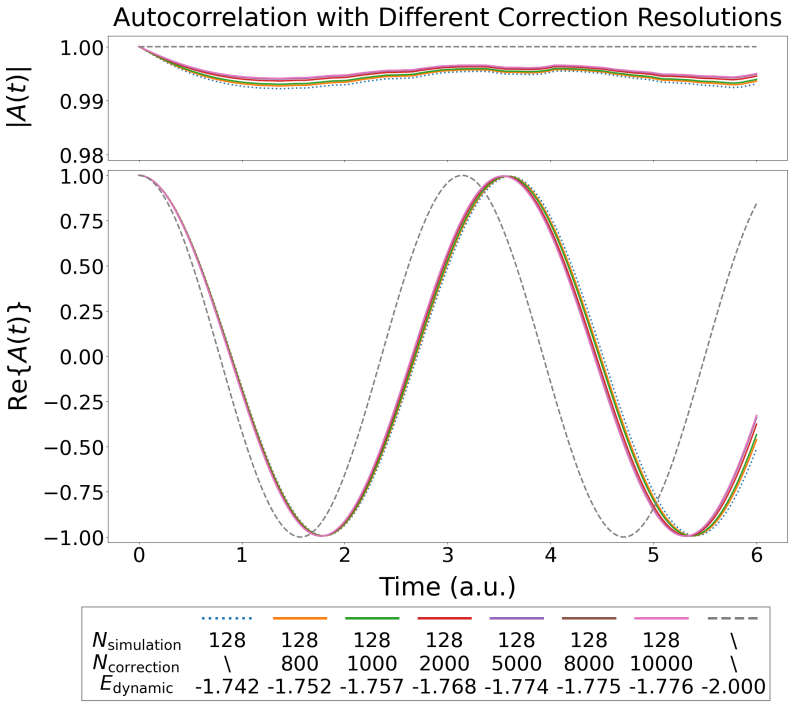

(b) Autocorrelation for the 2D hydrogen

Figure 5.3: Absolute value and real part of autocorrelation functions recorded from simulations of (a) the 1D electron-electron quantum ring and (b) the 2D nucleus-electron hydrogen using $V_{\text{corrected}}$ computed from different $N_{\text{correction}}$. For both panels, $N_{\text{simulation}}$ is fixed at 128 per dimension. Analytical profiles and results from uncorrected runs are plotted with dashed and dotted linestyles, respectively.

with system dimensionality. To make this step more scalable, we explore a piecewise non-uniform grid that concentrates points near the origin (where singularities occur), and allocates coarser spacing elsewhere.

As seen in Table 5.1, the energy values simulated using the non-uniform grid are close to those using much more uniform grids, provided the central resolution is comparable. The key insight is that the dominant contributions to the potential correction arise near the singularity, justifying the use of non-uniform strategy for higher-dimensional calculations to avoid the overhead of uniformly dense grids.

Central Spacing	$N_{\text{correction}}$ within $[-5, 5]$		E_{dynamic}
0.002	Non-Uniform	1800	-1.775
	Uniform	5000	-1.774
0.001	Non-Uniform	2800	-1.777
	Uniform	10000	-1.776

Table 5.1: Simulated E_{dynamic} of the 2D hydrogen system using uniform and non-uniform grid allocations in $V_{\text{corrected}}$ calculation. In the non-uniform cases, $N_{\text{correction}} = 1800$ and 2800 represent that 1000 and 2000 grid points are assigned within the central region, $[-1, 1]$ a.u., respectively, while the outer tails ($[1, 5]$ a.u. and $[-5, -1]$ a.u.) are allocated with 800 grid points.

5.4.2 Corrections on Initial Wavefunction

We then evaluate the impact of wavefunction correction on time propagation fidelity. In Figure 5.4, simulations initialised with corrected wavefunctions demonstrate near-perfect time fidelity. Although the deviations of the uncorrected $|A(t)|$ from unity appear small within the short time window shown, they indicate a residual excited-state admixture in the initial condition. Such contamination constitutes a coherent, systematic error that persists throughout the time evolution and may accumulate over extended propagation times. The present correction provides a controlled means of eliminating this mismatch at negligible additional cost. Across spatial grids of varying resolution examined ($N_{\text{simulation}} = 64, 128, 256$), the corrected cases keep tightly aligned with the ideal $|A(t)| = 1$ benchmark, in stark contrast to the visible deviations seen in the uncorrected runs. This indicates that the

correction effectively recovers eigenstate-like stability and the benefit extends to various $N_{\text{simulation}}$, confirming the robustness of utilising corrected initial states for maintaining high time fidelity even in coarse grids.

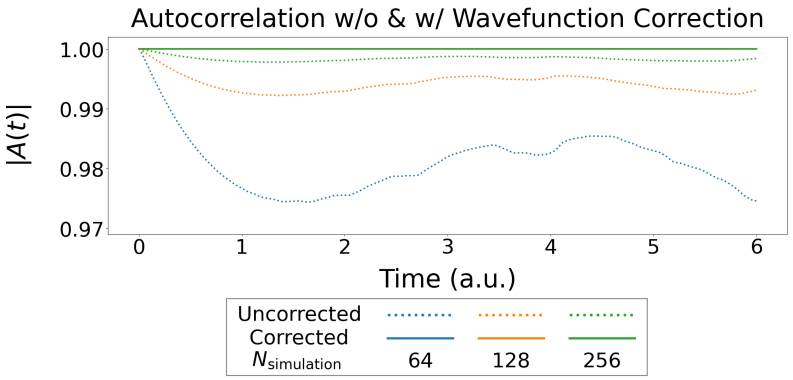

Figure 5.4: Absolute value of autocorrelation functions recorded from 2D hydrogen simulations initialised with uncorrected and corrected wavefunctions across different $N_{\text{simulation}}$.

The results above were obtained without applying the potential correction. The performance of wavefunction correction is independent of whether the potential correction is employed, as in each case the corrected state is constructed from the corresponding E_{dynamic} of the specified Hamiltonian and grid. The real part of the autocorrelation is not shown here because the wavefunction correction does not alter E_{dynamic} and therefore leaves the oscillation period of $\text{Re}(A(t))$ unchanged.

While the potential correction optimises E_{dynamic} and the wavefunction correction preserves time fidelity, we have examined that they together produce synergistic improvements. In simulations of the 2D hydrogen that simultaneously applies both corrections, the absolute autocorrelation remains ideal behaviour throughout and the numerical energy E_{dynamic} fully exhibit the benefit of the corrected potential. This dual-correction strategy is particularly suited for systems where increasing $N_{\text{simulation}}$ is computationally expensive, as it enables better-quality simulations than uncorrected baselines when holding the grid density unchanged.

5.5 Quantum Implementation

With the rapid progress in quantum computing, simulations of real-space Coulombic systems are expected to become significantly more tractable and efficient once practical quantum simulators are available [288]. We therefore seek to investigate the efficient realisation of our algorithm on quantum computers. The key properties of interest in this work, E_{dynamic} and time fidelity, are both derived from the time-dependent autocorrelation function. As the extraction of this function relies on repeated measurements via Hadamard test, the total measurement count serves as one of the metrics when assessing quantum resources. This cost can be reduced by employing a sparser sampling strategy, i.e., measuring the ancilla at selected time points with wider intervals, provided the resulting autocorrelation remains sufficiently smooth to resolve the desired properties.

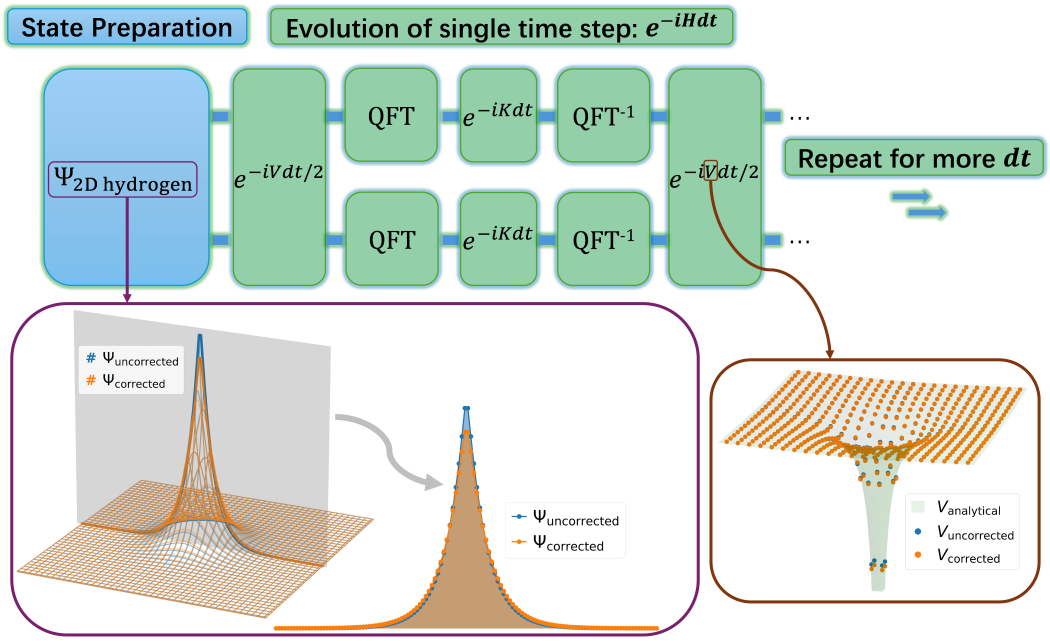

Figure 5.5: Schematic overview of essential components for simulating the 2D hydrogen system.

Another essential factor in resource evaluation is the circuit depth, which depends on the specific structure of the quantum circuits. In addition to autocorrelation measurements, the complete circuit also involves initial state preparation and time propagation stages. For these two stages, we have proposed and analysed two

targeted correction schemes in previous sections, both of which are compatible with quantum architectures. In the remainder of this section, we focus on the 2D hydrogen system as an illustrative example to detail the application of these correction schemes on realistic quantum hardware, along with an analysis of the associated gate depths and resource implications for constructing the circuit shown in Figure 5.5.

5.5.1 Preparation of Corrected Wavefunction

This section describes the quantum circuit construction for encoding the corrected wavefunction onto a register that represents a two-dimensional spatial space. We allocate $n = \log_2 N_{\text{simulation}}$ qubits per spatial dimension to represent a 2D $N_{\text{simulation}} \times N_{\text{simulation}}$ grid. The resulting quantum register consists of two n-qubit sub-registers, initialised in the state $|0\rangle^{\otimes 2n}$. The goal is to transform this initial state into a superposition state that reflects the amplitudes of the corrected wavefunction, i.e.,

$$\sum_{j_1=0}^{2^n-1} \sum_{j_2=0}^{2^n-1} c_{j_1 j_2} |j_1\rangle \otimes |j_2\rangle ,$$

where the coefficients $c_{j_1 j_2}$ denote the discretised amplitudes. Each basis state $|j_1\rangle \otimes |j_2\rangle$ corresponds to a specific grid point within the 2D space.

One straightforward approach for preparing this quantum state is to treat the two spatial dimensions as a single index and load the 2^{2n} amplitudes directly onto a $2n$-qubit register. This can be implemented by a cascade of uniformly-controlled rotations [178] requiring a gate count of $2^{2n+1} - 3$, where only two-qubit **CNOT** gates and single-qubit $\mathbf{R_y}$ gates are used due to the real and non-negative nature of the amplitudes. For $n = \log_2 128 = 7$, the total gate count is estimated to be 32,765.

To reduce the gate depth and improve efficiency, we alternatively adopt the Fourier Series Loader (FSL) method [180], which constructs the multidimensional quantum state from truncated Fourier series representations. Instead of loading all 2^{2n} amplitudes directly, only 2^{2l} Fourier coefficients with $l < n$ are used to approximate the full wavefunction.

A truncated set of Fourier coefficients is first precomputed classically from the corrected wavefunction and used to initialise a compact quantum state onto a $2l$-qubit register. As shown in Figure 5.6, the loading circuit implements sequences of uniformly controlled rotations, U_{UCR}, including alternating layers of **CNOT** gates interleaved with both $\mathbf{R_y}$ and $\mathbf{R_z}$ gates that result in total $2(2^{2l+1} - 3)$ gates. The remaining $n - l$ qubits per dimension are then activated via entangling operations of $n - l$ **CNOT** gates, which effectively expands the state to the full $2n$-qubit register by zero-padding. Finally, an inverse QFT maps the encoded amplitudes to real-space. The total number of gates for this FSL procedure is denoted by $2^{2l+2} + n^2/2 + 2n - l - 13/2$ (for odd n).

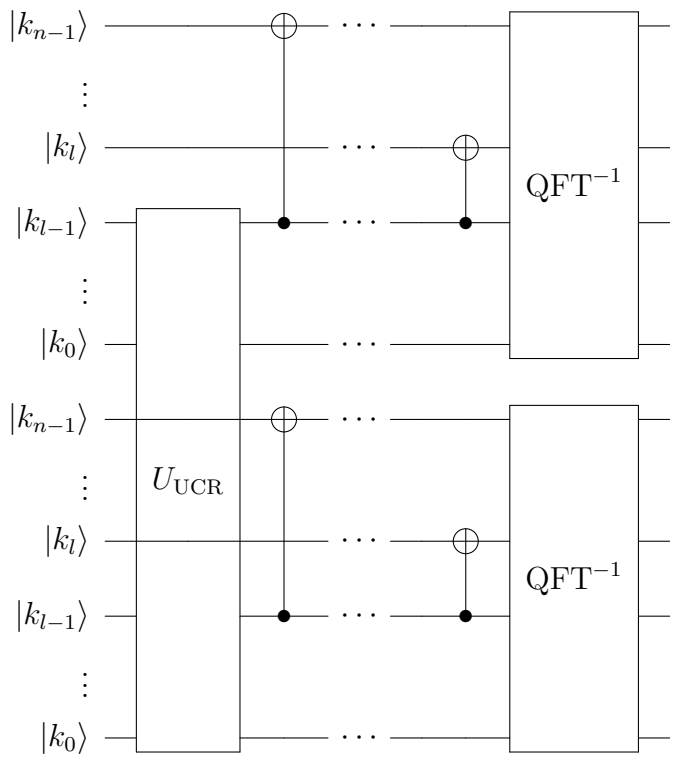

Figure 5.6: Quantum circuit for preparing the corrected wavefunction of the 2D hydrogen system. The U_{UCR} block denotes the uniformly controlled rotations that encode the $2l$ Fourier coefficients.

The choice of truncation level l depends on the trade-off between simulation fidelity and gate complexity. For instance, by fixing $n = 7$, we benchmark FSL-based initial states prepared from Qiskit [183] with varying l values against the exact corrected wavefunction. Figure 5.7 shows that with $l = 6$, the time-dependent

autocorrelation remains fully consistent with the exact result. The corresponding gate count, 16,410, is nearly half of that required by full-amplitude loading. Further reduction to $l = 5$ introduces minor deviations and undesirable oscillations in $A|(t)|$, but still fundamentally preserves the global stability of autocorrelation behaviours.

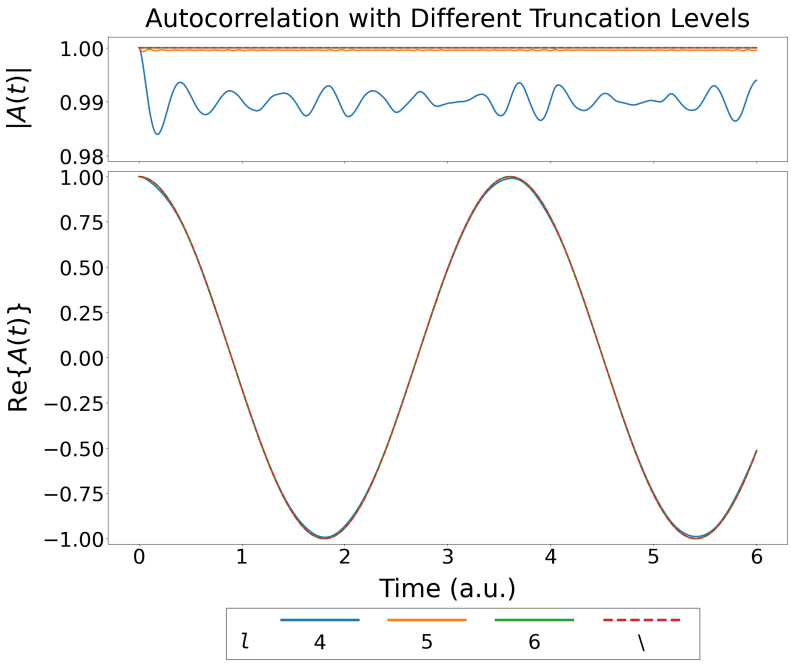

Figure 5.7: Autocorrelation functions recorded from 2D hydrogen simulations initialised with corrected wavefunctions prepared by FSL method. l represents the truncation level used in the state preparation. Benchmark data simulated from the exact corrected wavefunction ($n = 7$) are displayed in dashed linestyle.

5.5.2 Implementation of Corrected Hamiltonian

Simulating quantum dynamics on digital quantum hardware requires careful construction of the time evolution operator using gate-efficient techniques. In this section, we present the quantum implementation of time propagation under the trotterized Hamiltonian. The full circuit is composed of three fundamental components: the kinetic evolution operator, the potential evolution operator, and the QFT that facilitates conversion between position and momentum spaces, as illustrated in Figure 5.5. Here the QFT and its inverse block are applied before and after the kinetic term, respectively, each introducing $n^2/2 + n - 1/2$ gates for odd n.

The kinetic evolution operator takes the form of an exponentiated quadratic polynomial in the momentum basis, which can be succinctly complied into successive controlled $\mathbf{U_1}$ gates. For the 2D hydrogen system, it factorizes along dimensions as:

$$e^{-iKdt} = e^{(\frac{-ip_x^2 dt}{2})} e^{(\frac{-ip_y^2 dt}{2})},$$

resulting in a gate count of n^2 per Trotter step per n-qubit sub-register.

We then turn to the potential evolution operator, $e^{-iV_{\text{corrected}}dt/2}$, which is implemented directly in the position basis. A compact and ancilla-free method for realising such diagonal unitary by Walsh-operator formalism has been proposed by [289], which first maps the target unitary into a product of exponentials of Walsh operators, and then reorder them to reduce repeated **CNOT** gates.

We begin by expanding the discrete diagonal function $F = -V_{\text{corrected}}dt$, consisting of $N_{\text{total}} = 2^{2n}$ real values, as a Walsh series,

$$F = \sum_{j=0}^{N_{\text{total}}-1} a_j w_j,$$

where the coefficients a_js are obtained from the Walsh–Hadamard transform (WHT) of F. The Walsh operators ω_j are indexed by their Paley order j, and these indices are further grouped by the most significant non-zero bit, b, of their binary representation $|j\rangle$. The quantum circuit for a given ω_j consists of a Pauli-Z gate acting on the bth qubit, flanked by a set of **CNOT** gates.

Since all Walsh operators commute, the potential evolution operator can be expressed as

$$e^{-iV_{\text{corrected}}dt} = e^{iF} = \prod_{j=0}^{N_{\text{total}}-1} e^{ia_j\omega_j} = \prod_{j=0}^{N_{\text{total}}-1} U_j,$$

where each unitary U_j has the same circuit structure as ω_j, except that the central Pauli-Z gate is replaced by a rotation gate $\mathbf{R_z}(-2a_j)$. The concatenation of these circuits naturally allows cancellation of trailing **CNOT** gates from one block with leading **CNOT** gates of the next. The resulting circuit within each b-partition implements alternating layers of $\mathbf{R_z}(-2a_j)_{[b]}$ and $\mathbf{CNOT}^{[c]}_{[b]}$ gates, with the subscript and superscript representing target and control qubits, respectively. Specifically,

a $\mathbf{CNOT}_{[b]}^{[c]}$ gate is introduced only when the cth bit of the bitwise XOR between adjacent $|j\rangle$ is non-zero. To close each group, additional $\mathbf{CNOT}_{[b]}^{[c]}$ gates accounting for the XOR between the first and last $|j\rangle$ in each group are inserted at its beginning.

The total number of such **CNOT** gates can be reduced by carefully reordering the N_{total} $\mathbf{R_z}(-2a_j)$ rotations so as to minimise the number of non-zero XOR bits. This is optimally accomplished by arranging them in Gray-code sequence, where adjacent binary representations differ by a single bit. Under this construction, only one **CNOT** is required between successive $\mathbf{R_z}(-2a_j)$ gates, and thus yielding the shallowest circuit depth of $2^{2n+1} - 3$ gates.

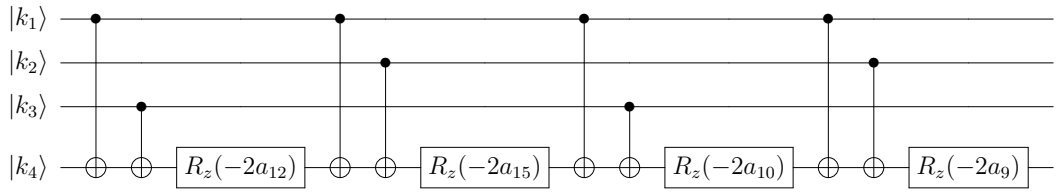

Figure 5.8: Circuit fragment corresponding to the $b = 4$ partition group. The four remaining indices $\{12, 15, 10, 9\}$ are arranged in gray-code order.

In practice, the number of non-trivial Walsh components is often much smaller than N_{total}, and discarding those a_j near zero significantly simplifies the circuit while preserving autocorrelation behaviours. For example, with $n = 7$ qubits per sub-register, we find that retaining only the largest $N_{\text{approx}} = 2^{12}$ coefficients (instead of the full 2^{14}) still generates E_{dynamic} and time fidelity indistinguishable from using the exhaustive series. Consequently, the number of $\mathbf{R_z}(-2a_j)$ gates reduces to $2^{12} = 4096$. Arranging this truncated set of 2^{12} indices in Gray-code order produces 8312 **CNOT** gates. Therefore, the total gate count for implementing $e^{-iV_{\text{corrected}}dt/2}$ is 12408. Figure 5.8 illustrates a representative fragment of the constructed circuit corresponding to the partition group of $b = 4$, where only four j values, $\{12, 15, 10, 9\}$, survive the truncation.

Following the structure shown in Figure 5.5, the propagation of one single time step dt includes the full-step kinetic evolution, both half-step potential evolutions, and double QFTs, which amounts to 25038 gates in total, For 6000 steps, the circuit depth scales linearly to $\sim 1.5 \times 10^8$ gates.

5.6 Conclusions

The grid-based SO-QFT method employed in this work has wide applicability in simulating time-propagated quantum dynamics. However, its accuracy degrades in the presence of Coulombic singularities, as the associated infinite value cannot be adequately represented using finite grids. While increasing grid density mitigates this error by more closely depicting the divergence, the exponential scaling of computational memory presents a major burden, especially for simulations with numerous Trotter steps. We therefore develop two correction schemes, one targeting Hamiltonian and the other focusing on wavefunction, to improve the robustness of Coulombic system simulations while maintaining the existing coarse grids.

The first correction reformulates the Coulomb potential by calculating its expectation value under the actual grid basis functions. This correction is pre-computed once and does not inflate costs during the time evolution. Our simulations in 1D electron-electron quantum ring and 2D nucleus-electron hydrogen systems validate the ability of the corrected potential to reduce bias in numerical energy and stabilise time fidelity. The second scheme concerns a wavefunction correction based on analytic solutions of soft Coulomb potentials. By incorporating additional polynomials and energy terms calibrated to specific grid resolution into the initial state, we create an initial state for 2D hydrogen that better represents the eigenstate of its grid-based Hamiltonian. Starting from this corrected wavefunction yields near-perfect time fidelity throughout the evolution window.

Although the corrections do not reproduce the exact singular behaviour, they consistently deliver smaller errors than the uncorrected forms. Because the associated deviation is systematic rather than stochastic, e.g., manifesting as quantifiable differences between corrected and analytical ground-state energies, it can be readily incorporated into analyses and practically subtracted as a correctible offset if necessary. Our correction schemes may offer tangible benefits when applied to more complex scenarios, such as simulations of multi-component systems involving hydrogen interacting with heavier atoms or under the influence of spatially varying external potentials (e.g., electric or magnetic). In such settings, small numerical

inaccuracies can be amplified and distort long-range interactions. The outlined strategies help reduce cumulative numerical errors and facilitate improved stability, leading to more reliable predictions of system dynamics.

The correction schemes proposed in this work also adapt readily to quantum computing architectures. The corrected potential operator can be implemented using a truncated Walsh expansion, while the corrected wavefunction is prepared through a truncated Fourier series. By appropriately selecting truncation thresholds to preserve simulation accuracy, we estimate a circuit depth of $\sim 1.5 \times 10^8$ gates for simulating a 2D hydrogen system with $n = 7$ qubits per dimension over 6,000 Trotter steps.

Future optimisations will be directed toward broadening the scope and efficiency of these corrections. On the algorithmic side, incorporating off-diagonal contributions into the potential correction may improve accuracy by accounting for inter-basis overlaps that are currently neglected. Similarly, generalising the wavefunction correction to more Coulombic systems will expand its versatility. From a quantum computing perspective, these correction schemes are compelling for minimising error accumulation without demanding additional qubits, which is particularly advantageous in resource-constrained regimes. Embedding them into large-scale models could enable high-fidelity quantum simulations under realistic computational budgets.

6
Conclusions

The potential of quantum computing stems mainly from the ability to encode and manipulate exponentially-scaling representations of many-body systems using only a linearly-scaling number of qubits and polynomially-scaling operations. Realising this potential in chemistry, however, requires explicit algorithms that are both theoretically rigorous and practically implementable. The overarching aim of this thesis has been to examine the grid-based Split Operator–Quantum Fourier Transform (SO-QFT) method, coupled with autocorrelation-based readout, as a versatile framework for simulating quantum dynamics, and to assess its practical viability as a pathway toward fault-tolerant quantum simulation. The work set out not only to develop an algorithmic framework, comprising state preparation, SO-QFT time evolution, and observable measurement, but also to evaluate its feasibility, accuracy, and quantum resource demands for representative chemical challenges through classical emulation. Across the three complementary studies presented in this work, this framework is consistently applied yet flexibly adapted. In this way, we provide a coherent account of what our end-to-end framework can deliver, what it requires, and how the cost scales.

In the first project, we construct the complete quantum circuit to realise our framework for multi-mode vibronic wavepacket propagation, and validate it by computing physical observables such as vibronic absorption spectra and population

dynamics between vibronically coupled electronic states. We further establish explicit, reusable scaling relations for the associated costs, translating physically meaningful resolution choices (e.g., grid size and time stepping) into concrete quantum budgets and thus providing quantitative roadmaps for hardware targets. While allocating at least $n = 4$ qubits are necessary for each normal mode, a 4-mode abstraction of photoexcited pyrazine results in a circuit depth of $\mathcal{O}(10^5)$ gates, and a full 24-mode model demands $\mathcal{O}(10^6)$ gates (both evaluated for 512 steps within 264 fs). The measurement effort required to obtain reliable spectra is estimated at $\mathcal{O}(10^5)$ shots.

Neglecting noise and error correction overhead, one may roughly estimate execution times on ideal quantum hardware by adopting nominal gate times: 35 ns for one-qubit and 423 ns for two-qubit operations, as indicated from [290, 291]. For the 24D circuit, a straightforward scaling of $\mathcal{O}(10^6)$ gates by 423 ns per gate gives a crude runtime estimate of $\sim$1.21 seconds. While this estimate is idealised and omits critical aspects such as fault-tolerant overheads or real-world decoherence, it serves to indicate the potential quantum advantage in execution time of such high-dimensional simulation task.

In the second project, we developed a time-dependent approach for simulating infrared spectra. It preserves the grid-based SO-QFT backbone but augments it with non-unitary dipole operators implemented via probabilistic strageties and higher-order potential terms, while maintaining tractable gate depth. On a tri-mode water model we showed that characteristic bands are accurately recovered, identified optimal time-discretisation parameters that balance fidelity and circuit depth, and validated cost-saving approximations (harmonic initial states, truncated dipoles) with minimal impact on spectral information. A illustrative circuit organisation of this model allocates $n = 4$ qubits per normal mode register, leading to $\mathcal{O}(10^9)$ gates for evolving 60,000 steps within 3950 fs.

Beyond the more accessible vibrational simulations, Hamiltonians governed by Coulombic interactions challenge our time-dependent framework because the use of finite grids near singularities destabilises the propagation. Rather than

relying on brute-force grid refinement, in our third project we introduced two complementary remedies for this breakdown: (i) a Hamiltonian correction that incorporates grid basis functions, and (ii) an initial-state correction that better matches the discretised Hamiltonian. On hydrogenic testbeds, they substantially improved time fidelity over long evolutions and reduced energy bias under fixed resource budgets. Crucially, both corrections admit circuit-compatible encodings using truncated series representations. For the case of 2D hydrogen system with $n = 7$ qubits per dimension, the resulting circuit depth is quantified at $\mathcal{O}(10^8)$ gates for a propagation of 6,000 steps.

In conclusion, this work realises the motivations set out at the outset, advancing the grid-based SO-QFT scheme into a quantitatively validated framework that is predictable in cost, faithful in output, and robust in scope. The three studies narrow the gap between theoretical promise and hardware-aligned requirements with a set of benchmarks that can guide future implementations on fault-tolerant quantum platforms.

While the contributions outlined here represent substantive progress, it is important to recognise certain limitations that shape the directions of subsequent studies. First, all validation in this thesis relies on classical emulation that presume fault-tolerant, noise-free execution and perfect logical operations. The explicit overheads arising from quantum error correction are not fully incorporated into the reported qubit and depth counts. Likewise, we have not modelled precision requirements on control operations during long propagations, nor the compilation overheads of multi-controlled gates on realistic architectures with restricted connectivity. As a result, the present estimates should be read as lower bounds at the logical level.

A natural next step is to move beyond logical resource estimates and toward physical hardware budgets under error-correcting codes [292, 293]. This requires decomposing the circuit into the Clifford + T gate set [294, 295], mapping them to the layout and connectivity of surface-code lattices [296, 297], and quantifying parallelism and qubit routing on restricted topologies [298, 299]. Such translation

will enable a more comprehensive assessment of the scalability and practicality of the proposed framework.

Future work should also focus on incorporating high-success block-encodings of non-unitary operators into our framework. In the current simulations of infrared spectra, non-unitary dipole operators are implemented probabilistically: success is obtained only upon favourable ancilla measurement outcomes. This strategy incurs elevated sampling demands with additional cost–precision trade-offs. One potential solution is to utilise amplitude amplification [245, 246] to boost success probabilities and thereby lower measurement requirements. Beyond improved success rates, these constructions will also benefit the efficient application of non-unitary damping functions directly to autocorrelation functions within the quantum circuit. In this way, damping can be performed natively on quantum hardware, and the resulting damped autocorrelation can then be Fourier transformed in situ via canonical QPE, obviating the need for post-processing on classical computers.

A further limitation arises from the reliance on Hadamard-test circuits for autocorrelation measurement. The Hadamard test, while widely adopted, imposes nontrivial constraints on circuit structure. In their standard form, these protocols require an ancillary qubit that controls the entire time-evolution operator. This global control removes the natural concurrency available in SO-QFT propagation: in the absence of control, kinetic, potential, and QFT blocks acting on independent registers can be executed in parallel, preventing circuit depth from scaling directly with the number of degrees of freedom. Under Hadamard control, however, these blocks must be applied sequentially, leading to a significant increase in depth. Overcoming this restriction will require control-free or ancilla-free measurement strategies, such as echo verification schemes [300, 301], that can restore concurrency while still enabling faithful extraction of autocorrelation functions.

This work has focused on rectilinear grid representations, where the constant volume element and the diagonal form of the kinetic energy operator in momentum space enable an efficient SO–QFT implementation. The trade-off then shifts to

the potential term: for floppy molecules exhibiting large-amplitude motion, rectilinear representations often require non-polynomial or tabulated potentials, whose propagators need to be synthesised as general unitaries with significant resource overhead. Conversely, general curvilinear or periodic coordinates can provide a more compact description of such potentials. However, this scheme introduces coordinate-dependent kinetic operators with non-trivial metric factors and volume elements, thereby breaking the clean kinetic-potential split and substantially increasing the circuit complexity. Future developments of the SO–QFT framework will therefore confront this central design question: whether to prioritise simplicity in the kinetic or the potential structure. Hybrid strategies that combine rectilinear normal modes for small-amplitude vibrations with curvilinear coordinates for selected large-amplitude degrees of freedom may offer a practical and balanced route toward more general molecular simulations on fault-tolerant quantum architectures.

Looking ahead, the present framework invites extension to more complex environments, as the current work does not exhaust the breadth of the chemical landscape. For instance, appropriate treatments of multi-surface dynamics involving spin–orbit couplings, or strong-field driven dynamics remain to be explored. Similarly, systems with more complex initial states, including thermal ensembles, highly excited wavepackets, and continuum scattering states, are not addressed here. Pursuing these multiple directions will test the flexibility of the grid-based SO-QFT scheme and demonstrate its generality in addressing central problems of time-dependent chemical dynamics.

Appendices

A

Supplementary Datasets for Infrared Simulation

This appendix provides the supplementary numerical datasets supporting the analyses presented in Chapter 4. Table A.1 reports fundamentals obtained from simulations using an approximate dipole operator: the first-order dipole operator is constructed via the circuit in Figure 4.1 with gate phases specified by the approximation in Eq. 4.10, and then applied to the approximate harmonic ground state. We tabulate the band positions and intensities under systematic variations of both total evolution time and time resolution. Tables A.2 and A.3 present large datasets of fundamental bands for all four $\mu\Psi$ approximation schemes, with the former covering cases of varying total evolution time at fixed resolution, and the latter covering varying resolution at fixed total time. Finally, Table A.4 provides overtone band positions and intensities for the two intermediate approximation schemes, $\mu_{\mathrm{1st}}\Psi_{\mathrm{ITE}}$ and $\mu_{\mathrm{3rd}}\Psi_{\mathrm{Gauss}}$, each reported for two different total evolution times.

T (fs)	n_t	dt (fs)	Mode 1		Mode 2		Mode 3	
			$\widetilde{\upsilon}_c$ (cm^{-1})	I_{IR} (km/mol)	$\widetilde{\upsilon}_c$ (cm^{-1})	I_{IR} (km/mol)	$\widetilde{\upsilon}_c$ (cm^{-1})	I_{IR} (km/mol)
Various total evolution time T, with a fixed time resolution dt:								
1975	30,000	0.066	3807.2 ± 17.7	4.7	1625.3 ± 4.1	72.6	3874.7 ± 9.4	38.3
3950	60,000	0.066	3809.1 ± 4.0	4.6	1625.1 ± 2.0	74.2	3876.2 ± 3.2	36.7
7900	120,000	0.066	3809.2 ± 0.8	4.7	1624.6 ± 0.9	72.9	3876.6 ± 0.8	38.3
13165	200,000	0.066	3808.9 ± 0.8	4.9	1624.2 ± 0.3	71.0	3876.6 ± 0.5	38.8
Various time resolution dt, with a fixed total evolution time T:								
3950	20,000	0.198	3814.8 ± 4.2	4.8	1627.2 ± 2.4	73.3	3882.2 ± 3.2	38.2
3950	40,000	0.099	3810.5 ± 4.2	4.8	1625.5 ± 1.6	73.2	3877.8 ± 3.3	37.4
3950	60,000	0.066	3809.1 ± 4.0	4.6	1625.1 ± 2.0	74.2	3876.2 ± 3.2	36.7
3950	80,000	0.049	3808.6 ± 4.0	4.6	1625.0 ± 2.2	74.2	3875.6 ± 3.3	37.2

Table A.1: Fundamental bands simulated from various time parameters. Here $\widetilde{\upsilon}_c$ and I_{IR} represent the band position and absolute band intensity, respectively. All simulations start from the approximate harmonic ground state and utilise approximated first-order dipole operators realised by the quantum circuit shown in Figure 4.1 with gate angles defined as Eq. 4.10.

Time Parameters			$\widetilde{\upsilon}_c$ (cm^{-1})				I_{IR} (km/mol)			
T fs	n_t	dt fs	$\mu_{3\mathrm{rd}}\Psi_{\mathrm{ITE}}$	$\mu_{1\mathrm{st}}\Psi_{\mathrm{ITE}}$	$\mu_{3\mathrm{rd}}\Psi_{\mathrm{Gauss}}$	$\mu_{1\mathrm{st}}\Psi_{\mathrm{Gauss}}$	$\mu_{3\mathrm{rd}}\Psi_{\mathrm{ITE}}$	$\mu_{1\mathrm{st}}\Psi_{\mathrm{ITE}}$	$\mu_{3\mathrm{rd}}\Psi_{\mathrm{Gauss}}$	$\mu_{1\mathrm{st}}\Psi_{\mathrm{Gauss}}$
Mode 1										
1975	30,000	0.066	3807.2 ± 17.7	3807.2 ± 17.7	3807.2 ± 17.7	3807.2 ± 17.7	4.7	5.9	4.5	4.8
3950	60,000	0.066	3809.1 ± 4.6	3809.1 ± 4.0	3809.1 ± 4.1	3809.1 ± 4.0	4.6	5.8	4.4	4.7
7900	120,000	0.066	3809.2 ± 0.9	3809.2 ± 0.8	3809.2 ± 0.9	3809.2 ± 0.8	4.6	5.8	4.5	4.8
13165	200,000	0.066	3808.9 ± 0.8	3808.9 ± 0.8	3808.9 ± 0.8	3808.9 ± 0.8	4.8	6.1	4.7	5.0
Mode 2										
1975	30,000	0.066	1625.3 ± 4.1	1625.3 ± 4.1	1625.3 ± 4.1	1625.3 ± 4.1	80.0	78.9	75.6	74.0
3950	60,000	0.066	1625.1 ± 2.0	1625.1 ± 2.0	1625.1 ± 2.0	1625.1 ± 2.0	81.7	80.6	77.2	75.6
7900	120,000	0.066	1624.6 ± 0.9	1624.6 ± 0.9	1624.6 ± 0.9	1624.6 ± 0.9	79.2	78.2	74.9	73.3
13165	200,000	0.066	1624.2 ± 0.3	1624.2 ± 0.3	1624.2 ± 0.3	1624.2 ± 0.3	78.3	77.2	73.9	72.4
Mode 3										
1975	30,000	0.066	3874.7 ± 9.5	3874.7 ± 9.4	3874.7 ± 9.4	3874.7 ± 9.4	38.9	42.9	36.3	38.5
3950	60,000	0.066	3876.2 ± 3.2	3876.2 ± 3.2	3876.2 ± 3.2	3876.2 ± 3.2	37.2	41.1	34.7	36.8
7900	120,000	0.066	3876.6 ± 0.8	3876.6 ± 0.8	3876.6 ± 0.8	3876.6 ± 0.8	38.9	42.9	36.3	38.5
13165	200,000	0.066	3876.6 ± 0.5	3876.6 ± 0.5	3876.6 ± 0.5	3876.6 ± 0.5	39.4	43.5	36.7	39.0

Table A.2: Fundamental bands obtained from simulations with four different approximation schemes in $\mu\Psi$, under varying total evolution time at fixed time resolution. Here $\widetilde{\upsilon}_c$ and I_{IR} represent the band position and absolute band intensity, respectively.

Time Parameters			$\widetilde{\upsilon}_c$ (cm^{-1})				I_{IR} (km/mol)			
T fs	n_t	dt fs	$\mu_{\mathrm{3rd}}\Psi_{\mathrm{ITE}}$	$\mu_{\mathrm{1st}}\Psi_{\mathrm{ITE}}$	$\mu_{\mathrm{3rd}}\Psi_{\mathrm{Gauss}}$	$\mu_{\mathrm{1st}}\Psi_{\mathrm{Gauss}}$	$\mu_{\mathrm{3rd}}\Psi_{\mathrm{ITE}}$	$\mu_{\mathrm{1st}}\Psi_{\mathrm{ITE}}$	$\mu_{\mathrm{3rd}}\Psi_{\mathrm{Gauss}}$	$\mu_{\mathrm{1st}}\Psi_{\mathrm{Gauss}}$
Mode 1										
3950	20,000	0.198	3814.8 ± 4.2	3814.8 ± 4.1	3814.8 ± 4.2	3814.8 ± 4.2	4.7	6.0	4.6	4.9
3950	40,000	0.099	3810.5 ± 4.3	3810.5 ± 4.2	3810.5 ± 4.3	3810.5 ± 4.2	4.7	5.9	4.6	4.9
3950	60,000	0.066	3809.1 ± 4.1	3809.1 ± 4.0	3809.1 ± 4.1	3809.1 ± 4.0	4.6	5.8	4.4	4.7
3950	80,000	0.049	3808.6 ± 4.0	3808.6 ± 4.0	3808.6 ± 4.0	3808.6 ± 4.0	4.6	5.8	4.5	4.7
Mode 2										
3950	20,000	0.198	1627.2 ± 2.4	1627.2 ± 2.4	1627.2 ± 2.4	1627.2 ± 2.4	80.7	79.7	76.3	74.7
3950	40,000	0.099	1625.5 ± 1.6	1625.5 ± 1.6	1625.5 ± 1.6	1625.5 ± 1.6	80.7	79.6	76.2	74.6
3950	60,000	0.066	1625.1 ± 2.0	1625.1 ± 2.0	1625.1 ± 2.0	1625.1 ± 2.0	81.7	80.6	77.2	75.6
3950	80,000	0.049	1625.0 ± 2.2	1625.0 ± 2.2	1625.0 ± 2.2	1625.0 ± 2.2	81.7	80.6	77.2	75.5
Mode 3										
3950	20,000	0.198	3882.2 ± 3.2	3882.2 ± 3.2	3882.2 ± 3.2	3882.2 ± 3.2	38.7	42.8	36.1	38.3
3950	40,000	0.099	3877.8 ± 3.3	3877.8 ± 3.3	3877.8 ± 3.3	3877.8 ± 3.3	37.9	41.9	35.3	37.5
3950	60,000	0.066	3876.2 ± 3.2	3876.2 ± 3.2	3876.2 ± 3.2	3876.2 ± 3.2	37.2	41.1	34.7	36.8
3950	80,000	0.049	3875.6 ± 3.3	3875.6 ± 3.3	3875.6 ± 3.3	3875.6 ± 3.3	37.7	41.6	35.1	37.3

Table A.3: Fundamental bands obtained from simulations with four different approximation schemes in $\mu\Psi$, under varying time resolution at fixed total evolution time. Here $\widetilde{\upsilon}_c$ and I_{IR} represent the band position and absolute band intensity, respectively.

$\mu_{1st}\Psi_{ITE}$			
$\widetilde{\upsilon}_c$ (cm^{-1})		I_{IR} (km/mol)	
T=3950 fs	T=13165 fs	T=3950 fs	T=13165 fs
3198.7 ± 19.9	3200.6 ± 10.5	0.062	0.064
4733.7 ± 15.4	4737.4 ± 7.7	0.050	0.051
5381.9 ± 12.2	5383.9 ± 4.2	0.035	0.033
5428.7 ± 8.5	5429.6 ± 4.2	0.17	0.17
6131.7 ± 15.1	6133.2 ± 6.8	0.036	0.036
6942.4 ± 17.9	6948.5 ± 9.1	0.089	0.089
7005.8 ± 17.1	7008.6 ± 4.7	0.021	0.015
7593.0 ± 10.4	7593.5 ± 4.8	0.13	0.14
7644.4 ± 6.3	7644.8 ± 3.0	0.83	0.83
7812.4 ± 37.9	7813.1 ± 4.9	0.015	0.018
8412.1 ± 15.0	8413.7 ± 5.9	0.033	0.035
8437.4 ± 37.9	8441.5 ± 4.5	0.017	0.015
/	9082.8 ± 4.4	/	0.012
/	9091.3 ± 4.9	/	0.0097
9112.4 ± 14.7	9116.2 ± 6.1	0.061	0.051
9826.8 ± 15.6	9828.8 ± 7.3	0.068	0.067
9869.0 ± 17.1	9870.6 ± 5.2	0.029	0.029
/	10532.0 ± 11.4	/	0.0063
/	10539.6 ± 4.5	/	0.013
/	10663.7 ± 4.5	/	0.013
/	11143.9 ± 5.1	/	0.010
11385.4 ± 14.9	11391.0 ± 5.8	0.047	0.049
11445.5 ± 12.6	11447.2 ± 5.6	0.10	0.10
11503.6 ± 14.2	11506.2 ± 5.4	0.052	0.050
11546.2 ± 14.4	11549.6 ± 6.6	0.076	0.080
/	11857.2 ± 11.4	/	0.0071
/	11912.9 ± 11.4	/	0.0070
11972.1 ± 17.1	11971.2 ± 5.2	0.035	0.035

Table A.4: Overtones simulated using different total propagation time lengths and approximation schemes in $\mu\Psi$, with a fixed time step size $dt \approx 0.066$ fs. Here $\widetilde{\upsilon}_c$ and I_{IR} represent the band position and absolute band intensity, respectively. The simulations in this panel (a) start from a ground state prepared via ITE and utilise dipole operators truncated at first order, i.e., $\mu_{1st}\Psi_{ITE}$. Panel (b) continues on the next page.

$\mu_{3rd}\Psi_{Gauss}$			
$\widetilde{\upsilon}_c$ (cm^{-1})		I_{IR} (km/mol)	
T=3950 fs	T=13165 fs	T=3950 fs	T=13165 fs
3206.6 ± 7.4	3206.9 ± 3.9	0.50	0.50
4733.3 ± 13.0	4736.0± 6.6	0.070	0.072
5384.3 ± 3.1	5384.6 ± 0.7	5.8	6.0
5427.3 ± 3.3	5427.9 ± 0.8	7.9	7.9
6135.0 ± 7.6	6135.4 ± 3.4	0.16	0.16
6943.0 ± 16.3	6948.0 ± 8.3	0.11	0.11
7006.3 ± 16.2	7008.7 ± 4.1	0.025	0.019
7596.0 ± 4.0	7595.5 ± 1.4	1.9	1.9
7643.5 ± 3.7	7643.5 ± 1.0	8.4	8.4
7813.3 ± 37.0	7813.4 ± 3.6	0.032	0.035
8418.7 ± 13.4	8418.9 ± 4.5	0.087	0.086
8440.0 ± 30.2	8439.7 ± 1.8	0.18	0.18
/	9084.0 ± 2.6	/	0.052
/	9090.9 ± 3.4	/	0.039
9110.5 ± 5.6	9111.7 ± 1.3	1.5	1.5
9827.3 ± 14.1	9828.9 ± 6.5	0.084	0.083
9870.7 ± 16.0	9871.7 ± 4.3	0.046	0.046
/	10532.2 ± 11.2	/	0.0076
/	10539.6 ± 4.0	/	0.018
/	10664.1 ± 3.7	/	0.020
/	11143.9 ± 5.1	/	0.010
11390.1 ± 9.3	11391.7 ± 2.8	0.21	0.21
11447.9 ± 4.6	11448.0 ± 2.0	0.79	0.82
11504.9 ± 10.6	11506.0 ± 3.7	0.11	0.11
11547.3 ± 13.1	11550.0 ± 5.9	0.096	0.10
/	11858.1 ± 7.9	/	0.024
/	11914.0 ± 5.0	/	0.057
11972.0 ± 12.7	11971.6 ± 3.9	0.064	0.064

Table A.4: Overtones simulated using different total propagation time lengths and approximation schemes in $\mu\Psi$, with a fixed time step size $dt \approx 0.066$ fs. Here $\widetilde{\upsilon}_c$ and I_{IR} represent the band position and absolute band intensity, respectively. The simulations in this panel (b) start from an approximate Gaussian-product ground state and utilise dipole operators truncated at third order, i.e., $\mu_{3rd}\Psi_{Gauss}$. (Continued from the previous page).

B

Supplementary Computational Workflow

The quantum algorithms developed in this thesis were emulated on classical hardware to validate their physical correctness and to assess quantum resource requirements. A schematic overview of the computational workflow is shown in Figure B.1. Spatial degrees of freedom are discretised on uniform grids, upon which the initial state is defined and the Hamiltonian constructed. Temporal discretisation specifies the Trotter step size, from which the split-operator propagators are synthesised using the discretised kinetic and potential operators. Statevector propagation is then performed under the SO-QFT scheme up to the target propagation time, during which relevant time-dependent observables are extracted. The resulting data are subsequently post-processed and analysed for physical validation and resource estimation.

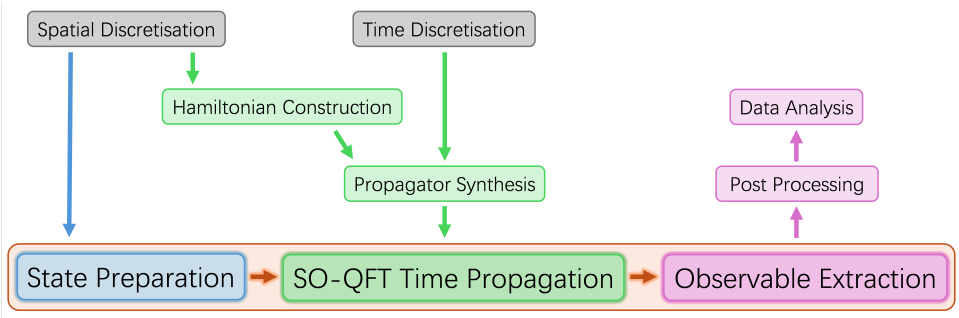

Figure B.1: Schematic overview of the computational framework used for classical emulation.

A representative implementation of this workflow developed for the vibronic simulations in Chapter 3 is publicly available at `https://github.com/XN-F/GridBasedPyrazine`. The repository includes Python-based scripts for state preparation, time propagation, observable extraction, statistical modelling of measurement costs, and the associated data analysis and visualisation.

References

[1] Adrián Gómez Pueyo et al. “Propagators for the Time-Dependent Kohn–Sham Equations: Multistep, Runge–Kutta, Exponential Runge–Kutta, and Commutator Free Magnus Methods”. In: *Journal of Chemical Theory and Computation* 14.6 (2018), pp. 3040–3052.

[2] Kota Hanasaki et al. “Implementation of real-time TDDFT for periodic systems in the open-source PySCF software package”. In: *Journal of Computational Chemistry* 44.9 (2023), pp. 980–987.

[3] Joscha Hekele et al. “All-electron real-time and imaginary-time time-dependent density functional theory within a numeric atom-centered basis function framework”. In: *The Journal of Chemical Physics* 155.15 (Oct. 2021), p. 154801.

[4] Min Choi et al. “QRCODE: Massively parallelized real-time time-dependent density functional theory for periodic systems”. In: *Computer Physics Communications* 305 (2024), p. 109349.

[5] W. van Dijk and F. M. Toyama. “Accurate numerical solutions of the time-dependent Schrödinger equation”. In: *Phys. Rev. E* 75 (3 Mar. 2007), p. 036707.

[6] Micheline B. Soley et al. “Functional Tensor-Train Chebyshev Method for Multidimensional Quantum Dynamics Simulations”. In: *Journal of Chemical Theory and Computation* 18.1 (2022), pp. 25–36.

[7] Brandon C. Cooper et al. “Short Iterative Lanczos Integration in Time-Dependent Equation-of-Motion Coupled-Cluster Theory”. In: *The Journal of Physical Chemistry A* 125.24 (2021), pp. 5438–5447.

[8] Jürgen Schnack. “Exact Diagonalization Techniques for Quantum Spin Systems”. In: *Computational Modelling of Molecular Nanomagnets*. Ed. by Gopalan Rajaraman. Cham: Springer International Publishing, 2023, pp. 155–177.

[9] M. ten Brink et al. “Real-time non-adiabatic dynamics in the one-dimensional Holstein model: Trajectory-based vs exact methods”. In: *The Journal of Chemical Physics* 156.23 (June 2022), p. 234109.

[10] Michael Innerberger et al. “Electron-light interaction in nonequilibrium: exact diagonalization for time-dependent Hubbard Hamiltonians”. In: *The European Physical Journal Plus* 135.11 (Nov. 2020).

[11] Christian Lubich. *From Quantum to Classical Molecular Dynamics: Reduced Models and Numerical Analysis*. Zurich Lectures in Advanced Mathematics. European Mathematical Society (EMS), Zürich, 2008, pp. x+144.

[12] Guido R. Mocken and Christoph H. Keitel. “FFT-split-operator code for solving the Dirac equation in 2+1 dimensions”. In: *Computer Physics Communications* 178.11 (2008), pp. 868–882.

[13] Mark R. Hermann and J. A. Fleck. “Split-operator spectral method for solving the time-dependent Schrödinger equation in spherical coordinates”. In: *Phys. Rev. A* 38 (12 Dec. 1988), pp. 6000–6012.

[14] Ronnie Kosloff. “Time-dependent quantum-mechanical methods for molecular dynamics”. In: *The Journal of Physical Chemistry* 92 (1988), 2087–2100.

[15] Masuo Suzuki. “Generalized Trotter’s formula and systematic approximants of exponential operators and inner derivations with applications to many-body problems”. In: *Communications in Mathematical Physics* 51.2 (June 1976), pp. 183–190.

[16] Masuo Suzuki. “Decomposition formulas of exponential operators and Lie exponentials with some applications to quantum mechanics and statistical physics”. In: *Journal of Mathematical Physics* 26.4 (Apr. 1985), pp. 601–612.

[17] Masuo Suzuki. “Fractal decomposition of exponential operators with applications to many-body theories and Monte Carlo simulations”. In: *Physics Letters A* 146.6 (1990), pp. 319–323.

[18] Xiaogang Zhu, Haiyang Wan, and Yaping Zhang. “A split-step finite element method for the space-fractional Schrödinger equation in two dimensions”. In: *Scientific Reports* 14.1 (Oct. 2024), p. 24257.

[19] Anastassiya Semenova et al. “Comparison of split-step and Hamiltonian integration methods for simulation of the nonlinear Schrödinger type equations”. In: *Journal of Computational Physics* 427 (Feb. 2021), p. 110061.

[20] Narayanasami Sathyamurthy and Susanta Mahapatra. “Time-dependent quantum mechanical wave packet dynamics”. In: *Phys. Chem. Chem. Phys.* 23 (13 2021), pp. 7586–7614.

[21] Julien Roulet and Jiří Vaníček. “An implicit split-operator algorithm for the nonlinear time-dependent Schrödinger equation”. In: *The Journal of Chemical Physics* 155.20 (Nov. 2021).

[22] Damian Kołaczek, Bartłomiej J. Spisak, and Maciej Wołoszyn. “The Phase–Space Approach to time Evolution of Quantum States in Confined Systems: the Spectral Split–Operator Method”. In: *International Journal of Applied Mathematics and Computer Science* 29.3 (2019), pp. 439–451.

[23] Lachlan P. Lindoy, Benedikt Kloss, and David R. Reichman. “Time evolution of ML-MCTDH wavefunctions. II. Application of the projector splitting integrator”. In: *The Journal of Chemical Physics* 155.17 (Nov. 2021), p. 174109.

[24] Takeshi Sato et al. “Time-dependent multiconfiguration self-consistent-field and time-dependent optimized coupled-cluster methods for intense laser-driven multielectron dynamics”. In: *Canadian Journal of Chemistry* 101.9 (2023), pp. 698–709.

[25] Souvik Mandal et al. “Stochastic multi-configuration time-dependent Hartree for dissipative quantum dynamics with strong intramolecular coupling”. In: *The Journal of Chemical Physics* 157.14 (Oct. 2022), p. 144105.

[26] Yuki Orimo, Takeshi Sato, and Kenichi L. Ishikawa. "Efficient simulation of multielectron dynamics in molecules under intense laser pulses: implementation of the multiconfiguration time-dependent Hartree–Fock method based on the adaptive finite element method". In: *Canadian Journal of Chemistry* 101.9 (2023), pp. 664–671.

[27] Ningyi Lyu, Micheline B. Soley, and Victor S. Batista. "Tensor-Train Split-Operator KSL (TT-SOKSL) Method for Quantum Dynamics Simulations". In: *Journal of Chemical Theory and Computation* 18.6 (2022), pp. 3327–3346.

[28] Raffaele Borrelli and Maxim F. Gelin. "Finite temperature quantum dynamics of complex systems: Integrating thermo-field theories and tensor-train methods". In: *WIREs Computational Molecular Science* 11.6 (2021), e1539.

[29] Raffaele Borrelli and Sergey Dolgov. "Expanding the Range of Hierarchical Equations of Motion by Tensor-Train Implementation". In: *The Journal of Physical Chemistry B* 125.20 (2021), pp. 5397–5407.

[30] Maxim F. Gelin and Raffaele Borrelli. "Simulation of Nonlinear Femtosecond Signals at Finite Temperature via a Thermo Field Dynamics-Tensor Train Method: General Theory and Application to Time- and Frequency-Resolved Fluorescence of the Fenna–Matthews–Olson Complex". In: *Journal of Chemical Theory and Computation* 17.7 (2021), pp. 4316–4331.

[31] Henrik R. Larsson. "A tensor network view of multilayer multiconfiguration time-dependent Hartree methods". In: *Molecular Physics* 122.14 (Feb. 2024).

[32] Yulin Wu et al. "Strong Quantum Computational Advantage Using a Superconducting Quantum Processor". In: *Phys. Rev. Lett.* 127 (18 Oct. 2021), p. 180501.

[33] Lars S. Madsen et al. "Quantum computational advantage with a programmable photonic processor". In: *Nature* 606.7912 (June 2022), pp. 75–81.

[34] Yu-Hao Deng et al. "Gaussian Boson Sampling with Pseudo-Photon-Number-Resolving Detectors and Quantum Computational Advantage". In: *Phys. Rev. Lett.* 131 (15 Oct. 2023), p. 150601.

[35] Ashley Montanaro. "Quantum algorithms: an overview". In: *npj Quantum Information* 2.1 (Jan. 2016), p. 15023.

[36] Andrew J. Daley et al. "Practical quantum advantage in quantum simulation". In: *Nature* 607.7920 (July 2022), pp. 667–676.

[37] Katherine L. Brown, William J. Munro, and Vivien M. Kendon. "Using Quantum Computers for Quantum Simulation". In: *Entropy* 12.11 (2010), pp. 2268–2307.

[38] Christian W. Bauer et al. "Quantum Simulation for High-Energy Physics". In: *PRX Quantum* 4.2 (May 2023).

[39] K. Temme et al. "Quantum Metropolis sampling". In: *Nature* 471.7336 (Mar. 2011), pp. 87–90.

[40] Daniel S. Abrams and Seth Lloyd. "Simulation of Many-Body Fermi Systems on a Universal Quantum Computer". In: *Physical Review Letters* 79.13 (Sept. 1997), pp. 2586–2589.

[41] M. B. Hastings et al. *Improving Quantum Algorithms for Quantum Chemistry*. 2014.

[42] Stephen P. Jordan, Keith S. M. Lee, and John Preskill. "Quantum Algorithms for Quantum Field Theories". In: *Science* 336.6085 (2012), pp. 1130–1133.

[43] I. M. Georgescu, S. Ashhab, and Franco Nori. "Quantum simulation". In: *Reviews of Modern Physics* 86 (1 Mar. 2014), pp. 153–185.

[44] Dominic W. Berry, Andrew M. Childs, and Robin Kothari. "Hamiltonian Simulation with Nearly Optimal Dependence on all Parameters". In: *2015 IEEE 56th Annual Symposium on Foundations of Computer Science*. IEEE, Oct. 2015, pp. 792–809.

[45] Xiao-Ming Zhang, Tongyang Li, and Xiao Yuan. "Quantum State Preparation with Optimal Circuit Depth: Implementations and Applications". In: *Physical Review Letters* 129.23 (Nov. 2022).

[46] Efekan Kökcü et al. "Algebraic compression of quantum circuits for Hamiltonian evolution". In: *Physical Review A* 105.3 (Mar. 2022).

[47] Kaito Wada et al. "Simulating time evolution with fully optimized single-qubit gates on parametrized quantum circuits". In: *Physical Review A* 105.6 (June 2022).

[48] Nikita Astrakhantsev et al. "Time evolution of uniform sequential circuits". In: *Physical Review Research* 5.3 (Sept. 2023).

[49] Maurits S. J. Tepaske, Dominik Hahn, and David J. Luitz. "Optimal compression of quantum many-body time evolution operators into brickwall circuits". In: *SciPost Physics* 14.4 (Apr. 2023).

[50] Jeongwan Haah et al. "Quantum Algorithm for Simulating Real Time Evolution of Lattice Hamiltonians". In: *SIAM Journal on Computing* 52.6 (2023), FOCS18-250-FOCS18–284.

[51] Pei Yuan and Shengyu Zhang. "Optimal (controlled) quantum state preparation and improved unitary synthesis by quantum circuits with any number of ancillary qubits". In: *Quantum* 7 (Mar. 2023), p. 956.

[52] R. Cleve et al. "Quantum algorithms revisited". In: *Proceedings of the Royal Society of London. Series A: Mathematical, Physical and Engineering Sciences* 454.1969 (Jan. 1998), pp. 339–354.

[53] D. Coppersmith. *An approximate Fourier transform useful in quantum factoring*. 2002.

[54] Michael A. Nielsen and Isaac L. Chuang. *Quantum Computation and Quantum Information: 10th Anniversary Edition*. Cambridge University Press, 2010.

[55] P.W. Shor. "Algorithms for quantum computation: discrete logarithms and factoring". In: *Proceedings 35th Annual Symposium on Foundations of Computer Science*. 1994, pp. 124–134.

[56] Jielun Chen, E.M. Stoudenmire, and Steven R. White. "Quantum Fourier Transform Has Small Entanglement". In: *PRX Quantum* 4.4 (Oct. 2023).

[57] Vinayak Dixit and Sisi Jian. "Quantum Fourier transform to estimate drive cycles". In: *Scientific Reports* 12.1 (Jan. 2022), p. 654.

[58] Daan Camps, Roel Van Beeumen, and Chao Yang. "Quantum Fourier transform revisited". In: *Numerical Linear Algebra with Applications* 28.1 (Sept. 2020).

[59] Ivan S. Oliveira et al. “5 - Implementation of Quantum Algorithms by NMR”. In: *NMR Quantum Information Processing*. Amsterdam: Elsevier Science B.V., 2007, pp. 183–205.

[60] Yehuda B. Band and Yshai Avishai. “5 - Quantum Information”. In: *Quantum Mechanics with Applications to Nanotechnology and Information Science*. Amsterdam: Academic Press, 2013, pp. 193–258.

[61] Michelle Wynne Sze et al. *Hamiltonian dynamics simulation using linear combination of unitaries on an ion trap quantum computer*. 2025.

[62] Pei Zeng et al. “Simple and High-Precision Hamiltonian Simulation by Compensating Trotter Error with Linear Combination of Unitary Operations”. In: *PRX Quantum* 6.1 (Mar. 2025).

[63] Dong An, Jin-Peng Liu, and Lin Lin. “Linear Combination of Hamiltonian Simulation for Nonunitary Dynamics with Optimal State Preparation Cost”. In: *Physical Review Letters* 131.15 (Oct. 2023).

[64] Richard Meister, Simon C. Benjamin, and Earl T. Campbell. “Tailoring Term Truncations for Electronic Structure Calculations Using a Linear Combination of Unitaries”. In: *Quantum* 6 (Feb. 2022), p. 637.

[65] Priyanka Mukhopadhyay, Torin F. Stetina, and Nathan Wiebe. “Quantum Simulation of the First-Quantized Pauli-Fierz Hamiltonian”. In: *PRX Quantum* 5.1 (Mar. 2024).

[66] Guang Hao Low and Isaac L. Chuang. “Hamiltonian Simulation by Qubitization”. In: *Quantum* 3 (July 2019), p. 163.

[67] Dominic W. Berry et al. “Qubitization of Arbitrary Basis Quantum Chemistry Leveraging Sparsity and Low Rank Factorization”. In: *Quantum* 3 (Dec. 2019), p. 208.

[68] Vera von Burg et al. “Quantum computing enhanced computational catalysis”. In: *Physical Review Research* 3.3 (July 2021).

[69] Hans Hon Sang Chan et al. “Grid-based methods for chemistry simulations on a quantum computer”. In: *Science Advances* 9.9 (Mar. 2023).

[70] Andrew M. Childs et al. “Quantum simulation of real-space dynamics”. In: *Quantum* 6 (Nov. 2022), p. 860.

[71] Pauline J Ollitrault et al. “Quantum algorithms for grid-based variational time evolution”. In: *Quantum* 7 (Oct. 2023), p. 1139.

[72] Seth Lloyd. “Universal Quantum Simulators”. In: *Science* 273.5278 (1996), pp. 1073–1078.

[73] Ian D. Kivlichan et al. “Improved Fault-Tolerant Quantum Simulation of Condensed-Phase Correlated Electrons via Trotterization”. In: *Quantum* 4 (July 2020), p. 296.

[74] Benjamin D. M. Jones et al. *Optimising Trotter-Suzuki Decompositions for Quantum Simulation Using Evolutionary Strategies*. 2019.

[75] Ivan Kassal et al. “Polynomial-time quantum algorithm for the simulation of chemical dynamics”. In: *Proceedings of the National Academy of Sciences* 105.48 (Dec. 2008), pp. 18681–18686.

[76] Christof Zalka. “Simulating quantum systems on a quantum computer”. In: *Proceedings of the Royal Society of London. Series A: Mathematical, Physical and Engineering Sciences* 454.1969 (1998), pp. 313–322.

[77] Rachel Crespo-Otero and Mario Barbatti. “Recent Advances and Perspectives on Nonadiabatic Mixed Quantum–Classical Dynamics”. In: *Chemical Reviews* 118.15 (2018), pp. 7026–7068.

[78] Michael S. Schuurman and Albert Stolow. “Dynamics at Conical Intersections”. In: *Annual Review of Physical Chemistry* 69.Volume 69, 2018 (2018), pp. 427–450.

[79] Basile F. E. Curchod and Todd J. Martínez. “Ab Initio Nonadiabatic Quantum Molecular Dynamics”. In: *Chemical Reviews* 118.7 (2018), pp. 3305–3336.

[80] Sebastian Mai and Leticia González. “Molecular Photochemistry: Recent Developments in Theory”. In: *Angewandte Chemie International Edition* 59.39 (2020), pp. 16832–16846.

[81] Wolfgang Domcke and David R. Yarkony. “Role of Conical Intersections in Molecular Spectroscopy and Photoinduced Chemical Dynamics”. In: *Annual Review of Physical Chemistry* 63.Volume 63, 2012 (2012), pp. 325–352.

[82] Graham A. Worth and Lorenz S. Cederbaum. “BEYOND BORN-OPPENHEIMER: Molecular Dynamics Through a Conical Intersection”. In: *Annual Review of Physical Chemistry* 55.Volume 55, 2004 (2004), pp. 127–158.

[83] Wolfgang Domcke, David R Yarkony, and Horst Köppel. *Conical Intersections*. WORLD SCIENTIFIC, 2004.

[84] David R. Yarkony. “Diabolical conical intersections”. In: *Rev. Mod. Phys.* 68 (4 Oct. 1996), pp. 985–1013.

[85] Yinan Shu et al. “Diabatic States of Molecules”. In: *The Journal of Physical Chemistry A* 126.7 (2022), pp. 992–1018.

[86] Yafu Guan et al. “High-fidelity first principles nonadiabaticity: diabatization, analytic representation of global diabatic potential energy matrices, and quantum dynamics”. In: *Phys. Chem. Chem. Phys.* 23 (44 2021), pp. 24962–24983.

[87] Joel M. Bowman, Tucker Carrington, and Hans-Dieter Meyer. “Variational quantum approaches for computing vibrational energies of polyatomic molecules”. In: *Molecular Physics* 106.16-18 (Aug. 2008), pp. 2145–2182.

[88] Alán Aspuru-Guzik et al. “Simulated Quantum Computation of Molecular Energies”. In: *Science* 309.5741 (Sept. 2005), pp. 1704–1707.

[89] Ivan Kassal et al. “Simulating Chemistry Using Quantum Computers”. In: *Annual Review of Physical Chemistry* 62.1 (May 2011), pp. 185–207.

[90] John Preskill. “Quantum Computing in the NISQ era and beyond”. In: *Quantum* 2 (Aug. 2018), p. 79.

[91] Alberto Peruzzo et al. “A variational eigenvalue solver on a photonic quantum processor”. In: *Nature Communications* 5.1 (July 2014).

[92] Jarrod R McClean et al. “The theory of variational hybrid quantum-classical algorithms”. In: *New Journal of Physics* 18.2 (Feb. 2016), p. 023023.

[93] Abhinav Kandala et al. “Hardware-efficient variational quantum eigensolver for small molecules and quantum magnets”. In: *Nature* 549.7671 (Sept. 2017), pp. 242–246.

[94] P. J. J. O’Malley et al. “Scalable Quantum Simulation of Molecular Energies”. In: *Phys. Rev. X* 6 (3 July 2016), p. 031007.

[95] Sam McArdle et al. “Quantum computational chemistry”. In: *Reviews of Modern Physics* 92.1 (Mar. 2020).

[96] Sergey B. Bravyi and Alexei Yu. Kitaev. “Fermionic Quantum Computation”. In: *Annals of Physics* 298.1 (May 2002), pp. 210–226.

[97] Jacob T. Seeley, Martin J. Richard, and Peter J. Love. “The Bravyi-Kitaev transformation for quantum computation of electronic structure”. In: *The Journal of Chemical Physics* 137.22 (Dec. 2012).

[98] James D. Whitfield, Jacob Biamonte, and Alán Aspuru-Guzik. “Simulation of electronic structure Hamiltonians using quantum computers”. In: *Molecular Physics* 109.5 (Mar. 2011), pp. 735–750.

[99] Dominic W. Berry et al. “Quantum simulation of realistic materials in first quantization using non-local pseudopotentials”. In: *npj Quantum Information* 10.1 (Dec. 2024).

[100] Yuan Su et al. “Fault-Tolerant Quantum Simulations of Chemistry in First Quantization”. In: *PRX Quantum* 2.4 (Nov. 2021).

[101] Ryan Babbush et al. “Quantum simulation of chemistry with sublinear scaling in basis size”. In: *npj Quantum Information* 5.1 (Nov. 2019).

[102] Peter W. Shor. *Fault-tolerant quantum computation*. 1997.

[103] Daniel Gottesman. *Stabilizer Codes and Quantum Error Correction*. 1997.

[104] Barbara M. Terhal. “Quantum error correction for quantum memories”. In: *Reviews of Modern Physics* 87.2 (Apr. 2015), pp. 307–346.

[105] Austin G. Fowler et al. “Surface codes: Towards practical large-scale quantum computation”. In: *Physical Review A* 86.3 (Sept. 2012).

[106] Thomas E O’Brien, Brian Tarasinski, and Barbara M Terhal. “Quantum phase estimation of multiple eigenvalues for small-scale (noisy) experiments”. In: *New Journal of Physics* 21.2 (Feb. 2019), p. 023022.

[107] Dominic W. Berry et al. “Simulating Hamiltonian Dynamics with a Truncated Taylor Series”. In: *Physical Review Letters* 114.9 (Mar. 2015).

[108] Andrew M. Childs and Nathan Wiebe. “Hamiltonian simulation using linear combinations of unitary operations”. In: *Quantum Info. Comput.* 12.11–12 (Nov. 2012), pp. 901–924.

[109] András Gilyén et al. “Quantum singular value transformation and beyond: exponential improvements for quantum matrix arithmetics”. In: *Proceedings of the 51st Annual ACM SIGACT Symposium on Theory of Computing*. STOC ’19. ACM, June 2019, pp. 193–204.

[110] Andrew M. Childs et al. “Toward the first quantum simulation with quantum speedup”. In: *Proceedings of the National Academy of Sciences* 115.38 (Sept. 2018), pp. 9456–9461.

[111] Markus Reiher et al. “Elucidating reaction mechanisms on quantum computers”. In: *Proceedings of the National Academy of Sciences* 114.29 (July 2017), pp. 7555–7560.

[112] Yizhi Shen et al. “Real-Time Krylov Theory for Quantum Computing Algorithms”. In: *Quantum* 7 (July 2023), p. 1066.

[113] Katherine Klymko et al. “Real-Time Evolution for Ultracompact Hamiltonian Eigenstates on Quantum Hardware”. In: *PRX Quantum* 3 (2 May 2022), p. 020323.

[114] Hirofumi Nishi et al. “Optimal scheduling in probabilistic imaginary-time evolution on a quantum computer”. In: *Physical Review Research* 5.4 (Oct. 2023).

[115] Stefano Barison, Filippo Vicentini, and Giuseppe Carleo. “An efficient quantum algorithm for the time evolution of parameterized circuits”. In: *Quantum* 5 (July 2021), p. 512.

[116] H. F. Trotter. “On the Product of Semi-Groups of Operators”. In: *Proceedings of the American Mathematical Society* 10.4 (1959), pp. 545–551.

[117] Naomichi Hatano and Masuo Suzuki. “Finding Exponential Product Formulas of Higher Orders”. In: *Quantum Annealing and Other Optimization Methods*. Springer Berlin Heidelberg, Nov. 2005, pp. 37–68.

[118] Johann Ostmeyer. “Optimised Trotter decompositions for classical and quantum computing”. In: *Journal of Physics A: Mathematical and Theoretical* 56.28 (June 2023), p. 285303.

[119] André D. Bandrauk and Hai Shen. “Higher order exponential split operator method for solving time-dependent Schrödinger equations”. In: *Canadian Journal of Chemistry* 70.2 (1992), pp. 555–559.

[120] D.J. Tannor. *Introduction to Quantum Mechanics*. University Science Books, 2007.

[121] Andrew M. Childs et al. “Theory of Trotter Error with Commutator Scaling”. In: *Physical Review X* 11.1 (Feb. 2021).

[122] Ish Dhand and Barry C Sanders. “Stability of the Trotter–Suzuki decomposition”. In: *Journal of Physics A: Mathematical and Theoretical* 47.26 (June 2014), p. 265206.

[123] Masuo Suzuki. “General theory of fractal path integrals with applications to many-body theories and statistical physics”. In: *Journal of Mathematical Physics* 32.2 (Feb. 1991), pp. 400–407.

[124] M.D Feit, J.A Fleck, and A Steiger. “Solution of the Schrödinger equation by a spectral method”. In: *Journal of Computational Physics* 47.3 (1982), pp. 412–433.

[125] M. D. Feit and Jr. Fleck J. A. “Solution of the Schrödinger equation by a spectral method II: Vibrational energy levels of triatomic molecules”. In: *The Journal of Chemical Physics* 78.1 (Jan. 1983), pp. 301–308.

[126] Giuliano Benenti and Giuliano Strini. “Quantum simulation of the single-particle Schrödinger equation”. In: *American Journal of Physics* 76.7 (2008), pp. 657–662.

[127] Marcus Cramer et al. “Efficient quantum state tomography”. In: *Nature Communications* 1.1 (Dec. 2010).

[128] Michael Nauenberg. “Autocorrelation function and quantum recurrence of wave packets”. In: *J. Phys. B. At. Mol. Opt. Phys.* 23.15 (1990), pp. L385–L390.

[129] Smik Patel et al. “Quantum Measurement for Quantum Chemistry on a Quantum Computer”. In: *Chemical Reviews* (July 2025).

[130] Zhiyan Ding and Lin Lin. “Even Shorter Quantum Circuit for Phase Estimation on Early Fault-Tolerant Quantum Computers with Applications to Ground-State Energy Estimation”. In: *PRX Quantum* 4 (2 May 2023), p. 020331.

[131] Kosuke Mitarai and Keisuke Fujii. “Methodology for replacing indirect measurements with direct measurements”. In: *Physical Review Research* 1.1 (Aug. 2019).

[132] Abhijith J. et al. “Quantum Algorithm Implementations for Beginners”. In: *ACM Transactions on Quantum Computing* 3.4 (July 2022), pp. 1–92.

[133] Dorit Aharonov, Vaughan Jones, and Zeph Landau. “A Polynomial Quantum Algorithm for Approximating the Jones Polynomial”. In: *Algorithmica* 55.3 (Nov. 2009), pp. 395–421.

[134] Krysta M. Svore, Matthew B. Hastings, and Michael Freedman. *Faster Phase Estimation*. 2013.

[135] A. Yu. Kitaev. *Quantum measurements and the Abelian Stabilizer Problem*. 1995.

[136] P M Q Cruz et al. “Optimizing quantum phase estimation for the simulation of Hamiltonian eigenstates”. In: *Quantum Science and Technology* 5.4 (Aug. 2020), p. 044005.

[137] Yudong Cao et al. “Quantum Chemistry in the Age of Quantum Computing”. In: *Chemical Reviews* 119.19 (Aug. 2019), pp. 10856–10915.

[138] Hongkang Ni, Haoya Li, and Lexing Ying. “On low-depth algorithms for quantum phase estimation”. In: *Quantum* 7 (Nov. 2023), p. 1165.

[139] H.-D. Meyer, U. Manthe, and L.S. Cederbaum. “The multi-configurational time-dependent Hartree approach”. In: *Chemical Physics Letters* 165.1 (1990), pp. 73–78.

[140] M.H. Beck et al. “The multiconfiguration time-dependent Hartree (MCTDH) method: a highly efficient algorithm for propagating wavepackets”. In: *Physics Reports* 324.1 (2000), pp. 1–105.

[141] Uwe Manthe. “A multilayer multiconfigurational time-dependent Hartree approach for quantum dynamics on general potential energy surfaces”. In: *The Journal of Chemical Physics* 128.16 (Apr. 2008), p. 164116.

[142] I. V. Oseledets. “Tensor-Train Decomposition”. In: *SIAM Journal on Scientific Computing* 33.5 (2011), pp. 2295–2317.

[143] Ulrich Schollwöck. “The density-matrix renormalization group in the age of matrix product states”. In: *Annals of Physics* 326.1 (Jan. 2011), pp. 96–192.

[144] F. Verstraete, V. Murg, and J.I. Cirac. “Matrix product states, projected entangled pair states, and variational renormalization group methods for quantum spin systems”. In: *Advances in Physics* 57.2 (Mar. 2008), pp. 143–224.

[145] Pratik Nandy et al. “Quantum dynamics in Krylov space: Methods and applications”. In: *Physics Reports* 1125–1128 (June 2025), pp. 1–82.

[146] Y. Saad. “Analysis of Some Krylov Subspace Approximations to the Matrix Exponential Operator”. In: *SIAM Journal on Numerical Analysis* 29.1 (1992), pp. 209–228.

[147] Marlis Hochbruck and Christian Lubich. “On Krylov Subspace Approximations to the Matrix Exponential Operator”. In: *SIAM Journal on Numerical Analysis* 34.5 (1997), pp. 1911–1925.

[148] H. Tal-Ezer and R. Kosloff. “An accurate and efficient scheme for propagating the time dependent Schrödinger equation”. In: *The Journal of Chemical Physics* 81.9 (Nov. 1984), pp. 3967–3971.

[149] C Leforestier et al. “A comparison of different propagation schemes for the time dependent Schrödinger equation”. In: *Journal of Computational Physics* 94.1 (1991), pp. 59–80.

[150] S. Breda et al. “Infrared spectra of pyrazine, pyrimidine and pyridazine in solid argon”. In: *Journal of Molecular Structure* 786.2 (2006), pp. 193–206.

[151] Clemens Woywod et al. “Characterization of the S1–S2 conical intersection in pyrazine using ab initio multiconfiguration self-consistent-field and multireference configuration-interaction methods”. In: *The Journal of Chemical Physics* 100.2 (1994), pp. 1400–1413.

[152] Rongxing He et al. “Ab initio studies of excited electronic state S2 of pyrazine and Franck–Condon simulation of its absorption spectrum”. In: *Chemical Physics Letters* 476.1 (2009), pp. 19–24.

[153] Stefan Krempl et al. “Path-integral treatment of multi-mode vibronic coupling”. In: *The Journal of Chemical Physics* 100.2 (1994), pp. 926–937.

[154] Stefan Krempl, Manfred Winterstetter, and Wolfgang Domcke. “Path-integral treatment of multi-mode vibronic coupling. II. Correlation expansion of class averages”. In: *The Journal of Chemical Physics* 102.16 (1995), pp. 6499–6510.

[155] G. A. Worth, H.-D. Meyer, and L. S. Cederbaum. “The effect of a model environment on the S2 absorption spectrum of pyrazine: A wave packet study treating all 24 vibrational modes”. In: *The Journal of Chemical Physics* 105.11 (1996), pp. 4412–4426.

[156] A. Raab et al. “Molecular dynamics of pyrazine after excitation to the S2 electronic state using a realistic 24-mode model Hamiltonian”. In: *The Journal of Chemical Physics* 110.2 (1999), pp. 936–946.

[157] Eric W. Fischer and Peter Saalfrank. “A thermofield-based multilayer multiconfigurational time-dependent Hartree approach to non-adiabatic quantum dynamics at finite temperature”. In: *The Journal of Chemical Physics* 155.13 (Oct. 2021), p. 134109.

[158] Matthieu Sala et al. “Laser control of the radiationless decay in pyrazine using the dynamic Stark effect”. In: *The Journal of Chemical Physics* 140.19 (2014), p. 194309.

[159] Michael Thoss, William H. Miller, and Gerhard Stock. “Semiclassical description of nonadiabatic quantum dynamics: Application to the S1–S2 conical intersection in pyrazine”. In: *The Journal of Chemical Physics* 112.23 (2000), pp. 10282–10292.

[160] Panchanan Puzari et al. “A quantum-classical approach to the photoabsorption spectrum of pyrazine”. In: *The Journal of Chemical Physics* 123.13 (2005), p. 134317.

[161] Xin Chen and Victor S. Batista. “Matching-pursuit/split-operator-Fourier-transform simulations of excited-state nonadiabatic quantum dynamics in pyrazine”. In: *The Journal of Chemical Physics* 125.12 (Sept. 2006).

[162] Dmitrii V. Shalashilin and Mark S. Child. “Real time quantum propagation on a Monte Carlo trajectory guided grids of coupled coherent states: 26D simulation of pyrazine absorption spectrum”. In: *The Journal of Chemical Physics* 121.8 (Aug. 2004), pp. 3563–3568.

[163] Maximilian A. C. Saller and Scott Habershon. “Basis Set Generation for Quantum Dynamics Simulations Using Simple Trajectory-Based Methods”. In: *Journal of Chemical Theory and Computation* 11.1 (2015), pp. 8–16.

[164] Maximilian A. C. Saller and Scott Habershon. “Quantum Dynamics with Short-Time Trajectories and Minimal Adaptive Basis Sets”. In: *Journal of Chemical Theory and Computation* 13.7 (2017), pp. 3085–3096.

[165] R Schneider and W Domcke. “S1-S2 Conical intersection and ultrafast S2→S1 Internal conversion in pyrazine”. In: *Chemical Physics Letters* 150.3 (1988), pp. 235–242.

[166] Manabu Kanno et al. “Ab initio quantum dynamical analysis of ultrafast nonradiative transitions via conical intersections in pyrazine”. In: *Physical Chemistry Chemical Physics* 17 (3 2015), pp. 2012–2024.

[167] Addison J. Schile and David T. Limmer. “Simulating conical intersection dynamics in the condensed phase with hybrid quantum master equations”. In: *The Journal of Chemical Physics* 151.1 (July 2019), p. 014106.

[168] Bing Gu and Shaul Mukamel. “Cooperative Conical Intersection Dynamics of Two Pyrazine Molecules in an Optical Cavity”. In: *The Journal of Physical Chemistry Letters* 11.14 (2020), pp. 5555–5562.

[169] Simon P Neville, Albert Stolow, and Michael S Schuurman. “Formation of electronic coherences in conical intersection-mediated dynamics”. In: *Journal of Physics B: Atomic, Molecular and Optical Physics* 55.4 (Mar. 2022), p. 044004.

[170] H. Köuppel, W. Domcke, and L. S. Cederbaum. “Multimode Molecular Dynamics Beyond the Born–Oppenheimer Approximation”. In: *Advances in Chemical Physics*. John Wiley & Sons, 1984, pp. 59–246.

[171] K.K. Innes, I.G. Ross, and William R. Moomaw. “Electronic states of azabenzenes and azanaphthalenes: A revised and extended critical review”. In: *Journal of Molecular Spectroscopy* 132.2 (1988), pp. 492–544.

[172] J. Franck and E. G. Dymond. “Elementary processes of photochemical reactions”. In: *Trans. Faraday Soc.* 21 (February 1926), pp. 536–542.

[173] Edward Condon. “A Theory of Intensity Distribution in Band Systems”. In: *Physical Review* 28 (6 Dec. 1926), pp. 1182–1201.

[174] Raymond T. Birge. “The Band Spectra of Carbon Monoxide”. In: *Physical Review* 28 (6 Dec. 1926), pp. 1157–1181.

[175] Josep M. Luis, David M. Bishop, and Bernard Kirtman. "A different approach for calculating Franck–Condon factors including anharmonicity". In: *The Journal of Chemical Physics* 120.2 (Jan. 2004), pp. 813–822.

[176] International Union of Pure and Applied Chemistry. *Franck–Condon principle*. IUPAC Gold Book. 2025.

[177] Sohang Kundu et al. "Franck–Condon and Herzberg–Teller Signatures in Molecular Absorption and Emission Spectra". In: *The Journal of Physical Chemistry B* 126.15 (2022), pp. 2899–2911.

[178] Mikko Möttönen et al. "Transformation of quantum states using uniformly controlled rotations". In: *Quantum Info. Comput.* 5.6 (Sept. 2005), pp. 467–473.

[179] Jason Iaconis, Sonika Johri, and Elton Yechao Zhu. "Quantum state preparation of normal distributions using matrix product states". In: *npj Quantum Information* 10.1 (Jan. 2024).

[180] Mudassir Moosa et al. "Linear-depth quantum circuits for loading Fourier approximations of arbitrary functions". In: *Quantum Science and Technology* 9.1 (Oct. 2023), p. 015002.

[181] Arthur G. Rattew et al. "The Efficient Preparation of Normal Distributions in Quantum Registers". In: *Quantum* 5 (Dec. 2021), p. 609.

[182] Christian W. Bauer et al. *Practical considerations for the preparation of multivariate Gaussian states on quantum computers*. 2021.

[183] Ali Javadi-Abhari et al. *Quantum computing with Qiskit*. 2024.

[184] Pauline J. Ollitrault, Guglielmo Mazzola, and Ivano Tavernelli. "Nonadiabatic Molecular Quantum Dynamics with Quantum Computers". In: *Physical Review Letters* 125 (26 Dec. 2020), p. 260511.

[185] Kianna Wan, Mario Berta, and Earl T. Campbell. "Randomized Quantum Algorithm for Statistical Phase Estimation". In: *Physical Review Letters* 129.3 (July 2022).

[186] Lin Lin and Yu Tong. "Heisenberg-Limited Ground-State Energy Estimation for Early Fault-Tolerant Quantum Computers". In: *PRX Quantum* 3.1 (Feb. 2022).

[187] Nick S. Blunt et al. "Statistical Phase Estimation and Error Mitigation on a Superconducting Quantum Processor". In: *PRX Quantum* 4.4 (Dec. 2023).

[188] Iwao Yamazaki et al. "Intramolecular electronic relaxation and photoisomerization processes in the isolated azabenzene molecules pyridine, pyrazine and pyrimidine". In: *Faraday Discuss. Chem. Soc.* 75 (0 1983), pp. 395–405.

[189] Samuel M. Greene and Victor S. Batista. "Tensor-Train Split-Operator Fourier Transform (TT-SOFT) Method: Multidimensional Nonadiabatic Quantum Dynamics". In: *Journal of Chemical Theory and Computation* 13.9 (2017), pp. 4034–4042.

[190] Thomas A. A. Oliver et al. "Controlling Electronic Product Branching at Conical Intersections in the UV Photolysis of para-Substituted Thiophenols". In: *The Journal of Physical Chemistry A* 116 (2012), pp. 12444–12459.

[191] Honghyun Kim et al. “Calculation of the infrared spectra of organophosphorus compounds and prediction of new types of nerve agents”. In: *New J. Chem.* 46 (18 2022), pp. 8653–8661.

[192] Aleksandr S. Kazachenko et al. “A density functional theory calculations of infrared spectra of galactomannan butyl ether”. In: *Journal of Molecular Structure* 1251 (2022), p. 131998.

[193] Yan Ji et al. “DFT-Calculated IR Spectrum Amide I, II, and III Band Contributions of N-Methylacetamide Fine Components”. In: *ACS Omega* 5.15 (2020), pp. 8572–8578.

[194] Airan F. S. Brito et al. “Infrared Spectroscopy of Ethanethiol Monomers and Dimers at MP2 Level: Characterizing the Dimer Formation and Hydrogen Bond”. In: *Journal of Computational Chemistry* 46.1 (2025), e27540.

[195] Subodh S. Khire, Takahito Nakajima, and Shridhar R. Gadre. “Cluster-in-Cluster Approach for Computing MP2-Level Vibrational Infrared Spectra of Large Molecular Clusters”. In: *The Journal of Physical Chemistry A* 128.18 (2024), pp. 3703–3710.

[196] Roie Knaanie et al. “Hybrid MP2/MP4 potential surfaces in VSCF calculations of IR spectra: Applications for organic molecules”. In: *Spectrochimica Acta Part A: Molecular and Biomolecular Spectroscopy* 119 (2014), pp. 2–11.

[197] Rodney J. Bartlett and John F. Stanton. “Applications of Post-Hartree—Fock Methods: A Tutorial”. In: *Reviews in Computational Chemistry*. John Wiley & Sons, Ltd, 1994, pp. 65–169.

[198] Peter R. Franke, John F. Stanton, and Gary E. Douberly. “How to VPT2: Accurate and Intuitive Simulations of CH Stretching Infrared Spectra Using VPT2+K with Large Effective Hamiltonian Resonance Treatments”. In: *The Journal of Physical Chemistry A* 125.6 (Feb. 2021), pp. 1301–1324.

[199] Jinfeng Liu et al. “Towards complete assignment of the infrared spectrum of the protonated water cluster H+(H2O)21”. In: *Nature Communications* 12.1 (Oct. 2021), p. 6141.

[200] Julien Bloino and Vincenzo Barone. “A second-order perturbation theory route to vibrational averages and transition properties of molecules: General formulation and application to infrared and vibrational circular dichroism spectroscopies”. In: *The Journal of Chemical Physics* 136.12 (Mar. 2012), p. 124108.

[201] Benjamin Schröder and Guntram Rauhut. “From the Automated Calculation of Potential Energy Surfaces to Accurate Infrared Spectra”. In: *The Journal of Physical Chemistry Letters* 15.11 (2024), pp. 3159–3169.

[202] Sebastian Erfort, Martin Tschöpe, and Guntram Rauhut. “Toward a fully automated calculation of rovibrational infrared intensities for semi-rigid polyatomic molecules”. In: *The Journal of Chemical Physics* 152.24 (June 2020), p. 244104.

[203] Alain Dargelos and Claude Pouchan. “CCSD(T)-F12 calculations of the IR spectrum of cyanoacetylene HC3N beyond the harmonic approximation”. In: *Chemical Physics Letters* 754 (2020), p. 137746.

[204] Chen Qu and Joel M. Bowman. “High-dimensional fitting of sparse datasets of CCSD(T) electronic energies and MP2 dipole moments, illustrated for the formic acid dimer and its complex IR spectrum”. In: *The Journal of Chemical Physics* 148.24 (Mar. 2018), p. 241713.

[205] Eric J. Heller. “The semiclassical way to molecular spectroscopy”. In: *Accounts of Chemical Research* 14.12 (1981), pp. 368–375.

[206] Shima Taherivardanjani et al. “Benchmarking the Computational Costs and Quality of Vibrational Spectra from Ab Initio Simulations”. In: *Advanced Theory and Simulations* 5.1 (2022), p. 2100293.

[207] Michael Gastegger, Jörg Behler, and Philipp Marquetand. “Machine learning molecular dynamics for the simulation of infrared spectra”. In: *Chem. Sci.* 8 (10 2017), pp. 6924–6935.

[208] Sean A. Fischer et al. “Infrared and Raman Spectroscopy from Ab Initio Molecular Dynamics and Static Normal Mode Analysis: The C–H Region of DMSO as a Case Study”. In: *The Journal of Physical Chemistry B* 120.8 (2016), pp. 1429–1436.

[209] Marie-Pierre Gaigeot and Michiel Sprik. “Ab Initio Molecular Dynamics Computation of the Infrared Spectrum of Aqueous Uracil”. In: *The Journal of Physical Chemistry B* 107.38 (2003), pp. 10344–10358.

[210] Stuart C. Althorpe. “Path Integral Simulations of Condensed-Phase Vibrational Spectroscopy”. In: *Annual Review of Physical Chemistry* 75.Volume 75, 2024 (2024), pp. 397–420.

[211] Sam Shepherd et al. “Efficient Quantum Vibrational Spectroscopy of Water with High-Order Path Integrals: From Bulk to Interfaces”. In: *The Journal of Physical Chemistry Letters* 12.37 (2021), pp. 9108–9114.

[212] Stuart C Althorpe. “Path-integral approximations to quantum dynamics”. en. In: *Eur. Phys. J. B* 94.7 (July 2021).

[213] Jian Liu and Zhijun Zhang. “Path integral Liouville dynamics: Applications to infrared spectra of OH, water, ammonia, and methane”. In: *The Journal of Chemical Physics* 144.3 (Jan. 2016), p. 034307.

[214] Nicolas P. D. Sawaya, Francesco Paesani, and Daniel P. Tabor. “Near- and long-term quantum algorithmic approaches for vibrational spectroscopy”. In: *Phys. Rev. A* 104 (6 Dec. 2021), p. 062419.

[215] Pauline J. Ollitrault et al. “Hardware efficient quantum algorithms for vibrational structure calculations”. In: *Chemical Science* 11 (2020), pp. 6842–6855.

[216] Sam McArdle et al. “Digital quantum simulation of molecular vibrations”. In: *Chemical Science* 10.22 (2019), pp. 5725–5735.

[217] Alexander Teplukhin, Brian K. Kendrick, and Dmitri Babikov. “Calculation of Molecular Vibrational Spectra on a Quantum Annealer”. In: *Journal of Chemical Theory and Computation* 15.8 (2019), pp. 4555–4563.

[218] Ling Hu et al. “Simulation of molecular spectroscopy with circuit quantum electrodynamics”. In: *Science Bulletin* 63.5 (2018), pp. 293–299.

[219] Ryan J. MacDonell et al. “Predicting molecular vibronic spectra using time-domain analog quantum simulation”. In: *Chemical Science* 14.35 (2023), pp. 9439–9451.

[220] Philip Richerme et al. “Quantum Computation of Hydrogen Bond Dynamics and Vibrational Spectra”. In: *The Journal of Physical Chemistry Letters* 14.32 (Aug. 2023), pp. 7256–7263.

[221] Ksenia Komarova et al. “Parallel Quantum Computation of Vibrational Dynamics”. In: *Frontiers in Physics* 8, 486 (Oct. 2020), p. 486.

[222] Dimitar Trenev et al. *Refining resource estimation for the quantum computation of vibrational molecular spectra through Trotter error analysis*. 2023.

[223] David Lauvergnat and André Nauts. “Quantum dynamics with sparse grids: A combination of Smolyak scheme and cubature. Application to methanol in full dimensionality”. In: *Spectrochimica Acta Part A: Molecular and Biomolecular Spectroscopy* 119 (2014), pp. 18–25.

[224] Gustavo Avila and Jr. Carrington Tucker. “Using nonproduct quadrature grids to solve the vibrational Schrödinger equation in 12D”. In: *The Journal of Chemical Physics* 134.5 (Feb. 2011), p. 054126.

[225] Maxim Rakhuba and Ivan Oseledets. “Calculating vibrational spectra of molecules using tensor train decomposition”. In: *The Journal of Chemical Physics* 145.12 (Sept. 2016), p. 124101.

[226] E Cantarella, F Culot, and J Liévin. “Ab initio calculation of vibrational dipole moment matrix elements. I. methods of calculation and diatomic test systems”. In: *Physica Scripta* 46.6 (Dec. 1992), p. 489.

[227] F. Culot and Jacques Liévin. “Ab initio calculation of vibrational dipole moment matrix elements.Ii.the water molecule as a polyatomic test case”. In: *Physica Scripta* 46 (1992), pp. 502–517.

[228] Guntram Rauhut. “Efficient calculation of potential energy surfaces for the generation of vibrational wave functions”. In: *The Journal of Chemical Physics* 121.19 (Nov. 2004), pp. 9313–9322.

[229] Bastiaan J. Braams and Joel M. Bowman. “Permutationally invariant potential energy surfaces in high dimensionality”. In: *International Reviews in Physical Chemistry* 28.4 (2009), pp. 577–606.

[230] Carolin König and Ove Christiansen. “Linear-scaling generation of potential energy surfaces using a double incremental expansion”. In: *The Journal of Chemical Physics* 145.6 (Aug. 2016), p. 064105.

[231] Jonathan P. Alborzpour, David P. Tew, and Scott Habershon. “Efficient and accurate evaluation of potential energy matrix elements for quantum dynamics using Gaussian process regression”. In: *The Journal of Chemical Physics* 145.17 (Nov. 2016), p. 174112.

[232] Benjamin Schröder and Guntram Rauhut. “From the Automated Calculation of Potential Energy Surfaces to Accurate Infrared Spectra”. In: *The Journal of Physical Chemistry Letters* 15.11 (2024), pp. 3159–3169.

[233] Gabriel G. Balint-Kurti, Richard N. Dixon, and C. Clay Marston. "Time-dependent quantum dynamics of molecular photofragmentation processes". In: *J. Chem. Soc., Faraday Trans.* 86 (10 1990), pp. 1741–1749.

[234] Oriol Vendrell, Fabien Gatti, and Hans-Dieter Meyer. "Full dimensional (15-dimensional) quantum-dynamical simulation of the protonated water dimer. II. Infrared spectrum and vibrational dynamics". In: *The Journal of Chemical Physics* 127.18 (Nov. 2007).

[235] Daniel Peláez and Hans-Dieter Meyer. "On the infrared absorption spectrum of the hydrated hydroxide (H3O2-) cluster anion". In: *Chemical Physics* 482 (2017), pp. 100–105.

[236] L. Lehtovaara, J. Toivanen, and J. Eloranta. "Solution of time-independent Schrödinger equation by the imaginary time propagation method". In: *Journal of Computational Physics* 221.1 (2007), pp. 148–157.

[237] Jarrod R. McClean and Alán Aspuru-Guzik. "Compact wavefunctions from compressed imaginary time evolution". In: *RSC Advances* 5.124 (2015), pp. 102277–102283.

[238] Sam McArdle et al. "Variational ansatz-based quantum simulation of imaginary time evolution". In: *npj Quantum Information* 5.1 (Sept. 2019).

[239] Niladri Gomes et al. "Efficient Step-Merged Quantum Imaginary Time Evolution Algorithm for Quantum Chemistry". In: *Journal of Chemical Theory and Computation* 16.10 (Sept. 2020), pp. 6256–6266.

[240] Chiara Leadbeater et al. "Non-unitary Trotter circuits for imaginary time evolution". In: *Quantum Science and Technology* 9.4 (July 2024), p. 045007.

[241] Hao-Nan Xie et al. "Probabilistic imaginary-time evolution algorithm based on nonunitary quantum circuits". In: *Phys. Rev. A* 109 (5 May 2024), p. 052414.

[242] Mario Motta et al. "Determining eigenstates and thermal states on a quantum computer using quantum imaginary time evolution". In: *Nature Physics* 16.2 (Nov. 2019), pp. 205–210.

[243] Kübra Yeter-Aydeniz, Raphael C. Pooser, and George Siopsis. "Practical quantum computation of chemical and nuclear energy levels using quantum imaginary time evolution and Lanczos algorithms". In: *npj Quantum Information* 6.1 (July 2020), p. 63.

[244] Taichi Kosugi et al. "Imaginary-time evolution using forward and backward real-time evolution with a single ancilla: First-quantized eigensolver algorithm for quantum chemistry". In: *Phys. Rev. Res.* 4 (3 Aug. 2022), p. 033121.

[245] Patrick Rall. "Faster Coherent Quantum Algorithms for Phase, Energy, and Amplitude Estimation". In: *Quantum* 5 (Oct. 2021), p. 566.

[246] Yulong Dong, Lin Lin, and Yu Tong. "Ground-State Preparation and Energy Estimation on Early Fault-Tolerant Quantum Computers via Quantum Eigenvalue Transformation of Unitary Matrices". In: *PRX Quantum* 3.4 (Oct. 2022).

[247] Marat Sibaev and Deborah L. Crittenden. "PyVCI: A flexible open-source code for calculating accurate molecular infrared spectra". In: *Computer Physics Communications* 203 (2016), pp. 290–297.

[248] Jonathan Tennyson et al. “The ExoMol database: Molecular line lists for exoplanet and other hot atmospheres”. In: *Journal of Molecular Spectroscopy* 327 (Sept. 2016), pp. 73–94.

[249] Oleg V. Prezhdo. “Modeling Non-adiabatic Dynamics in Nanoscale and Condensed Matter Systems”. In: *Accounts of Chemical Research* 54.23 (2021), pp. 4239–4249.

[250] Karl Michael Ziems et al. “Nuclear–Electron Correlation Effects and Their Photoelectron Imprint in Molecular XUV Ionisation”. In: *Frontiers in Chemistry* Volume 10 - 2022 (2022).

[251] Adam Kirrander and Dmitrii V. Shalashilin. “Quantum dynamics with fermion coupled coherent states: Theory and application to electron dynamics in laser fields”. In: *Phys. Rev. A* 84 (3 Sept. 2011), p. 033406.

[252] Zecheng Gan et al. “Fast algorithm for quasi-2D Coulomb systems”. In: *Journal of Computational Physics* 524 (Mar. 2025), p. 113733.

[253] Simon Elias Schrader et al. “Time evolution as an optimization problem: The hydrogen atom in strong laser fields in a basis of time-dependent Gaussian wave packets”. In: *The Journal of Chemical Physics* 161.4 (July 2024).

[254] Jannes Nys et al. “Ab-initio variational wave functions for the time-dependent many-electron Schrödinger equation”. In: *Nature Communications* 15.1 (Oct. 2024), p. 9404.

[255] Anders M. N. Niklasson. “Extended Lagrangian Born–Oppenheimer molecular dynamics for orbital-free density-functional theory and polarizable charge equilibration models”. In: *The Journal of Chemical Physics* 154.5 (Feb. 2021), p. 054101.

[256] Keefer Rowan et al. “Simulation of a hydrogen atom in a laser field using the time-dependent variational principle”. In: *Physical Review E* 101.2 (Feb. 2020).

[257] K. T. Schütt et al. “Unifying machine learning and quantum chemistry with a deep neural network for molecular wavefunctions”. In: *Nature Communications* 10.1 (Nov. 2019), p. 5024.

[258] László Füsti-Molnár and Peter Pulay. “The Fourier transform Coulomb method: Efficient and accurate calculation of the Coulomb operator in a Gaussian basis”. In: *The Journal of Chemical Physics* 117.17 (Nov. 2002), pp. 7827–7835.

[259] Tobias Schäfer et al. “Sampling the reciprocal Coulomb potential in finite anisotropic cells”. In: *The Journal of Chemical Physics* 160.5 (Feb. 2024).

[260] Yang Li et al. “Implementation of the Time-Dependent Complete-Active-Space Self-Consistent-Field Method for Diatomic Molecules”. In: *The Journal of Physical Chemistry A* 128.8 (Feb. 2024), pp. 1523–1532.

[261] Mykola Sereda et al. “Sparse-Stochastic Fragmented Exchange for Large-Scale Hybrid Time-Dependent Density Functional Theory Calculations”. In: *Journal of Chemical Theory and Computation* 20.10 (May 2024), pp. 4196–4204.

[262] A. A. Silaev et al. “Second-order imaginary differential operator for effective absorption in the numerical solution of the time-dependent Schrödinger equation”. In: *Phys. Rev. A* 108 (1 July 2023), p. 013118.

[263] Liang-You Peng and Anthony F. Starace. “Application of Coulomb wave function discrete variable representation to atomic systems in strong laser fields”. In: *The Journal of Chemical Physics* 125.15 (Oct. 2006).

[264] Ariel Gordon, Christian Jirauschek, and Franz X. Kärtner. “Numerical solver of the time-dependent Schrödinger equation with Coulomb singularities”. In: *Phys. Rev. A* 73 (4 Apr. 2006), p. 042505.

[265] Isao Kawata and Hirohiko Kono. “Dual transformation for wave packet dynamics: Application to Coulomb systems”. In: *The Journal of Chemical Physics* 111.21 (Dec. 1999), pp. 9498–9508.

[266] Xinyang Dong, Emanuel Gull, and Hugo U. R. Strand. “Excitations and spectra from equilibrium real-time Green’s functions”. In: *Phys. Rev. B* 106 (12 Sept. 2022), p. 125153.

[267] Andrew W. King, Adam L. Baskerville, and Hazel Cox. “Hartree–Fock implementation using a Laguerre-based wave function for the ground state and correlation energies of two-electron atoms”. In: *Philosophical Transactions of the Royal Society A: Mathematical, Physical and Engineering Sciences* 376.2115 (2018), p. 20170153.

[268] Pei-Yuan Zhao, Ke Ding, and Shuo Yang. “Chebyshev pseudosite matrix product state approach for the spectral functions of electron-phonon coupling systems”. In: *Physical Review Research* 5.2 (Apr. 2023).

[269] Tobias Dornheim et al. “Fermionic physics from ab initio path integral Monte Carlo simulations of fictitious identical particles”. In: *The Journal of Chemical Physics* 159.16 (Oct. 2023), p. 164113.

[270] T. Schoof et al. “Configuration Path Integral Monte Carlo”. In: *Contributions to Plasma Physics* 51.8 (2011), pp. 687–697.

[271] M Bonitz et al. “Theory and simulation of strong correlations in quantum Coulomb systems”. In: *Journal of Physics A: Mathematical and General* 36.22 (May 2003), p. 5921.

[272] Pontus Svensson et al. “Development of a new quantum trajectory molecular dynamics framework”. In: *Philosophical Transactions of the Royal Society A: Mathematical, Physical and Engineering Sciences* 381.2253 (July 2023).

[273] X. Oriols. “Quantum-Trajectory Approach to Time-Dependent Transport in Mesoscopic Systems with Electron-Electron Interactions”. In: *Phys. Rev. Lett.* 98 (6 Feb. 2007), p. 066803.

[274] S. V. Popruzhenko, G. G. Paulus, and D. Bauer. “Coulomb-corrected quantum trajectories in strong-field ionization”. In: *Phys. Rev. A* 77 (5 May 2008), p. 053409.

[275] Ryan Babbush et al. “Quantum simulation of exact electron dynamics can be more efficient than classical mean-field methods”. In: *Nature Communications* 14.1 (July 2023), p. 4058.

[276] Guang Hao Low et al. “Complexity of Implementing Trotter Steps”. In: *PRX Quantum* 4 (2 May 2023), p. 020323.

[277] Ian D Kivlichan et al. “Bounding the costs of quantum simulation of many-body physics in real space”. In: *Journal of Physics A: Mathematical and Theoretical* 50.30 (June 2017), p. 305301.

[278] David Poulin et al. *The Trotter Step Size Required for Accurate Quantum Simulation of Quantum Chemistry*. 2014.

[279] Chee-Kong Lee et al. “Variational Quantum Simulation of Chemical Dynamics with Quantum Computers”. In: *Journal of Chemical Theory and Computation* 18.4 (Apr. 2022), pp. 2105–2113.

[280] M. Cerezo et al. “Variational quantum algorithms”. In: *Nature Reviews Physics* 3.9 (Aug. 2021), pp. 625–644.

[281] Jules Tilly et al. “The Variational Quantum Eigensolver: A review of methods and best practices”. In: *Physics Reports* 986 (Nov. 2022), pp. 1–128.

[282] Abhinav Anand et al. “A quantum computing view on unitary coupled cluster theory”. In: *Chemical Society Reviews* 51.5 (2022), pp. 1659–1684.

[283] Harper R. Grimsley et al. “An adaptive variational algorithm for exact molecular simulations on a quantum computer”. In: *Nature Communications* 10.1 (July 2019).

[284] Rongxin Xia and Sabre Kais. “Quantum machine learning for electronic structure calculations”. In: *Nature Communications* 9.1 (Oct. 2018).

[285] X. L. Yang et al. “Analytic solution of a two-dimensional hydrogen atom. I. Nonrelativistic theory”. In: *Phys. Rev. A* 43 (3 Feb. 1991), pp. 1186–1196.

[286] Pierre-Fran çois Loos and Peter M. W. Gill. “Exact Wave Functions of Two-Electron Quantum Rings”. In: *Phys. Rev. Lett.* 108 (8 Feb. 2012), p. 083002.

[287] Chen Li. “Exact Analytical Solution of the Ground-State Hydrogenic Problem with Soft Coulomb Potential”. In: *The Journal of Physical Chemistry A* 125.23 (2021), pp. 5146–5151.

[288] Guang Hao Low et al. *Fast quantum simulation of electronic structure by spectrum amplification*. 2025.

[289] Jonathan Welch et al. “Efficient quantum circuits for diagonal unitaries without ancillas”. In: *New Journal of Physics* 16 (2014), p. 033040.

[290] Teague Tomesh et al. *SupermarQ: A Scalable Quantum Benchmark Suite*. 2022.

[291] Norbert M. Linke et al. “Experimental comparison of two quantum computing architectures”. In: *Proceedings of the National Academy of Sciences* 114.13 (Mar. 2017), pp. 3305–3310.

[292] J. Pablo Bonilla Ataides et al. “The XZZX surface code”. In: *Nature Communications* 12.1 (Apr. 2021).

[293] Rajeev Acharya et al. “Suppressing quantum errors by scaling a surface code logical qubit”. In: *Nature* 614.7949 (Feb. 2023), pp. 676–681.

[294] Vivien Vandaele et al. “Optimal Hadamard Gate Count for Clifford+T Synthesis of Pauli Rotations Sequences”. In: *ACM Transactions on Quantum Computing* 5.1 (Feb. 2024), pp. 1–29.

[295] Daniel Litinski. “A Game of Surface Codes: Large-Scale Quantum Computing with Lattice Surgery”. In: *Quantum* 3 (Mar. 2019), p. 128.

[296] George Watkins et al. “A High Performance Compiler for Very Large Scale Surface Code Computations”. In: *Quantum* 8 (May 2024), p. 1354.

[297] Matt McEwen, Dave Bacon, and Craig Gidney. “Relaxing Hardware Requirements for Surface Code Circuits using Time-dynamics”. In: *Quantum* 7 (Nov. 2023), p. 1172.

[298] Giacomo Nannicini et al. “Optimal Qubit Assignment and Routing via Integer Programming”. In: *ACM Transactions on Quantum Computing* 4.1 (Oct. 2022).

[299] Abtin Molavi et al. “Qubit Mapping and Routing via MaxSAT”. In: *Proceedings of the 55th Annual IEEE/ACM International Symposium on Microarchitecture*. MICRO ’22. Chicago, Illinois, USA: IEEE Press, 2023, pp. 1078–1091.

[300] Thomas E. O’Brien et al. “Error Mitigation via Verified Phase Estimation”. In: *PRX Quantum* 2 (2 May 2021), p. 020317.

[301] Stefano Polla, Gian-Luca R. Anselmetti, and Thomas E. O’Brien. “Optimizing the information extracted by a single qubit measurement”. In: *Phys. Rev. A* 108 (1 July 2023), p. 012403.